MODELING THERMAL REGENERATION IN RECIPROCATING, REACTING STREAMS WITH APPLICATIONS IN THERMOELECTRIC POWER GENERATION AND IN INTERNAL COMBUSTION ENGINES

by

Chan-Woo Park

A dissertation submitted in partial fulfillment
of the requirements for the degree of
Doctor of Philosophy
(Mechanical Engineering)
in The University of Michigan
2000

Doctoral Committee:

Professor Massoud Kaviany, Chairperson
Associate Professor Claus Borgnakke
Professor Gerard M. Faeth
Professor Gene Smith

The LORD is my shepherd, I shall not be in want. He makes me lie down in green pastures, he leads me beside quiet waters, he restores my soul. He guides me in paths of righteousness for his names's sake.

Psalms 23:1-3

To my parents
and my wife Young-Shin and my daughters Jiwon, Chaewon

ACKNOWLEDGEMENTS

I would like to thank all those who helped me in completing this thesis. First I want to thank Professor Massoud Kaviany for his constant encouragement and showing me a scholastic example. The committee members, Professors Claus Borgnakke, Gerard M. Faeth, and Gene Smith, for their time and interest in being part of my committee. Mr. John Clarke and Dr. Allen J. Ferrenberg for the valuable discussions. My friends in the porous media laboratory, Dr. Scott G. Liter, Dr. Amir A. M. Oliveira, Minas M. Mezedur, Ozgur Karagozoglu, Leslie B. King for the sharing of the memorable time and valuable discussion. Dr. Jinyong Jung, Jinyong Joo, Hooseok Lee, and other friends in Ann Arbor. Especially, all those including pastor Isaac Shin, Deacon Woongchul Yang, Charles H. Lee, and YoungShin Hyun and all past and current sok members in Ann Arbor Korea United Methodist Church for their support and wonderful fellowship. Rev. Mija Chae, Rev. Andrew Yoo and my missed brothers and sisters in Han Yang ESF for their faithful spiritual support and prayers. Furthermore, I would like to thank my parents, father-in-law (in memory) and mother-in-law for their unconditional love. Brothers, sister and sisters-in-law for their unforgettable support and encouragement, and my loving wife Young-Shin and my gifts from God, daughters Jiwon and Chaewon for their devoted love and for bringing me joy and happiness. Finally I thank God for loving, teaching and guiding me to be his good servant all the time till now and beyond.

TABLE OF CONTENTS

LIST OF FIGURES

LIST OF TABLES

Table

NOMENCLATURE

a	length (mm) or frequency factor (s^{-1}) or exponent
$a, b, \ldots f$	coefficients of insert motion
A	area (m^2) or air
A_g	cross-sectional area of gas phase $\pi D_1^2/4$ (m^2)
A_r	surface area for surface radiation $\pi D_1 \Delta x$ (m^2)
A_s	cross-sectional area of solid phase $\pi(D_2^2 - D_1^2)/4$ (m^2)
A_{sg}	interfacial surface area $\pi D_1 \Delta x$ (m^2)
BDC	bottom dead center
B_M	mass transfer number
c_p	specific heat capacity (J/kg-K)
C	heat capacity ratio $\rho c_p/(\rho c_p)_g$
C_D	drag coefficient
d	diameter (m)
D	diameter (m)
D_1, D_2	inside and outside diameter (m)
D_m	diffusion coefficient (m^2/s)
E_b	blackbody emissive power (W/m^2)
F	fuel or force (N)

F_{i-j}	view factor
J_e	current (A)
k	thermal conductivity (W/m-K)
K	permeability (m^2)
l	thickness (m)
l_s	tube wall thickness $(D_2 - D_1)/2$ (m)
L	length (m)
Le	Lewis number $D_m/\alpha_g = (\rho c_p)_g D_m/k_g$
M	molar weight (kg/kmole) or mass (kg)
$\dot{M}$	mass flow rate (kg/s)
n	n-type material or number of grid nodes or particle density per a parcel ($1/m^3$)
$\dot{n}_{r,P}$	volumetric production rate of species P (kg/m^3-s)
N	rpm (rot/min) or number of nodes or number of parcels
N_t	number of thermoelectric tube
Nu_D	Nusselt number based on D
Nu_e	external Nusselt number
p	p-type material or pressure (Pa)
P	combustion product species
Pr	Prandtl number
q	heat flux (W/m^2)
Q	heat flow rate (W)

Q_k	conduction heat flow rate (W)
Q_{ku}	surface-convection heat flow rate (W)
Q_r	surface radiation heat flow rate (W)
Q_u	convection heat flow rate (W)
r	radial axis (m)
r_c	compression ratio
R	thermal resistance (K/W)
R_e	internal electrical resistance per a tube (Ohm)
$R_{e,o}$	external electrical resistance (Ohm)
R_g	universal gas constant 8.3145 kJ/kmole-K
Re_D	Reynolds number based on D
$\dot{S}$	energy conversion rate (W)
Sc	Schmidt number
sfc	specific fuel consumption (g/kW-hr)
Sto	Stoke number
t	time (s)
T	temperature (K)
TDC	top dead center
u	velocity (m/s)
$\langle u \rangle_g$	average gas velocity (m/s)
V	volume of gas and solid phases (m^3)
W	work (J)

$\dot{W}$	power (W)
x	coordinate axes (m) or partial pressure
x_{cs}	coordinate of control surface of a grid (m)
Y	species concentration
Z_e	figure of merit of the thermoelectric material $\alpha_S^2/(\rho_e k_{TE})$ (1/K)

Greek

α	absorption coefficient or filtration efficiency
α_S	Seebeck coefficient (V/K)
δx	distance between nodes (m)
ΔE_a	activation energy (kJ/kmole)
Δh_{lg}	heat of the phase change (J/kg)
$\Delta h_{r,\mathrm{F}}$	heat of reaction of fuel (J/kg-fuel)
Δp	pressure drop (Pa)
ΔT	temperature difference (K)
ΔT_s	$T_{s,h} - T_{s,c}$ (K)
Δx	length of nodal control volume (m)
$\Delta\varphi$	voltage (V)
ϵ	emissivity or radiation or porosity
ϵ_r	emissivity
η	conversion efficiency $\dfrac{J_e^2 R_{e,o}/N_t}{-\Delta h_{r,\mathrm{F}}\rho_{\mathrm{F},o}\langle u\rangle_{g,o}A_g}$
η_T	thermal efficiency, see Equation (3.29)
ν	stoichiometric coefficient

μ	viscosity (Pa - s)
ρ	density (kg/m^3)
ρ_e	internal electric resistivity (Ohm-m)
θ	crank angle (degree)
σ_{SB}	Stefan-Boltzmann constant 5.670×10^{-8} W/m^2-K^4
Σ	summation
τ_c	period of reciprocation (s)
Φ	stoichiometric ratio

Superscripts

a	exponent
f	fluid phase

Subscripts

0	first surface node
$1, 2, .., n+2$	node index
a	activation or air or actual
ad	adiabatic
A	surface or air
b	blackbody or bottom gas zone or bulk
B	cylinder bore
c	cold or combustion or cycle or compression or clearance or cooling or critical
cb	cylinder block

ch	cylinder head
cs	control surface
C	combustion
d	droplet or displacement or divergence
D	diameter
e	electric or external or east or exhaust or end or emission
evp	evaporation
exh	exhaust
f	fluid
F	fuel
g	gas phase
h	hot or heating
i	node index or porous insert or intake
id	ignition delay
in	indicated variable
inj	fuel injection
ins	porous insert
int	intake
j	node index
J	Joule
k	conduction
ku	surface convection

l	left or liquid
lg	liquid-gas
$loss$	loss
L	last surface node
m	mass diffusion or mass
max	maximum
mep	mean effective pressure
mix	mixture
M	mass
n	n-type material or last node or ambient
o	reference or outgoing
opt	optimum value
O	oxidant
p	pressure or p-type material or piston or pore or plug flow
P	Peltier or product species
r	radiation or reaction or right
R	reactant species
s	solid phase or start or particle or stoichiometric
sf	solid-fluid interface
sfc	specific fuel consumption (g/kW-hr)
sg	solid-gas interface or saturation gas
sl	solid-liquid phase change

st	stoichiometry
S	Seebeck
SB	Stefan-Boltzmann
SM	Sauter mean diameter
t	tube or top gas zone or thermal or total
T	thermal or isentropic
TE	thermoelectric
u	convection
v	vapor or valve or volume
w	west or cooling water
x	x-component

Other symbols

$\langle\ \rangle$	local spatial averaged
$\overline{\ }$	time averaged
$[\ ]$	species concentration (mol/cm^3)
∞	surroundings
*	dimensionless quantity

ABSTRACT

Presence of bounding solid surfaces and reciprocation of the stream direction, allow for heat storage/release (thermal regeneration) in fluid streams undergoing an exothermic reaction (combustion). Direct fuel injection also allows for the control of the flame location, and therefore, ideally unlimited excess (above the adiabatic) temperature (called the superadiabatic temperature). While improvements in the surface-convection heat transfer and the ability of the solid to store/release heat are desirable, the solid thermal conductivity hinders performance. Porous solids (foams, tube bundles etc.), however, provide a way to avoid the difficulties. This superadiabatic temperature can be used, among other applications, to increase the efficiencies of thermoelectric power generation and internal combustion engines. These two examples are modeled and analyzed here in detail and the possibilities and limitations of using different porous materials are discussed.

Using silicon-based, high-temperature thermoelectric materials (such as $Si_{0.7}Ge_{0.3}$), a combustion-thermoelectric tube bundle is designed. The air stream reciprocates through the tubes having a short, central adiabatic methane-gas injection region and two (one on each end) thermoelectric regions (with the p- and n-type materials placed co-axially). The hot-junction temperature is only limited by the melting temperature of the silicon-germanium alloy, and through optimization of the parameters,

an efficiency of about 11 percent is obtained.

An existing design using an in-cylinder, reciprocating SiC-foam regenerator in the Diesel internal combustion engine is analyzed to take advantage of the superadiabatic temperature. The intake air is heated in the regenerator, before entering the droplet-fuel injection region and this results in an enhanced evaporation and a more uniform fuel distribution (due to deflection of the droplets by the air emanating from the regenerator). Through optimization of the regenerative cooling/heating strokes, it is confirmed that the thermal efficiency of the engine can be noticeably improved.

CHAPTER I

INTRODUCTION

Presence of the bounding solid surfaces and the reciprocation of the stream direction, allow for heat storage/release (thermal regeneration) in fluid streams undergoing an exothermic reaction (combustion). The thermal regeneration results in excess (above the adiabatic) temperature (called the superadiabatic temperature) (Weinberg, [16], Hoffmann et al. [5, 28], Hanamura et al. [26]). Whereas enhancing the surface-convection heat transfer and the ability of the solid to store/release heat are desirable, solid conductivity hinders the performance. In contrast, the use of porous solids (foams, tube bundles etc.) helps to avoid this difficulty. Direct fuel injection also allows for the control of the flame location, and therefore, capability to ideally reach unlimited superadiabatic temperatures (Kesting et al. [9]). These superadiabatic temperatures can be used to increase the efficiencies of thermoelectric power generation and internal combustion engines (Echigo et al. [3], Ferrenberg, [22, 23, 24]) among other. The pre-combustion processes of the fuel vaporization and fuel-air mixing are enhanced by the superadiabatic temperature and the flow turbulence. The fuel droplet impingement on the hot regenerator surface (above the Leidenfrost temperature) and the heated air emanating from the porous regenerator, also promote fuel evaporation and fuel vapor-air mixing in the mixing-controlled

reactions.

Depending upon the flow arrangement and the method of fuel introduction, the reacting streams are classified into (a) premixed-unidirectional, (b) premixed-reciprocating, and (c) fuel injected-reciprocating streams. Limitations of these arrangements are shown in Figure 1.1.

In a premixed-unidirectional reacting stream, as shown in Figure 1.1(a), the superadiabatic temperature is due to heat recirculation by solid-phase conduction $\mathbf{q}_k$ and radiation heat transfer $\mathbf{q}_r$, prior to the reaction region and toward the cold, unburned gas (Yoshizawa et al. [38], Sahraoui and Kaviany [34]). In such an arrangement, the burning speed and the flame location are strongly influenced by this heat recirculation. While the premixed-reciprocating flow, as shown in Figure 1.1(b), increases the superadiabatic temperature significantly compared to that of the premixed-unidirectional arrangement, the superadiabatic temperature and the flame location are determined by the ignition of the premixed fuel mixture (Hanamura et al. [26]). The heat content of the exhaust gas can be regenerated by surface-convection heat transfer $\mathbf{q}_{ku}$ and heat storage/release in the solid (with no need for the conduction and radiation heat transfer which are the main mechanisms for the heat recirculation of the unidirectional flow).

In direct fuel-injection into reciprocating oxidant flows, as shown in Figure 1.1(c), the flame temperature can be ideally increased without limit. However, there are practical limits due to effects of gas dissociation/ionization (caused by the ideally unlimited preheating of the oxidant stream), melting of the solid, and the formation of undesirable pollutants such as NOx (Weinberg, [16], Kesting et al. [9]).

In unidirectional flows, separate heat recuperation is needed, whereas in reciprocating flows, the bounding solid phase itself is used as the direct contact heat

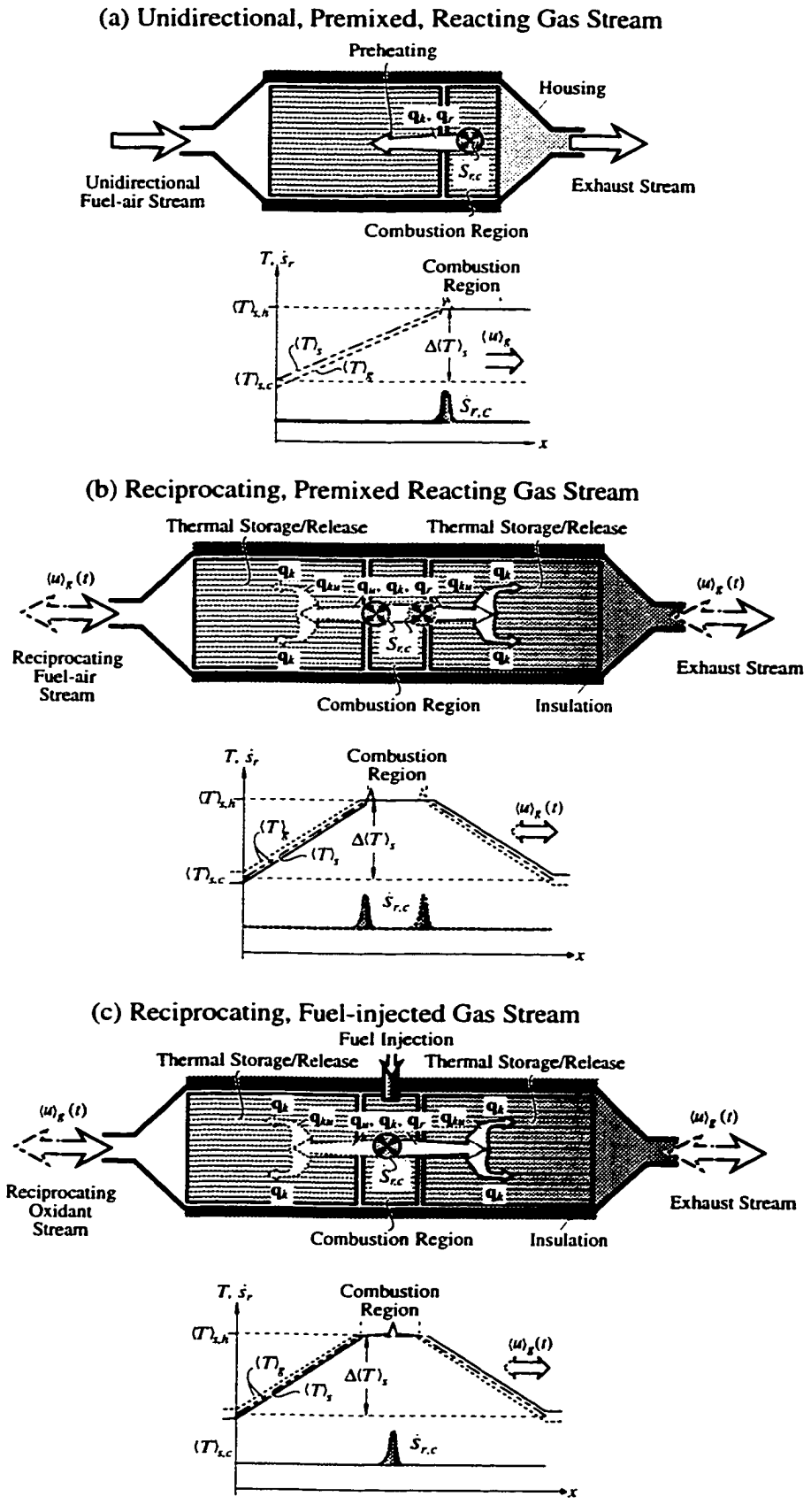

Figure 1.1: Rendering of the unidirectional and reciprocating streams with fuel injection and with premixed fuel-oxidant.

exchanger to store heat which allows for a more effective heat exchange.

The superadiabatic combustion caused by thermal regeneration can be used in low calorific, fuel-injection, reciprocating reacting streams demanding high thermal efficiencies. Examples are high temperature radiant burners (Kesting et al. [9]), fixed-bed catalytic reactors (Matros and Bunimivich [10]), and the pollutant after-treatment system of regenerative soot filtration (Athanasios and Margaritis [1]). Two examples, the thermoelectric-combustion tube and the regenerative Diesel engine, using thermal regeneration and fuel injection in reciprocating reacting streams, are analyzed here.

1.1 Combustion-Thermoelectric Tube

The first problem considered is the combustion-thermoelectric tube which generates electrical power using heat released from combustion. Hanamura et al. [26] have designed a premixed, reciprocating stream-porous medium system to create local superadiabatic temperatures. The release of the heat of combustion in the gas phase is followed by solid-gas interfacial heat transfer and then heat storage/release, with some solid-phase conduction and radiation. The interfacial heat transfer to the upstream cold gaseous stream completes the heat recirculation and the formation of local, superadiabatic temperatures in the flame region (Min and Shin [11], Sahraoui and Kaviany [34], Hoffmann et al. [5, 28]). The important roles of the interfacial surface area per unit volume, the Nusselt number, and the frequency of flow reciprocation, to this heat recirculation process are evident. Compared to the unidirectional flow arrangement used for achieving a superadiabatic flame temperature by solid conduction (and surface radiation), the reciprocation of the flow allows for heat recirculation using the storage/release of the thermal energy in the solid.

The lack of any solid conductivity and any surface radiation would assist the process.

Echigo et al. [3], have also suggested that the superadiabatic temperature of such a system can be exploited for thermoelectric energy conversion by placing the hot junction in the flame region and the cold junction in the entrance region (one on each side). A relatively short combustion region separates the two thermoelectric regions. Critical to the high efficiency of this combustion-thermoelectric system is the solid conductivity in the thermoelectric region. The currently available high-temperature thermoelectric materials (Rowe [13]), have relatively high figure of merits (e.g., Si-Ge alloy) but they also have relatively high thermal conductivities which prevents high energy-conversion efficiencies. These high-temperature ceramics (or semi-metals) are fabricated from powders and the effective conductivity of the sintered powder mixture is much smaller than the bulk thermal conductivity of each of the components and depends on their grain sizes. It has been shown by Chen [2] that the effective conductivity can be reduced by using very fine grains. Nevertheless, the search for low conductivity thermoelectric materials continues.

The use of direct fuel injection, compared to premixing, allows for a better control of the flame location and further increases the maximum gas and solid temperatures, avoiding any premature ignition (Kesting et al. [9]).

Here, in order to identify the potential and limitations of this energy conversion system, a combustion-thermoelectric tube is introduced and analyzed. The tube is shown in Figure 1.2(a) and a bundle of the combustion-thermoelectric tubes with its electrical connections is also shown in Figure 1.2(b). The reciprocating oxidant (here air is used) stream is represented by a radially averaged fluid velocity $\langle u \rangle_g(t)$ which alters in direction at the end of each half cycle. The tube consists of two thermoelectric regions (designated by TE) and one combustion region (designated

by C). The combustion region is much shorter than each of the thermoelectric regions. The tube inside and outside diameters are uniform throughout. In the thermoelectric region, the tube wall is made of a layer of p-type and a layer of n-type semiconductor materials with a very thin (negligible thickness) dielectric layer (such as a silicon dioxide) separating these two layers. The thermoelectric and combustion regions are connected with an assumed negligible thermal contact resistance.

The fuel (gaseous methane) is injected laterally in the short combustion region. Due to the small diameter of the tube (on the order of one millimeter), the fuel is expected to rapidly mix over a short distance. Using radial diffusion only, the distance needed for the penetration of the fluid supplied at the periphery is $0.01\langle u\rangle_{g,o}D_1^2/D_m$. For the range of $\langle u\rangle_{g,o}$, D_1, and D_m (and T_g) considered here, this distance is less than the tube diameter D_1. Also, due to the high temperature of the combustion region and the availability of the oxidant (i.e., low stoichiometry, fuel-limited combustion), the fuel is expected to be completely burned.

There are geometrical parameters (diameters and lengths), flow parameters (velocity and cycle period), heat transfer parameters (Nusselt number, surface emissivity), fuel parameters (stoichiometric ratio), thermoelectric material properties (Seebeck coefficient, thermal conductivity, electrical resistivity), and power-circuit parameters (external resistance). Through parametric variations, the role of these parameters on the thermoelectric energy conversion is studied using the properties of one of the current high-temperature thermoelectric materials, i.e., $Si_{0.7}Ge_{0.3}$ alloys. Finally, a further increase in the efficiency is demonstrated with a reduction of the thermal conductivity of the thermoelectric materials.

(a) A Schematic of the Combustion-Thermoelectric Tube

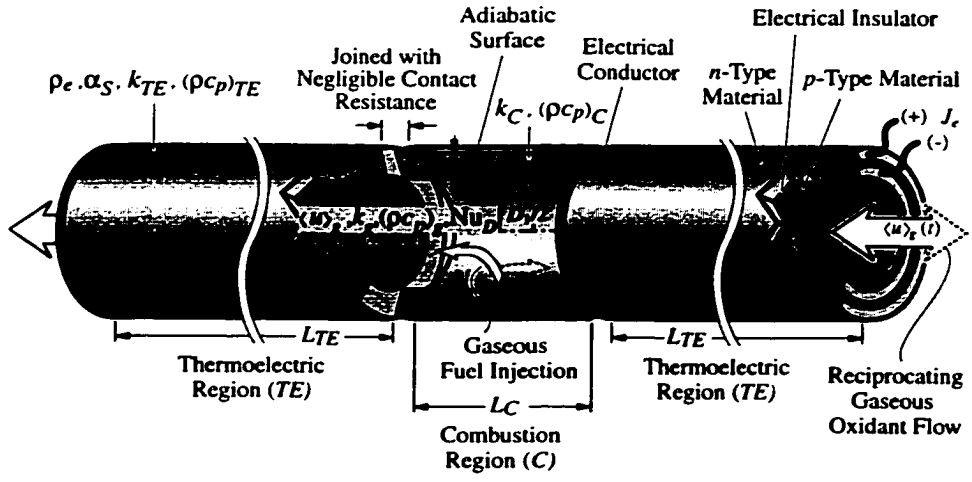

(b) Tube-Bundle Module of Combustion-Thermoelectric Energy Converter

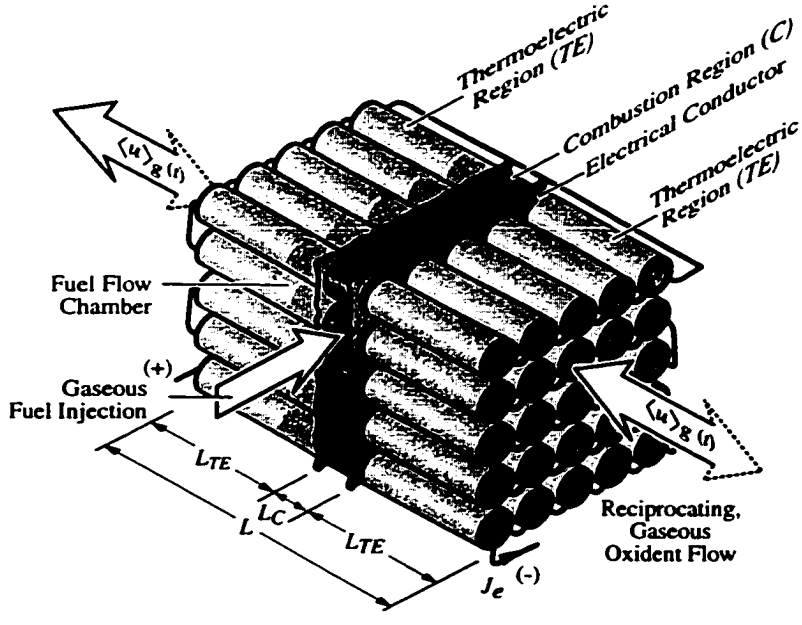

Figure 1.2: (a) A schematic of the combustion - thermoelectric tube, (b) the combustion-thermoelectric tube bundle.

1.2 Regenerative Diesel Engine

The second problem considered is a regenerative Diesel engine, which uses an in-cylinder, reciprocating porous regenerator. This regenerative engine has the potential to improve fuel-air mixing, combustion and fuel evaporation processes, and the thermal efficiency (Clarke, [20], Ferrenberg, [22], [23], Ferrenberg et al., [24]). The regenerative engine is shown in Figure 1.3. The porous insert is attached to a rod and moves within the cylinder, synchronized, but out of phase with the piston. During the regenerative heating stroke, the regenerator moves toward the piston and during the regenerative cooling stroke, the regenerator moves away from the piston. Following the combustion and expansion processes, the products of combustion (exhaust gases) retain an appreciable sensible heat. During the regenerative cooling stroke, the hot exhaust gas flows through the regenerator and stores part of this sensible heat by surface-convection heat transfer in the regenerator (which has a large surface area). Since the cold air flows through the insert and is heated after the intake is closed (during the regenerative heating stroke), then the volumetric efficiency is not affected. The superadiabatic flame temperature (due to the thermal regeneration of the combustion heat) (Hanamura et al., [26], Hoffman et al., [28], Park and Kaviany, [33], Sahraoui and Kaviany, [34], Yoshizawa et al., [38]) and the fuel droplet-regenerator interaction enhance the fuel evaporation. A uniform fuel vapor distribution is possible due to the deflection of the fuel droplets by the air flow emanating from the porous regenerator and this can improve combustion.

A multi-gas zone model and a one-dimensional model for the solid phase are used in the analysis. A droplet-tracking model is used to determine the fuel evaporation rate. The filtration model and a film evaporation model of the impinging fuel droplet

on the porous regenerator are used to examine the effect of the regenerator on the enhanced fuel evaporation. The fuel and oxidant concentrations in the top region of the engine cylinder are included in an Arrhenius combustion model for the heat release rate.

Here the effect of the thermal regeneration and the superadiabatic combustion on the thermal efficiency is examined, i.e., seeking improved regenerative engine performance.

(a) Physical rendering of Diesel engine with porous regenerator and movement of regenerator through a complete cycle (720° crank angle cycle)

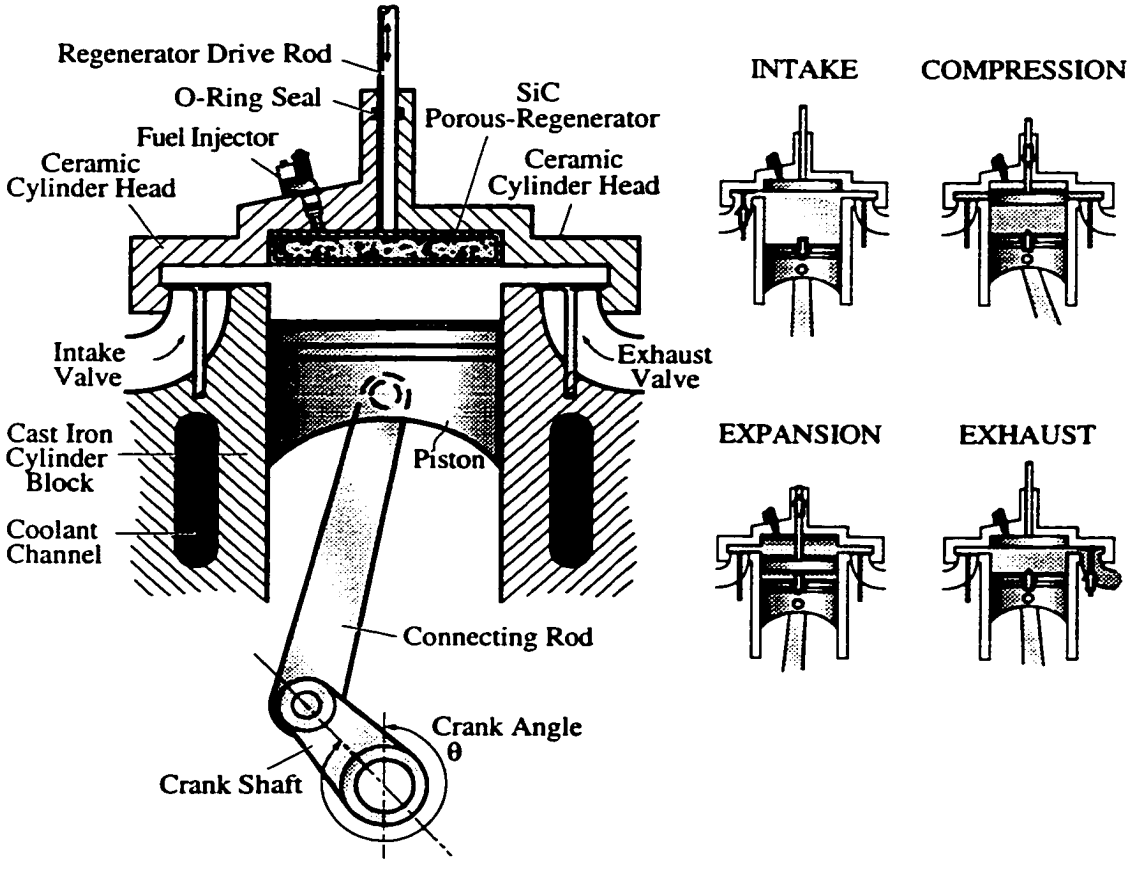

(b) Motion of the Regenerator through a complete cycle (720° crank angle cycle)

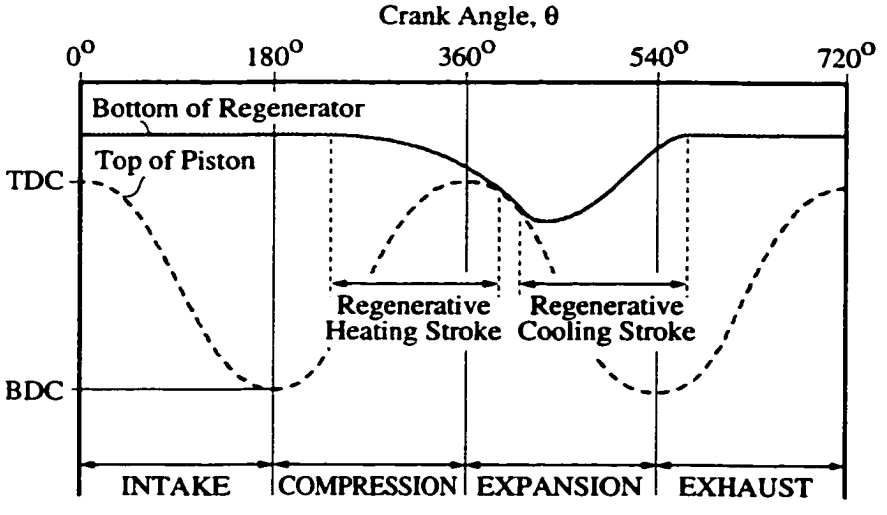

Figure 1.3: (a) Physical rendering of Diesel engine with porous regenerator and movement of regenerator and piston through a complete cycle (720° crank angle cycle). (b) Motion of regenerator through a complete cycle (720° crank angle cycle)

1.3 Scope and Limitations

The objective of the investigation is to analyze the effect of thermal regeneration using time periodic, reacting gas streams in power generation systems. The regenerator is a porous medium, selected for the required properties. The relevant conservation equations and relationships are solved numerically.

Gas dissociation/ionization becomes significant at very large gas temperatures, but this effect is not considered here. The porous medium (the solid matrix) is assumed to be inert (i.e., not participating in the reactions).

It is assumed that in the combustion-thermoelectric tube, the dielectric layer between the p- and n-type thermoelectric materials has a negligible thickness and that there is the perfect electrical insulation and thermal contact. It is also assumed that the methane-gas is injected into the combustion region at high temperature, without considering any pyrolysis to soot.

For the regenerative Diesel engine, it is assumed that the regenerator is actuated by a cam mechanism. The effects of the regenerator rod volume and heat transfer through the rod are neglected. It is also assumed that the intake and exhaust valves are located in the side wall and that the extra volume due to the valves is negligible. While a perfect mixing of the fuel vapor and air is assumed in the top and bottom gas regions, the gas phase in the porous regenerator is axially divided into small-finite volumes.

CHAPTER II

COMBUSTION-THERMOELECTRIC TUBE

2.1 Motivation, Background, Scope, and Objectives

Local, superadiabatic temperatures result from gas preheating (i.e., heat recirculation) of the unidirectional reacting flow, which is due to conduction and radiation heat transfer in the solid matrix (Yoshizawa et al. [38], Sahraoui and Kaviany [34]). Hanamura et al. [26] have designed a premixed, reciprocating fluid flow-porous medium system to create such superadiabatic temperatures. Echigo et al. [3], have also suggested that the superadiabatic temperature of such a system can be exploited for thermoelectric energy conversion by placing the hot junction in the flame region and the cold junction in the entrance region.

Critical to the high efficiency of the combustion-thermoelectric system is the solid conductivity in the thermoelectric region. The currently available high-temperature thermoelectric materials (Rowe [13]), have relatively large figure of merits (e.g., Si-Ge alloys), but they also have relatively large thermal conductivities which prevents high energy-conversion efficiencies.

The use of direct fuel injection, compared to premixing, allows for a better control of the flame location and further increases the maximum gas and solid temperatures by avoiding any premature ignition (Kesting et al. [9]). The fuel (gaseous methane)

is injected laterally in a short combustion region.

Here, in order to identify the potential and limitation of this energy conversion system, a combustion-thermoelectric tube is introduced and analyzed as shown in Figure 2.1(a). The tube consists of two thermoelectric regions (designated by TE) and one combustion region (designated by C). The tube inside and outside diameters are uniform throughout. In the thermoelectric region, the tube wall is made of a layer of p-type and a layer of n-type semiconductor materials with a very thin (negligible thickness) dielectric layer (such as a silicon dioxide) separating these two layers. The reciprocating oxidant (here air is used) stream is represented by a radially averaged fluid velocity $\langle u \rangle_g(t)$ which alters in direction at the end of each half cycle. The gaseous fuel is injected laterally in the short combustion region. Due to the small diameter of the tube (on the order of one millimeter), the fuel is expected to rapidly mix over a short distance.

The analysis must consider geometrical parameters (diameters and lengths), flow parameters (velocity and cycle period), heat transfer parameters (Nusselt number, surface emissivity), fuel parameters (stoichiometric ratio), thermoelectric material properties (Seebeck coefficient, thermal conductivity, electrical resistivity), and power-circuit parameters (external resistance). Through parametric variations, the role of these properties on thermoelectric energy conversion is studied using the properties of one of the current high-temperature thermoelectric materials, i.e., $Si_{0.7}Ge_{0.3}$ alloys.

2.2 Analysis

A one-dimensional model for the solid and gas phases is used for the analysis of the combustion-thermoelectric tube. Radially averaged temperatures are used for the

(a) A Schematic of the Combustion-Thermoelectric Tube

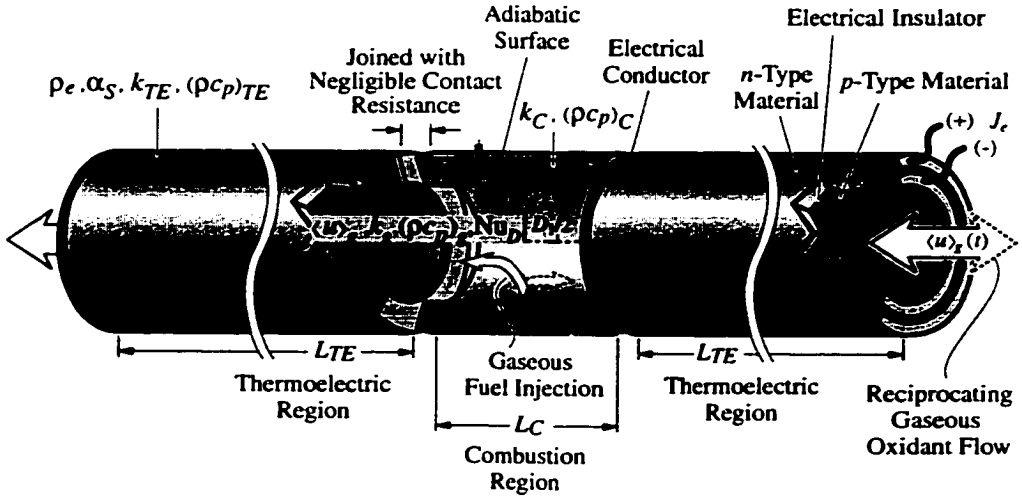

(b) Thermal Nodal Model of Combustion-Thermoelectric Tube

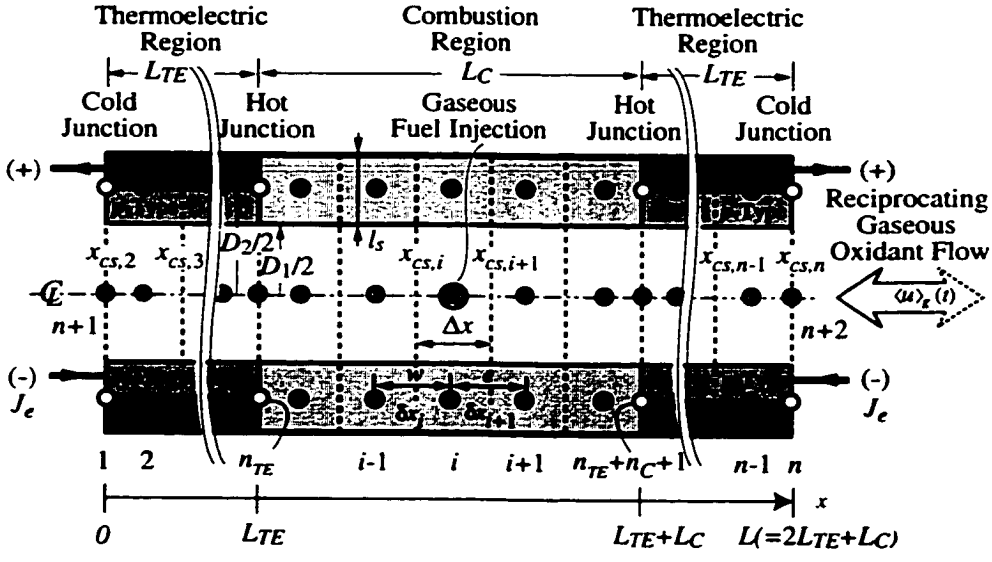

Figure 2.1: (a) A schematic of the combustion-thermoelectric tube. (b) Thermal nodal model of the combustion-thermoelectric tube.

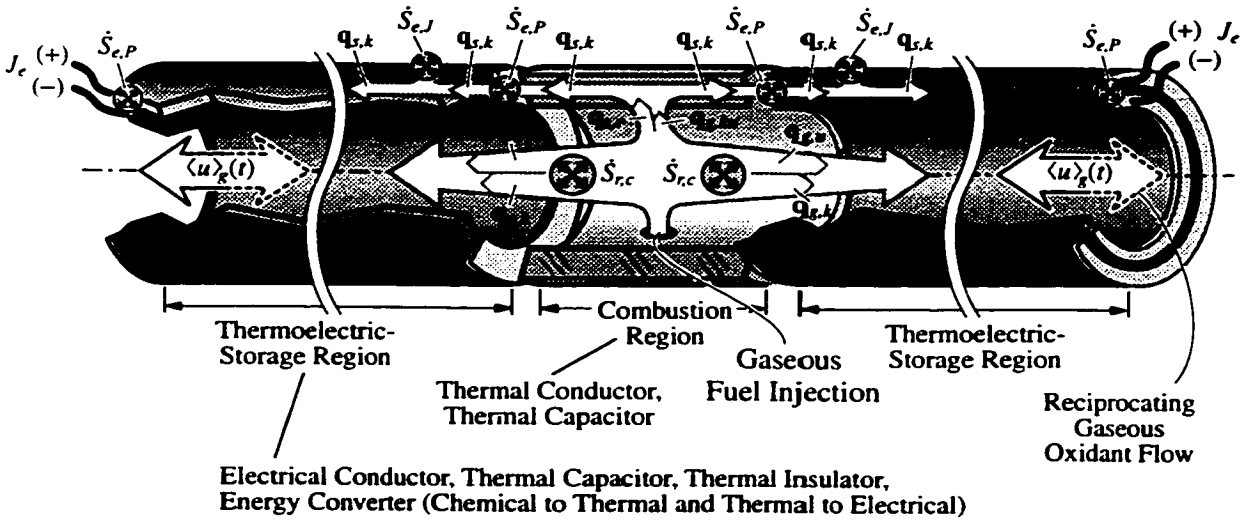

Figure 2.2: Heat flux vector tracking for the combustion-thermoelectric tube.

gas and solid phases. The heat flux vector tracking for the combustion-thermoelectric tube is shown in Figure 2.2. The mechanisms of the heat transfer considered include the surface-convection, conduction and solid surface radiation. The thermoelectric and combustion regions are connected with an assumed negligible thermal contact resistance.

The various regions are axially divided into small, finite volumes. These volumes are shown in Figure 2.1(b). The surface nodes are shown with open circles and they are at the cold and hot junctions, i.e., at $i = 1$, n_{TE}, $n_{TE} + n_C + 1$, and n. Constant thermophysical properties and a unity Lewis number (Le = 1), are assumed.

Using the radially averaged velocity $\langle u \rangle_g$, the mass conservation equation for the gas phase is

$$A_g \Delta x \frac{d\rho_{g,i}}{dt} = (\rho A \langle u \rangle)_{g,w,i} - (\rho A \langle u \rangle)_{g,e,i}. \tag{2.1}$$

The density is given by the ideal gas law, $\rho_g = pM_g/R_g T_g$, and a constant, atmospheric pressure is assumed.

The finite-volume species mass conservation equation for the product-species P in i gas-phase node is

$$A_g \Delta x \frac{d\rho_{\mathrm{P},i}}{dt} = A_g[(\rho_{\mathrm{P}}\langle u\rangle_g)_{w,i} - (\rho_{\mathrm{P}}\langle u\rangle_g)_{e,i}] + D_m A_g(\frac{\rho_{\mathrm{P},i-1} - \rho_{\mathrm{P},i}}{\delta x_i} - \frac{\rho_{\mathrm{P},i} - \rho_{\mathrm{P},i+1}}{\delta x_{i+1}}) + \dot{n}_{r,\mathrm{P},i} A_g \Delta x, \tag{2.2}$$

where i is the axial node index.

For the product species generation terms $\dot{n}_{r,\mathrm{P},i}$, a first-order, Arrhenius relation (Yoshizawa et al. [38]) is used, i.e.

$$\dot{n}_{r,\mathrm{P},i} = a_r(\rho_{g,i} - \rho_{\mathrm{P},i})e^{-\frac{\Delta E_a}{R_g T_{g,i}}}, \tag{2.3}$$

where $\rho_{g,i} = \rho_{\mathrm{R},i} + \rho_{\mathrm{P},i}$, $\rho_{\mathrm{R},i} = \rho_{\mathrm{F},i} + \rho_{\mathrm{O},i} = \rho_{g,i} - \rho_{\mathrm{P},i}$ is the local reactant density in the gas phase. Since the amount of the injected fuel (2.36 percent of the oxidant mass flow rate for the baseline conditions) is small, it is assumed that the injected fuel is well mixed and the change in ρ_g due to the fuel injection is negligible and a premixed reaction begins after the injection.

The two medium model is used here to allow for the thermal nonequilibrium caused by the gaseous combustion. The radially averaged temperatures $\langle T\rangle_r^g = T_g$ and $\langle T\rangle_r^s = T_s$ are used, where $\langle\ \rangle_r^g$ and $\langle\ \rangle_r^s$ indicate radially, phase averaged quantities (Kaviany [7]).

The finite-volume energy conservation equation for the i gas-phase node [shown in Figure 2.1(b)] is

$$A_g \Delta x \frac{d}{dt}(\rho c_p T)_{g,i} = Q_{g,u,i} + Q_{g,k,i} + Q_{g,ku,i} + \dot{S}_{r,c,i}, \tag{2.4}$$

where

$$Q_{g,u,i} = (\rho c_p \langle u\rangle AT)_{g,w,i} - (\rho c_p \langle u\rangle AT)_{g,e,i} \tag{2.5}$$

$$Q_{g,k,i} = k_g A_g \left(\frac{T_{g,i-1} - T_{g,i}}{\delta x_i} - \frac{T_{g,i} - T_{g,i+1}}{\delta x_{i+1}}\right) \tag{2.6}$$

$$Q_{g,ku,i} = \mathrm{Nu}_D \frac{k_g}{D_1} A_{sg}(T_{s,i} - T_{g,i}) \tag{2.7}$$

$$\dot{S}_{r,c,i} = -\Delta h_{r,F} \frac{\nu_F M_F}{\nu_R M_R} \dot{n}_{r,P,i} A_g \Delta x. \tag{2.8}$$

The hydrodynamic dispersion is neglected, because of the small Péclet number and the dominance of the surface convection over gaseous conduction and dispersion. The energy equation for the i solid-phase node [shown in Figure 2.1(b)] is

$$(\rho c_p)_{s,i} A_s \Delta x \frac{dT_{s,i}}{dt} = Q_{s,k,i} - Q_{s,ku,i} - Q_{s,r,i} + (\dot{S}_{e,J})_i + (\dot{S}_{e,P})_i, \tag{2.9}$$

where

$$Q_{s,k,i} = k_s A_s \left(\frac{T_{s,i-1} - T_{s,i}}{\delta x_i} - \frac{T_{s,i} - T_{s,i+1}}{\delta x_{i+1}}\right) \tag{2.10}$$

$$Q_{s,ku,i} = \mathrm{Nu}_D \frac{k_g}{D_1} A_{sg}(T_{s,i} - T_{g,i}) \tag{2.11}$$

$$Q_{s,r,i} = \frac{E_{b,i} - (q_{r,o})_i}{\left(\frac{1-\epsilon_r}{A_r \epsilon_r}\right)_i} \tag{2.12}$$

$$(\dot{S}_{e,J})_i = \left[\left(\frac{\rho_e \Delta x}{A}\right)_{p,i} + \left(\frac{\rho_e \Delta x}{A}\right)_{n,i}\right] J_e^2 \qquad \text{for TE region} \tag{2.13}$$

$$(\dot{S}_{e,P})_i = \mp \alpha_S T_{s,i} J_e \qquad \text{at hot/cold junctions of TE region,} \tag{2.14}$$

where the Nusselt number, Nu_D, is taken to be for laminar, fully-developed fields, occurring $\mathrm{Re}_D < 2,300$, $\mathrm{Nu}_D = 3.66$. The Peltier heat absorption/release $(\dot{S}_{e,P})_i$ occurs at the hot/cold junctions and is used in the surface nodes.

Using simple mean beam length analysis (Siegel and Howell [35]), it can be shown that for small (order of one millimeter diameter) tubes, the gas radiation is less than one half percent of the surface radiation. The surface radiation heat flow rate $Q_{s,r,i}$ is written as

$$Q_{s,r,i} = \frac{E_{b,i} - (q_{r,o})_i}{\left(\frac{1-\epsilon_r}{A_r \epsilon_r}\right)_i} = \sum_{j=1}^{n+2} \frac{(q_{r,o})_i - (q_{r,o})_j}{\frac{1}{A_{r,i} F_{i-j}}}, \tag{2.15}$$

where $E_{b,i} = \sigma_{SB} T_{s,i}^4$ is the total hemispherical blackbody emissive power. The inlet ($i = n+1$) and outlet region ($i = n+2$) of the tube as shown in Figure 2.1(b), are treated as imaginary blackbody surfaces. The view factor $F_{i\text{-}j}$ is obtained by the kernel approximation (Min and Shin [11], Siegel and Howell [35]) and is

$$F_{i\text{-}j} = \frac{D_1}{4\Delta x}[e^{\frac{2(x_{cs,i}+\Delta x)}{D_1}} - e^{\frac{2x_{cs,i}}{D_1}}][e^{-\frac{2x_{cs,j}}{D_1}} - e^{-\frac{2(x_{cs,j}+\Delta x)}{D_1}}]$$

$$i, j = 1, .., n \qquad \text{ring to another ring} \tag{2.16}$$

$$F_{i\text{-}j} = \frac{D_1}{4\Delta x}[e^{-\frac{2x_{cs,i}}{D_1}} - e^{-\frac{2(x_{cs,i}+\Delta x)}{D_1}}]$$

$$i = 1, .., n,\ j = n+1, n+2 \qquad \text{ring to end disk.} \tag{2.17}$$

Figure 2.3(a) shows a bundle of the combustion-thermoelectric tubes with its electrical connections. Figure 2.3(b) also shows the electrical circuit for such a bundle. The voltage $\Delta\varphi$ for an N_t-tube bundle shown in Figure 2.3(b), is

$$\Delta\varphi = J_e R_{e,o} = 2N_t[\alpha_S \Delta T_s - J_e(R_{e,p} + R_{e,n})], \tag{2.18}$$

where $\Delta T_s = T_{s,h} - T_{s,c}$, $T_{s,h} = (T_{s,n_{TE}} + T_{s,n_{TE}+n_C+1})/2$, $T_{s,c} = (T_{s,1} + T_{s,n})/2$, $\alpha_S = \alpha_{S,p} - \alpha_{S,n}$, $R_{e,p} = (\rho_e L/A)_p$ and $R_{e,n} = (\rho_e L/A)_n$.

For the case of $A_p = A_n = A_s/2$, $\rho_{e,p} = \rho_{e,n} = \rho_e$ and $L_p = L_n = L_{TE}$, the internal electrical resistance of the left side of a thermoelectric tube, shaded in Figure 2.3(b), is

$$R_e = R_{e,p} + R_{e,n} = (\frac{\rho_e L}{A})_p + (\frac{\rho_e L}{A})_n = 4\frac{\rho_e L_{TE}}{A_s}, \tag{2.19}$$

where A_p and A_n are the cross-sectional areas of the p-type and n-type thermoelectric materials, and A_s is the total solid cross-sectional area.

Using the voltage relation, Eq. (2.18), the current is

$$J_e = \frac{2N_t \alpha_S \Delta T_s}{2N_t R_e + R_{e,o}} = \frac{\alpha_S \Delta T_s}{R_e(1 + R_{e,o}^*)}$$

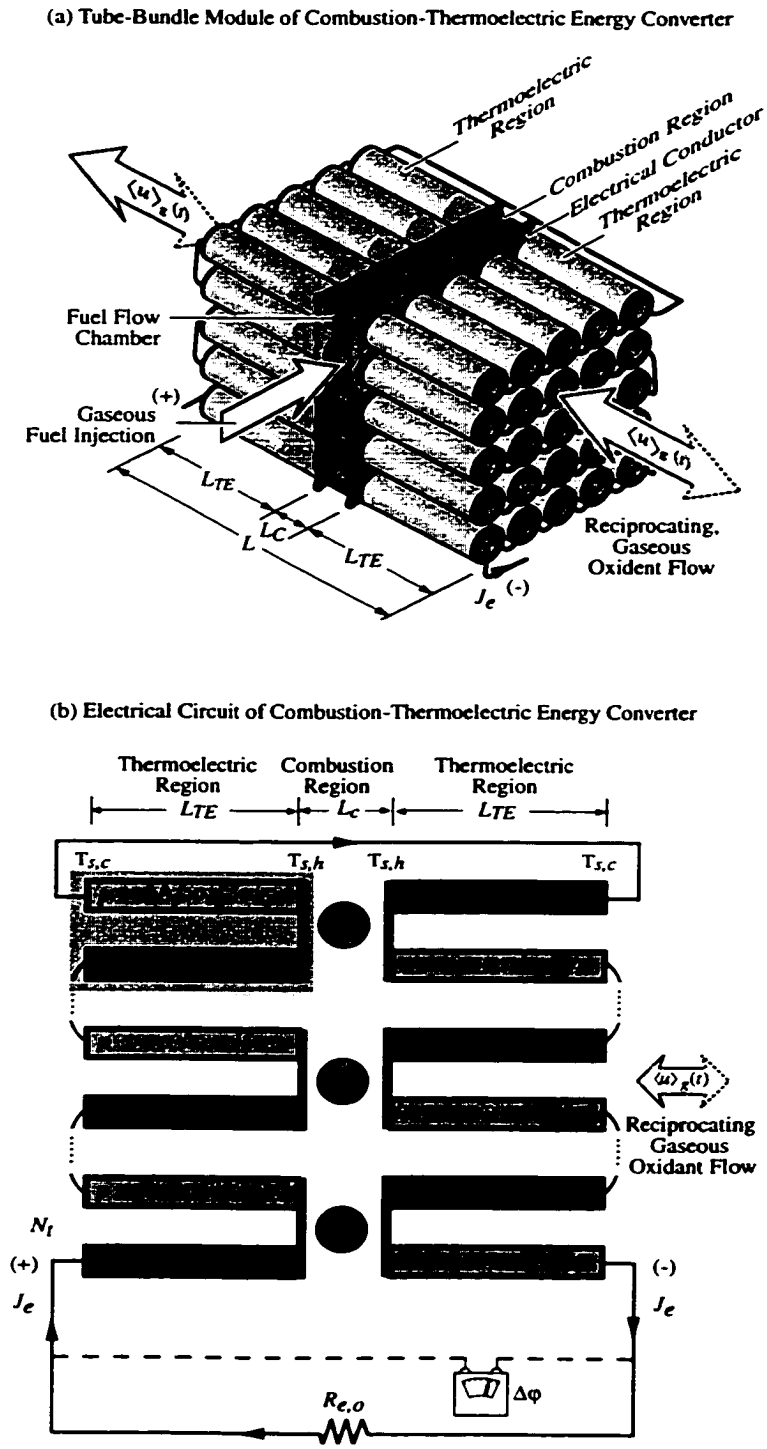

Figure 2.3: (a) Tube-bundle module of the combustion-thermoelectric energy converter. (b) Electrical circuit for the combustion-thermoelectric energy converter.

$$= \frac{\alpha_S \Delta T_s}{4\rho_e L_{TE}(1 + R^*_{e,o})} A_s, \tag{2.20}$$

where $R^*_{e,o}$ is the ratio of the external resistances to the internal resistance, i.e., $R_{e,o}/(2N_t R_e)$.

The electric power generated is

$$\begin{aligned} J_e^2 R_{e,o} &= 2N_t(J_e \alpha_S \Delta T_s - J_e^2 R_e) \\ &= N_t \frac{\alpha_S^2 \Delta T_s^2 R^*_{e,o}}{2\rho_e L_{TE}(1 + R^*_{e,o})^2} A_s. \end{aligned} \tag{2.21}$$

The gas-phase energy and species-P conservation equations for the inlet and outlet fluid nodes, for the gas flowing from left to right, are

$$-k_g A_g \frac{T_{g,1} - T_{g,2}}{\delta x_2} + (\rho c_p A)_g \langle u \rangle_g (T_o - T_{g,1}) = 0 \qquad \text{at} \quad i = 1 \tag{2.22}$$

$$T_{g,n} = T_{g,n-1} \qquad \text{at} \quad i = n \tag{2.23}$$

$$-D_m A_g \frac{\rho_{\mathrm{P},1} - \rho_{\mathrm{P},2}}{\delta x_2} - A_g \langle u \rangle_g \rho_{\mathrm{P},1} = 0 \qquad \text{at} \quad i = 1 \tag{2.24}$$

$$\rho_{\mathrm{P},n} = \rho_{\mathrm{P},n-1} \qquad \text{at} \quad i = n. \tag{2.25}$$

Similar equations are written for the gas flow from right to left.

The energy equations for the left-side cold junction is

$$-k_{TE} A_s \frac{T_{s,1} - T_{s,2}}{\delta x_2} - \epsilon_r \sigma_{SB} A_s (T_{s,1}^4 - T_o^4) + J_e \alpha_S T_{s,1} - \mathrm{Nu}_e \frac{k_g}{D_2} A_s (T_{s,1} - T_o) = 0, \tag{2.26}$$

where Nu_e is the external Nusselt number for the external air cooling at cold junctions.

A similar equation is written for the right-side cold junction.

The thermoelectric conversion efficiency is the ratio of the electric power generated to the combustion heating rate, i.e.,

$$\eta = \frac{J_e^2 R_{e,o}}{-N_t \Delta h_{r,\mathrm{F}} \dfrac{\nu_{\mathrm{F}} M_{\mathrm{F}}}{\nu_{\mathrm{R}} M_{\mathrm{R}}} \rho_g \langle u \rangle_{g,o} A_g}$$

$$= \frac{\dfrac{\alpha_S^2 \Delta T_s{}^2 R_{e,o}^*}{2\rho_e L_{TE}(1+R_{e,o}^*)^2} A_s}{-\Delta h_{r,F}\rho_{F,o}\langle u\rangle_{g,o} A_g}. \tag{2.27}$$

The power consumed for the reciprocating flow and in other components (e.g., valves), are neglected.

Considering the existence of many parameters, they are made dimensionless reducing their number. The nondimensional parameters are

$$Z_e T_o = \frac{\alpha_S^2}{\rho_e k_{TE}} T_o, \quad R_{e,o}^* = \frac{R_{e,o}}{2N_t R_e}, \quad \mathrm{Re}_D = \frac{\rho_g \langle u\rangle_{g,o} D_1}{\mu_g}$$

$$C = \frac{\rho c_p}{(\rho c_p)_g}, \qquad k^* = \frac{k}{k_g}, \qquad \Phi = \frac{\rho_{F,o}}{(\rho_{F,o})_{st}} \frac{(1-\rho_{F,o}/\rho_g)_{st}}{(1-\rho_{F,o}/\rho_g)}.$$

The magnitude for the baseline parameters (i.e., conditions) are listed in Table 2.1 (properties from Kaviany [8]). From these magnitudes, the magnitudes of the nondimensional parameters are $Z_e T_o = 0.59$, $R_{e,o}^* = 1$, $\mathrm{Re}_D = 54.5$, $C_{TE} = 1,908.8$, $C_C = 3,236.0$, $k_{TE}^* = 75$, $k_C^* = 523.6$, and $\Phi = 0.414$.

The species and energy conservation equations Eqs. (2.2), (2.4) and (2.9) are discretized with a central-difference scheme with respect to space, and an implicit-difference scheme with respect to time and are solved simultaneously using iterations (Patankar [12]). The grid-net size dependence is tested and for an 85 node (uniform gridnet), an asymptotic solution is obtained. For a typical case, the computation time is about 90 min with HP B160L. The convergence at each time step is obtained by evaluating the residues in the species and energy conservation equations and requiring the maximum resides be below 0.00001. The quasi-steady solution is obtained when the error in overall energy balance is less $1 \sim 2$ percent.

Table 2.1: Physical, chemical, and geometrical properties and the baseline magnitude of parameters.

Parameter	Magnitude
fuel (methane):	
$\rho_{F,o}$	0.02746 kg-fuel/m^3
$(\rho_{F,o})_{st}$	0.06424 kg-fuel/m^3
Φ	0.414
$\Delta h_{r,F}$	-55.53 MJ/kg-fuel
ΔE_a	131 MJ/kmole
a_r	2.8 $\times 10^8$ 1/s
T_{ad}/T_o	4.0
oxidant (air):	
$\rho_{g,o}$	1.164 kg/m^3
$c_{p,g}$	1,099 J/kg-K
k_g	0.0573 W/m-K
μ_g	369.8 $\times$ 10^{-7} N-s/m^2
$\langle u \rangle_{g,o}$	0.75 m/s
$T_{g,o}$, T_o	298 K, 298 K
Nu_D, Nu_e	3.66, 1.5
Re_D	54.5
τ_c	10 s
Le	1

Table 2.1: (Continued)

Parameter	Magnitude
tube bundle module:	
length, $2L_{TE} + L_C$	127.5 mm
cross-sectional area, $a \times a$	30×30 mm^2
number of tubes, N_t	$a^2/D_2^2 = 144$
electrical resistance ratio	$R^*_{e,o} = 1$
power generated	24.0 W, 26.7 kW/m^2
voltage	93.7 V
current	256.3 mA
thermoelectric region	
$Si_{0.7}Ge_{0.3}$:	
Z_eT_o	0.59
$\alpha_{S,p}, \alpha_{S,n}, \alpha_S(= \alpha_{S,p} - \alpha_{S,n})$	195.3, -207.3, 402.6 μV/K
ρ_e	19.1 μOhm-m
ρ_s	2,990 kg/m^3
$c_{p,s}$	816.7 J/kg-K
C_{TE}	1,908.8
k_{TE} (k^*_{TE})	4.3 W/m-K (75)
D_1	1.3 mm
l_s (D_2)	0.6 mm (2.5 mm)
L_{TE}	60 mm
ϵ_r	1.0
T_{sl}	2,000 K
combustion region	
SiC (CVD fabrication):	
ρ_s	3,160 kg/m^3
$c_{p,s}$	1,310 J/kg-K
C_C	3,236.0
k_C (k^*_C)	30 W/m-K (523.6)
L_C	7.5 mm
ϵ_r	1.0
T_{sl}	3,100 K

2.3 Results and Discussion

Typical results for the distributions of the solid- and gas-phase temperatures, the mass fraction of the combustion products, and the reaction rate at the end of a half cycle, with gas flowing from left to right, are shown in Figure 2.4. The results show that for $Si_{0.7}Ge_{0.3}$ alloy with an assumed melting temperature of $T_{sl} = 2,000$ K, the conversion efficiency is 11.3 percent and the power converted is 24.0 W, under the baseline conditions listed in Table 2.1.

As was indicated in the introduction, the pure lateral diffusion transport of the fuel is expected to occur in a very short distance. The lateral momentum of the fuel can further assist in the mixing. As shown in Figure 2.4, due to the high oxidant temperature, the flame temperature reaches a local, superadiabatic temperature right at the fuel-injection site in the combustion region. The adiabatic flame temperature T_{ad} is also shown in Figure 2.4.

The conduction heat flow towards, and the Peltier heat release at the cold junctions, are removed by the intensive external cooling [the product of the total solid cross-sectional area A_s and the external Nusselt number Nu_e is large in Eq. (2.26)]. A Nusselt number $\mathrm{Nu}_e = 150$ (based on the outside diameter) and a surface area A_s are used as a baseline values. When an extended surface (fins) is used with an area of $A = 100A_s$, the Nusselt number Nu_e is then reduced to 1.5 which can readily be achieved using low speed air flow over fins.

For $R^*_{e,o} = 1$ [obtained as the optimum value for a maximum power from Eq. (2.21)], the current is independent of the number of tubes, as evident from Eq. (2.20). The number of tubes in a tube-bundle module, which is an elemental unit circuit, is chosen to meet an electrical specifications such as a desired current-voltage.

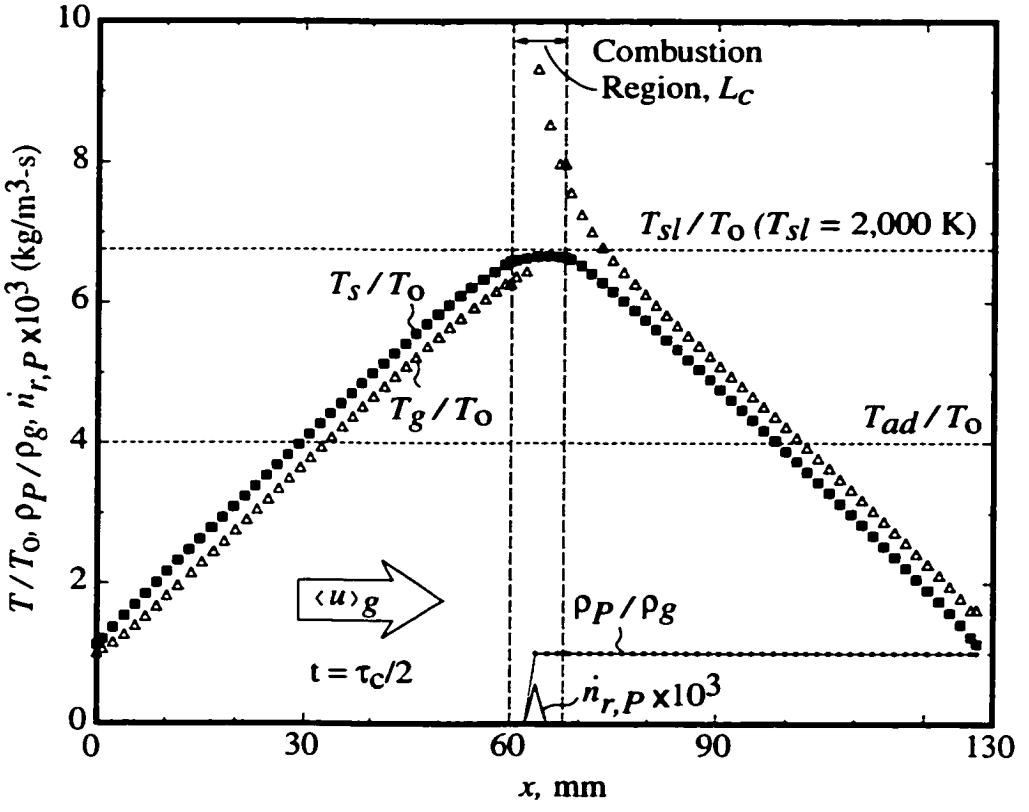

Figure 2.4: Typical axial distributions of normalized gas and solid temperatures, reaction rate, and product species mass fraction. $Z_e T_o = 0.59$, $R^*_{e,o} = 1$, $\tau_c = 10$ s, $\langle u \rangle_{g,o} = 0.75$ m/s, $D_1 = 1.3$ mm, $l_s = 0.6$ mm, $L_{TE} = 60$ mm, $L_C = 7.5$ mm, $C_{TE} = 1,908.8$, $C_C = 3,236.0$, $k^*_{TE} = 75$, $k^*_C = 523.6$, $\Phi = 0.414$.

A tube-bundle module of 144 tubes gives a current of $J_e = 256.3$ mA and a voltage of $\Delta\varphi = 93.7$ V. For nine such modules connected in parallel, the power is $J_e\Delta\varphi = 216.1$ W and the current is $J_e = 2.31$ A. Each tube-bundle module has a length $2L_{TE} + L_C = 127.5$ mm and a cross-sectional area $a \times a = 30$ (mm) $\times$ 30 (mm), in a close-pack, square-array arrangement of the tubes, giving the power density of 26.7 kW/m^2. These results are not far to the design results of the $2L_{TE} + L_C$ of 50 $\sim$ 100 mm and power density of 5 $\sim$ 10 kW/m^2 suggested by Echigo et al. [3].

2.3.1 Effect of Various Parameters

A parametric study is performed using the fluid flow, thermoelectric-region, and combustion-region parameters. The baseline conditions are listed in Table 2.1.

Figure 2.5 shows that the conversion efficiency η, defined by Eq. (2.27), and the hot and cold junction temperatures of the thermoelectric region, do not change noticeably with the cycle period τ_c. This is because the flame location is fixed at the fuel injection site and due to the intensive external cooling of the cold junction, the transient variations are diminished, as compared to the case of the premixed combustion. For mechanical maintenance purposes, less mechanical movement of the parts (e.g., valves) is desirable. Here, a longer period of $\tau_c = 10$ s is used as the baseline condition.

Figure 2.6 shows that for the gas velocities $\langle u \rangle_{g,o} > 0.75$ m/s, the efficiency no longer increases and the hot junction temperature reaches the melting temperature T_{sl}. The pressure drop under the baseline conditions is about 178 Pa, and therefore, is considered rather small.

The combustion region provides an extended surface to the hot junctions (joined with an assumed negligible contact resistance to the combustion region) for the

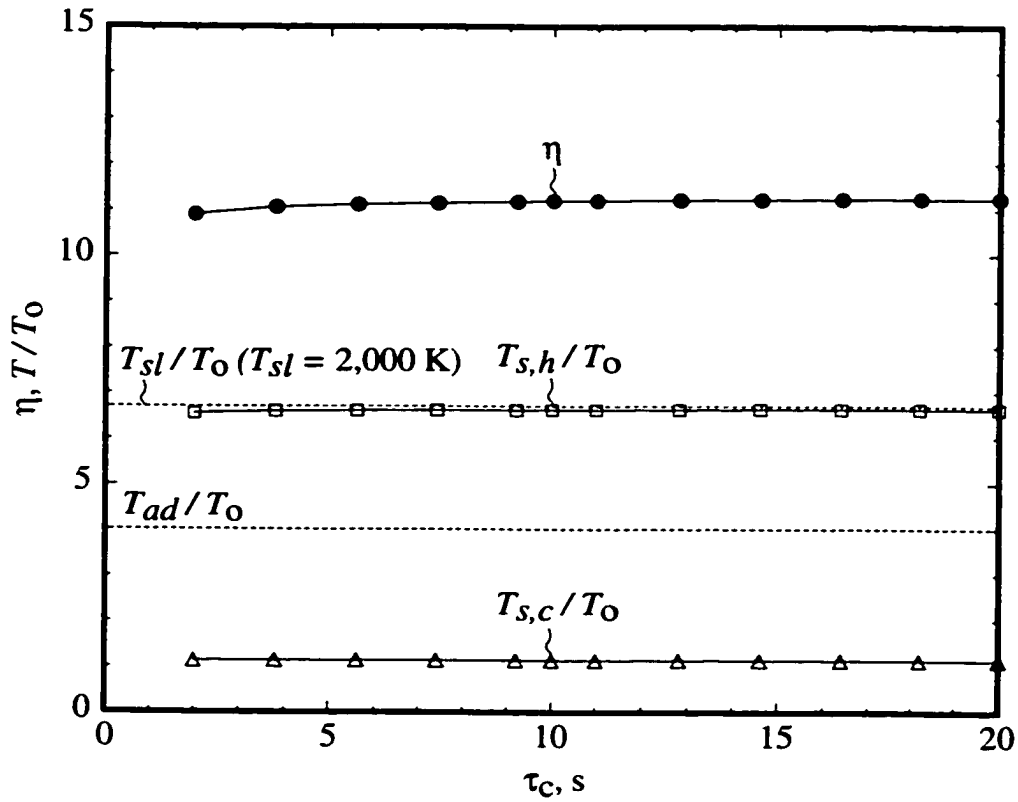

Figure 2.5: Effect of the cycle period τ_c on the conversion efficiency and the junction temperatures. $Z_eT_o = 0.59$, $R^*_{e,o} = 1$, $\langle u \rangle_{g,o} = 0.75$ m/s, $D_1 = 1.3$ mm, $l_s = 0.6$ mm, $L_{TE} = 60$ mm, $L_C = 7.5$ mm, $C_{TE} = 1,908.8$, $C_C = 3,236.0$, $k^*_{TE} = 75$, $k^*_C = 523.6$, $\Phi = 0.414$.

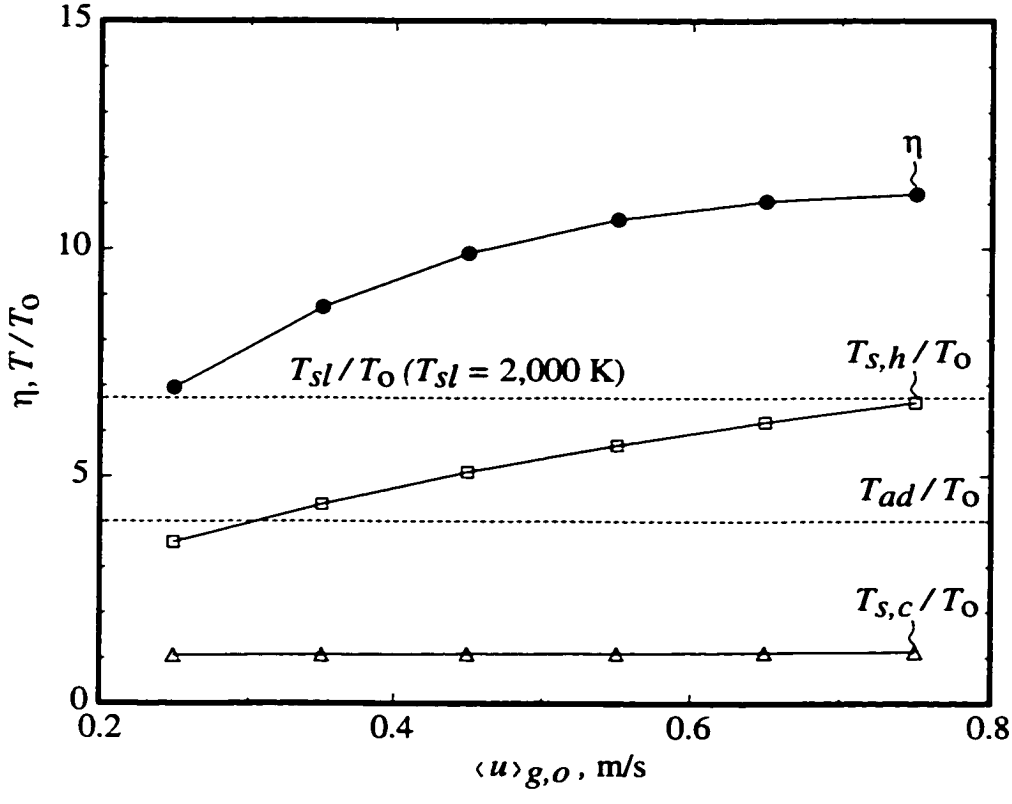

Figure 2.6: Effect of the gas velocity $\langle u \rangle_{g,o}$ on the conversion efficiency and the junction temperatures. $Z_e T_o = 0.59$, $R^*_{e,o} = 1$, $\tau_c = 10$ s, $D_1 = 1.3$ mm, $l_s = 0.6$ mm, $L_{TE} = 60$ mm, $L_C = 7.5$ mm, $C_{TE} = 1,908.8$, $C_C = 3,236.0$, $k^*_{TE} = 75$, $k^*_C = 523.6$, $\Phi = 0.414$.

transfer of the heat released by combustion. Figure 2.7 shows the effect of the combustion region length L_C (with the fuel injection located at the center of the region), on the conversion efficiency. The effect is not significant, because of the relatively high thermal conductivity for the combustion region, which results in a uniform temperature. For complete combustion, only a short combustion region is needed, i.e., $L_C = 7.5$ mm. The efficiency is not very sensitive to the thermal conductivity and the heat capacity of the combustion region. Here, SiC has been used, due to its high melting temperature. The thermal conductivity of SiC varies depending on the fabrication technique (e.g., CVD, sintered powder, etc.). Here a value close to the CVD fabrication is used (Kaviany [8]).

Figure 2.8 shows the effect of the stoichiometric ratio Φ on the conversion efficiency η, for several tube wall thicknesses. As the stoichiometric ratio increases, the efficiency and the hot junction temperatures $T_{s,h}$ increase. Above a tube wall thickness $l_s = 0.6$ mm used as the baseline value, the efficiency reaches an asymptotic value, with $T_{s,h}$ kept below $T_{sl} = 2,000$ K. The maximum flame temperature for the tube wall thickness $l_s = 0.8$ mm and 0.9 mm, are also shown in Figure 2.8. Since the maximum flame temperature depends on the gas preheating temperature (determined by the maximum temperature of the thermoelectric region, i.e., the hot junction temperature $T_{s,h}$), it is much higher than the adiabatic flame temperature. Note that due to the preheating, the flammability limit is reduced significantly. The smallest equivalence ratio for a stable flame in ceramic foams is 0.026 reported by Hoffmann et al. [28].

The oxidant preheating temperature is determined by the length of the thermoelectric region L_{TE}. The flame has a superadiabatic temperature and as compared to the premixed combustion, the flame position is determined by the fuel injection

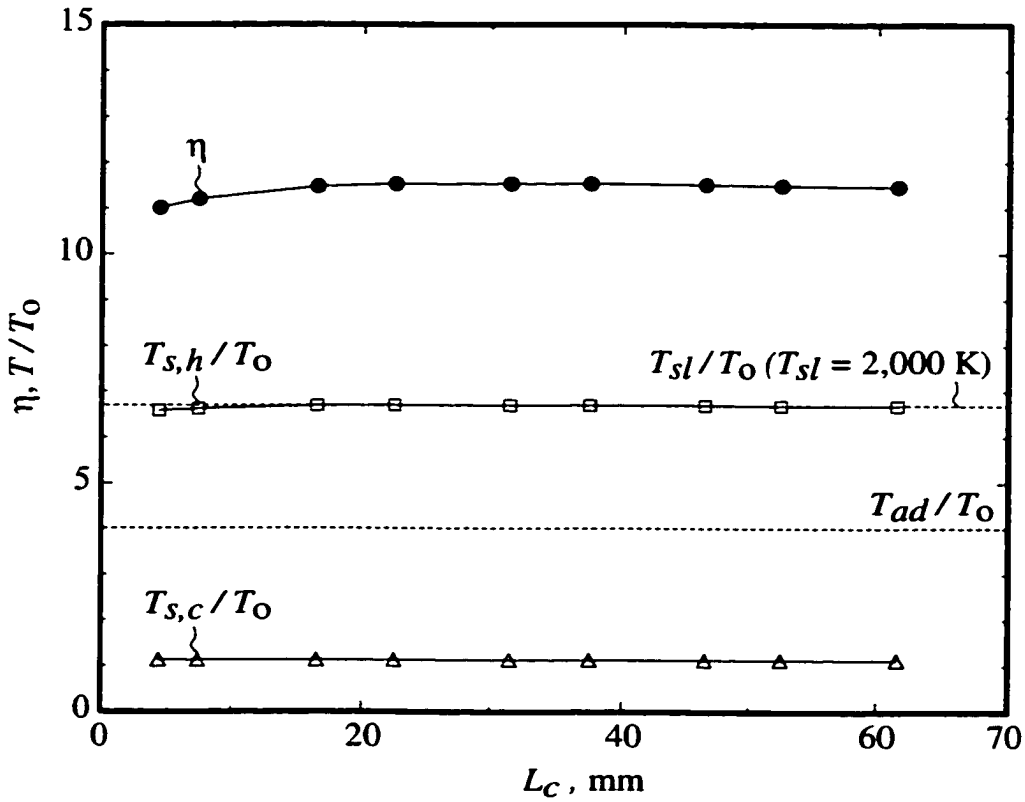

Figure 2.7: Effect of the combustion region length L_C on the conversion efficiency and the junction temperatures. $Z_e T_o = 0.59$, $R^*_{e,o} = 1$, $\tau_c = 10$ s, $\langle u \rangle_{g,o} = 0.75$ m/s, $D_1 = 1.3$ mm, $l_s = 0.6$ mm, $L_{TE} = 60$ mm, $C_{TE} = 1,908.8$, $C_C = 3,236.0$, $k^*_{TE} = 75$, $k^*_C = 523.6$, $\Phi = 0.414$.

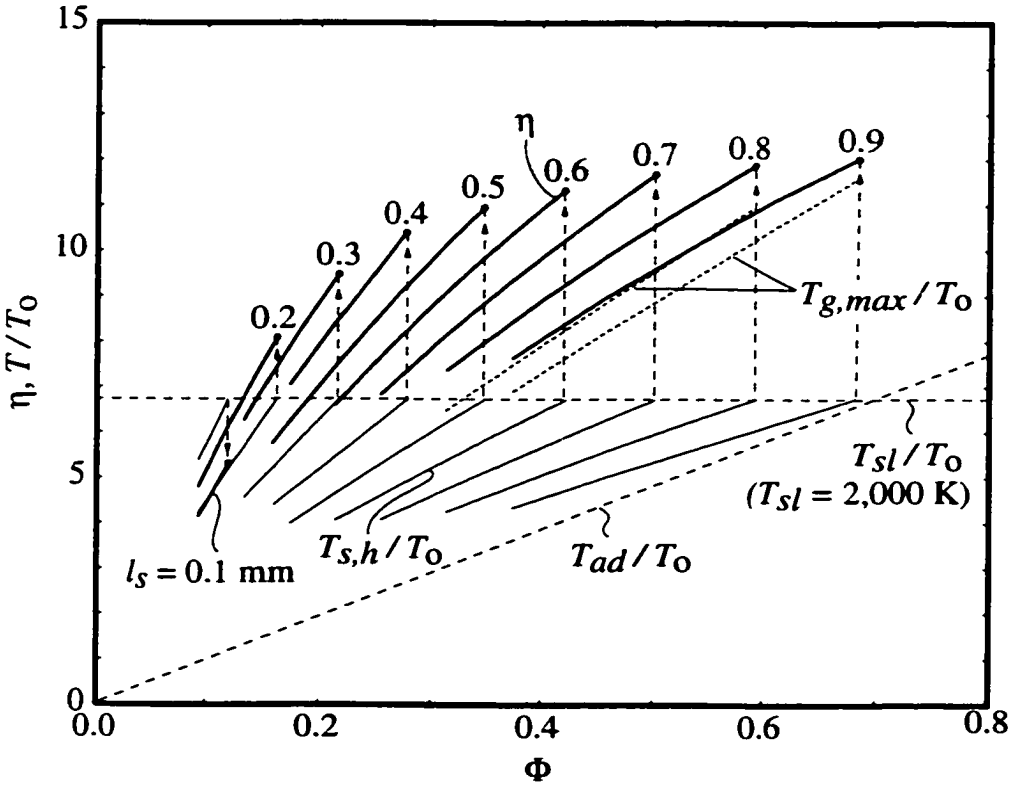

Figure 2.8: Effect of the stoichiometric ratio Φ on the conversion efficiency and the hot junction temperature, for various tube wall thicknesses. $Z_e T_o = 0.59$, $R^*_{e,o} = 1$, $\tau_c = 10$ s, $\langle u \rangle_{g,o} = 0.75$ m/s, $D_1 = 1.3$ mm, $L_{TE} = 60$ mm, $L_C = 7.5$ mm, $C_{TE} = 1,908.8$, $C_C = 3,236.0$, $k^*_{TE} = 75$, $k^*_C = 523.6$.

location, instead of the ignition temperature. In addition, with the fuel injection the maximum flame temperature is only limited by the allowable maximum temperature of the combustion region, i.e., its melting temperature. Then within the chemical kinetic considered, there is no limit on the achievable maximum flame temperature.

The efficiency increases with an increase in the length of the thermoelectric region, as shown in Figure 2.9. Here, $L_{TE} = 60$ mm is used to optimize the efficiency and keep $T_{s,h} \leq T_{sl} = 2,000$ K.

Improved surface convection between the gas and solid phase results in a higher temperature and higher efficiency. This requires large specific interfacial area [in the surface convection terms $Q_{g,ku}$ and $Q_{s,ku}$ of Eqs. (2.4) and (2.9) respectively] and large Nusselt number. The specific interfacial area $A_{sg}/V(= 4D_1/(2l_s + D_1)^2)$ have a maximum value at $D_{1,opt} = 2l_s$ for a fixed l_s. However, the optimum inside diameter for the maximum efficiency will be different from than $D_{1,opt}$, since the relative magnitude of the other terms in the energy conservation equations of Eqs. (2.14) and (2.19), dependent on D_1 and l_s. As shown in Figure 2.10, the maximum efficiency is achieved near $D_1 = 1.3$ mm, for $l_s = 0.6$ mm, which is close to the optimum diameter $D_{1,opt} = 1.2$ mm. The optimum diameter is also restricted by the allowable hot junction temperature being below the melting temperature T_{sl}.

As the tube thickness l_s decreases, the conduction heat loss decreases and thus the hot junction temperature increase. Keeping the hot junction temperature $T_{s,h} \leq T_{sl}, l_s = 0.6$ mm gives the highest efficiency, as shown Figure 2.11. If a higher melting temperature is allowed, the tube wall thickness smaller than 0.6 mm would give even higher efficiency. However, as the l_s is decreased beyond a threshold, the Joule heating becomes very significant and the efficiency begins to decrease.

Figure 2.12 shows the effect of the electrical resistance ratio on the conversion

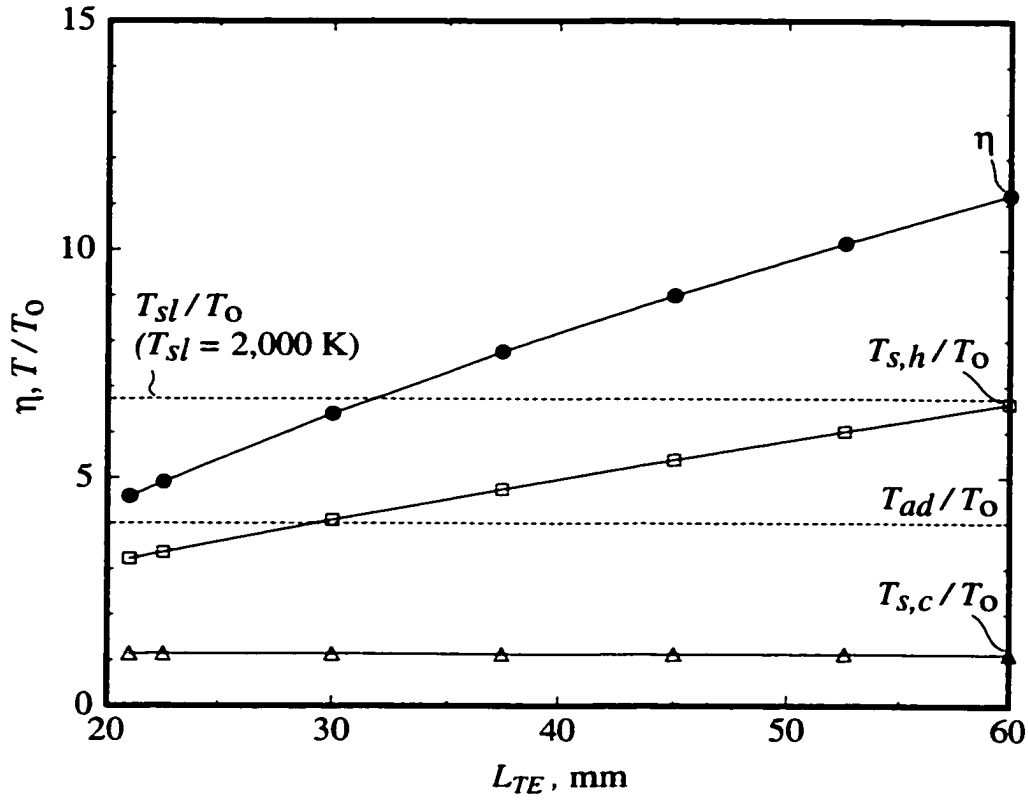

Figure 2.9: Effect of the thermoelectric region length L_{TE} on the conversion efficiency and the junction temperatures. $Z_eT_o = 0.59$, $R^*_{e,o} = 1$, $\tau_c = 10$ s, $\langle u \rangle_{g,o} = 0.75$ m/s $D_1 = 1.3$ mm, $l_s = 0.6$ mm, $L_C = 7.5$ mm, $C_{TE} = 1,908.8$, $C_C = 3,236.0$, $k^*_{TE} = 75$, $k^*_C = 523.6$, $\Phi = 0.414$.

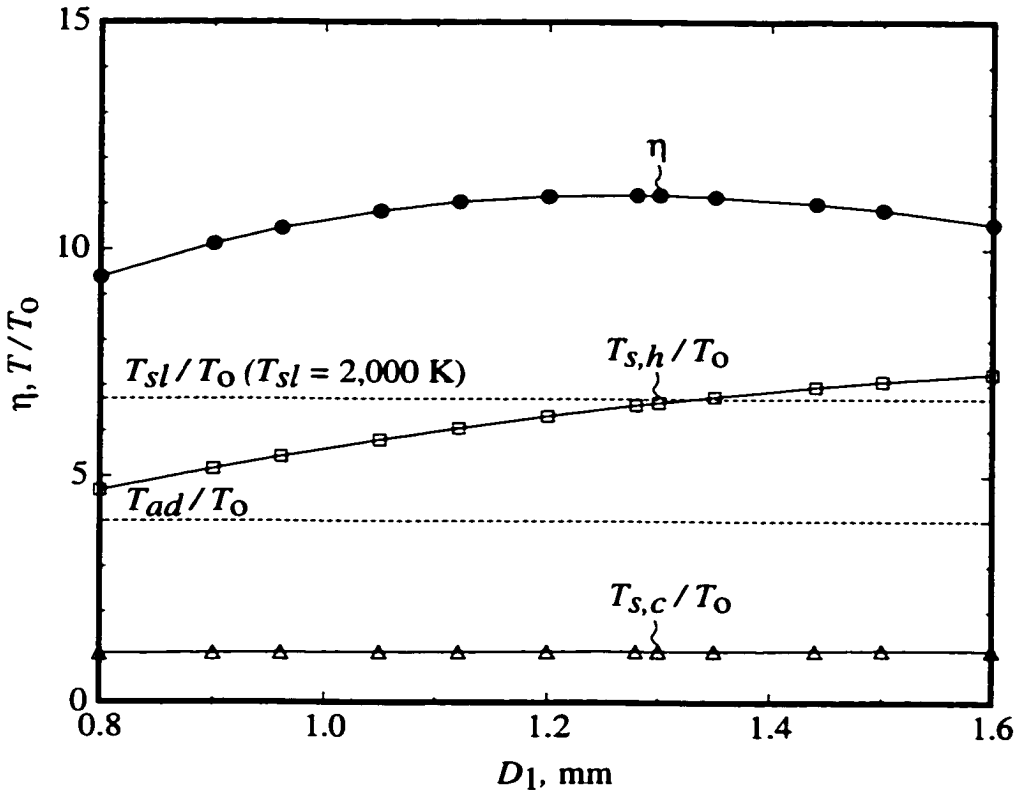

Figure 2.10: Effect of the diameter D_1 of the thermoelectric regions on the conversion efficiency and the junction temperatures. $Z_e T_o = 0.59$, $R^*_{e,o} = 1$, $\tau_c = 10$ s, $\langle u \rangle_{g,o} = 0.75$ m/s, $l_s = 0.6$ mm, $L_{TE} = 60$ mm, $L_C = 7.5$ mm, $C_{TE} = 1,908.8$, $C_C = 3,236.0$, $k^*_{TE} = 75$, $k^*_C = 523.6$, $\Phi = 0.414$.

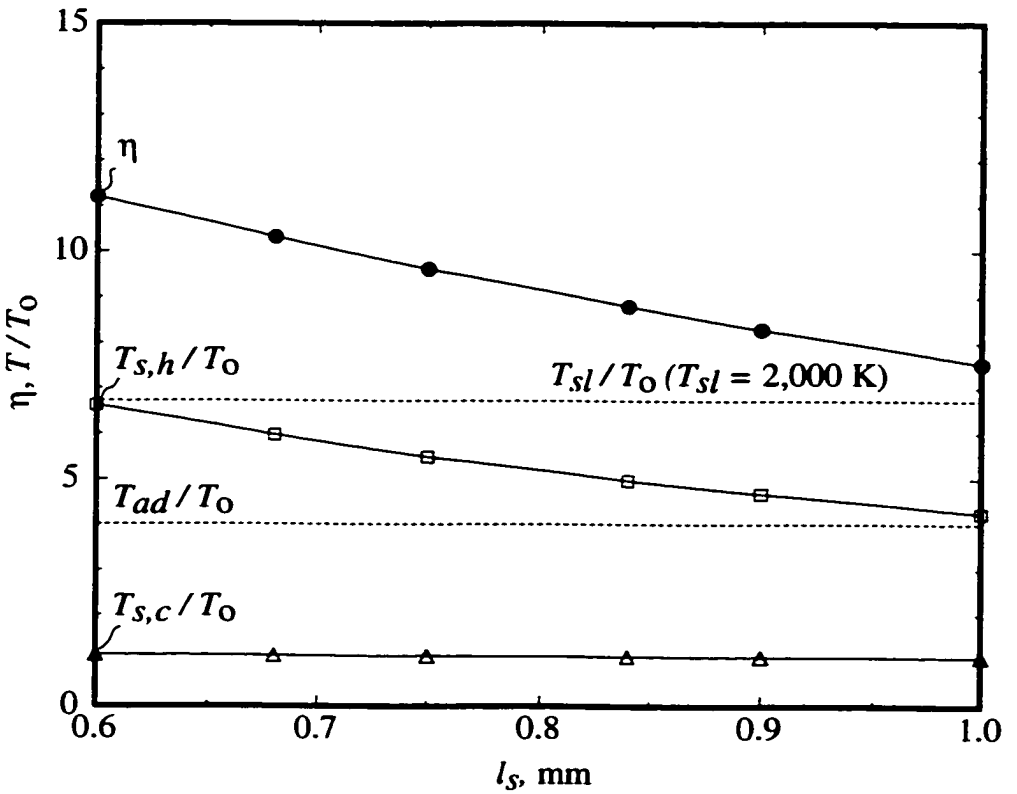

Figure 2.11: Effect of the tube thickness l_s on the conversion efficiency and the junction temperatures. $Z_eT_o = 0.59$, $R^*_{e,o} = 1$, $\tau_c = 10$ s, $\langle u \rangle_{g,o} = 0.75$ m/s, $D_1 = 1.3$ mm, $L_{TE} = 60$ mm, $L_C = 7.5$ mm, $C_{TE} = 1,908.8$, $C_C = 3,236.0$, $k^*_{TE} = 75$, $k^*_C = 523.6$, $\Phi = 0.414$.

efficiency. The efficiency does not increase noticeably for $R^*_{e,o} > 1.27$. For simplicity, $R^*_{e,o} = 1$ is used to optimize the efficiency. For the unity $R^*_{e,o}$, the total internal resistance $2N_tR_e$ is matched with the external resistance $R_{e,o}$. The power generated, and the current and voltage, are regulated by combining modules in parallel or series arrangements to meet the requirement.

In general, the surface radiation in the tube deteriorates the conversion efficiency by lowering the hot junction temperature. Here, the blackbody emissivity, $\epsilon_r = 1$, is used for the surface radiation within the tube. The tube length to diameter ratio is very large, and therefore, the radiation heat transfer is rather local.

2.3.2 Effect of Thermal Conductivity and Melting Temperature

Good thermoelectric materials should have a large Seebeck coefficient α_S, and low thermal conductivity k_{TE} to keep a large temperature difference. It should also have a low electrical resistance ρ_e to minimize the Joule heating. These properties are embodied in a figure-of-merit $Z_e = \alpha_S^2/(k_{TE}\rho_e)$. The thermal conductivity of the thermoelectric region is a key parameter in limiting the thermoelectric conversion efficiency. Figure 2.13 shows the effect of thermal conductivity of the thermoelectric region k_{TE} on the efficiency and the junction temperatures. The efficiency increases rapidly as the thermal conductivity decreases.

For lower thermal conductivity, (such as that of the low-temperature thermoelectric materials, e.g., bismuth telluride Bi_2Te_3, $k_{TE} = 1.6$ W/m-K, $k^*_{TE} = 28$), higher efficiencies are possible. Currently the high melting temperature material is used.

The asymptotic, quasi-steady, overall energy equation, neglecting radiation losses, gives

$$\eta = \frac{J_e^2 R_{e,o}/N_t}{Q_e + Q_{g,u} + J_e^2 R_{e,o}/N_t}. \tag{2.28}$$

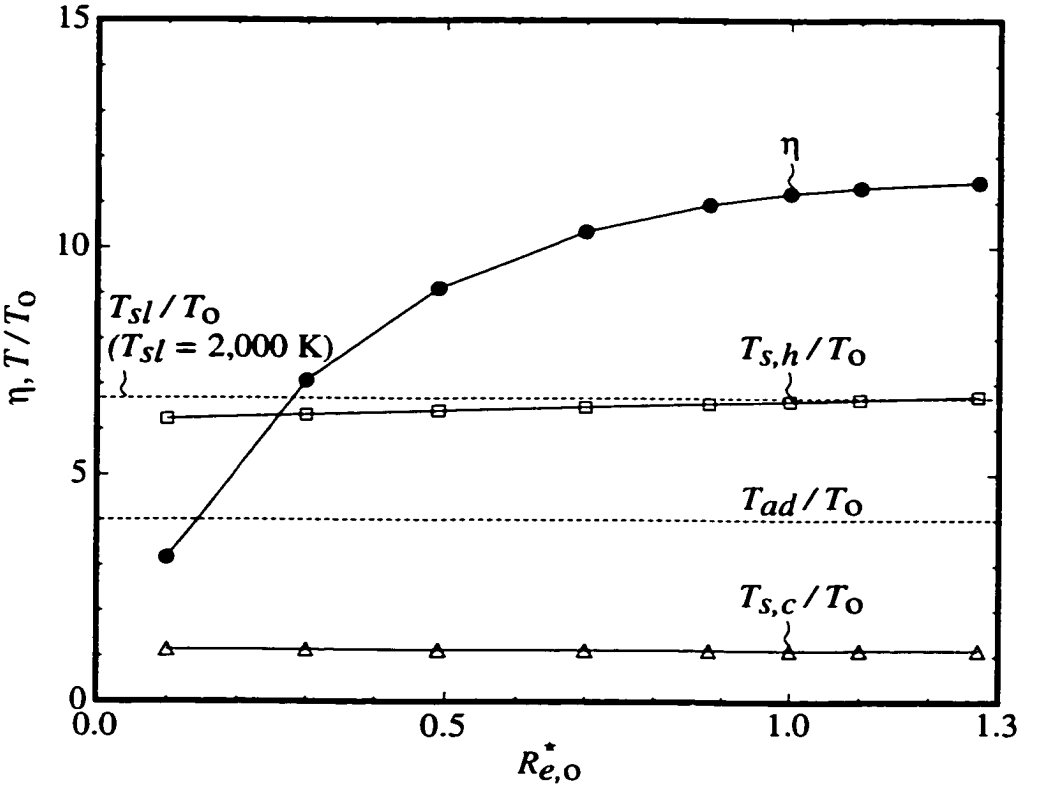

Figure 2.12: Effect of the dimensionless external resistance $R^*_{e,o}$ on the conversion efficiency and the junction temperatures. $Z_eT_o = 0.59$, $\tau_c = 10$ s, $\langle u \rangle_{g,o} = 0.75$ m/s, $D_1 = 1.3$ mm, $l_s = 0.6$ mm, $C_{TE} = 1,908.8$, $C_C = 3,236.0$, $L_{TE} = 60$ mm, $L_C = 7.5$ mm, $k^*_{TE} = 75$, $k^*_C = 523.6$, $\Phi = 0.414$.

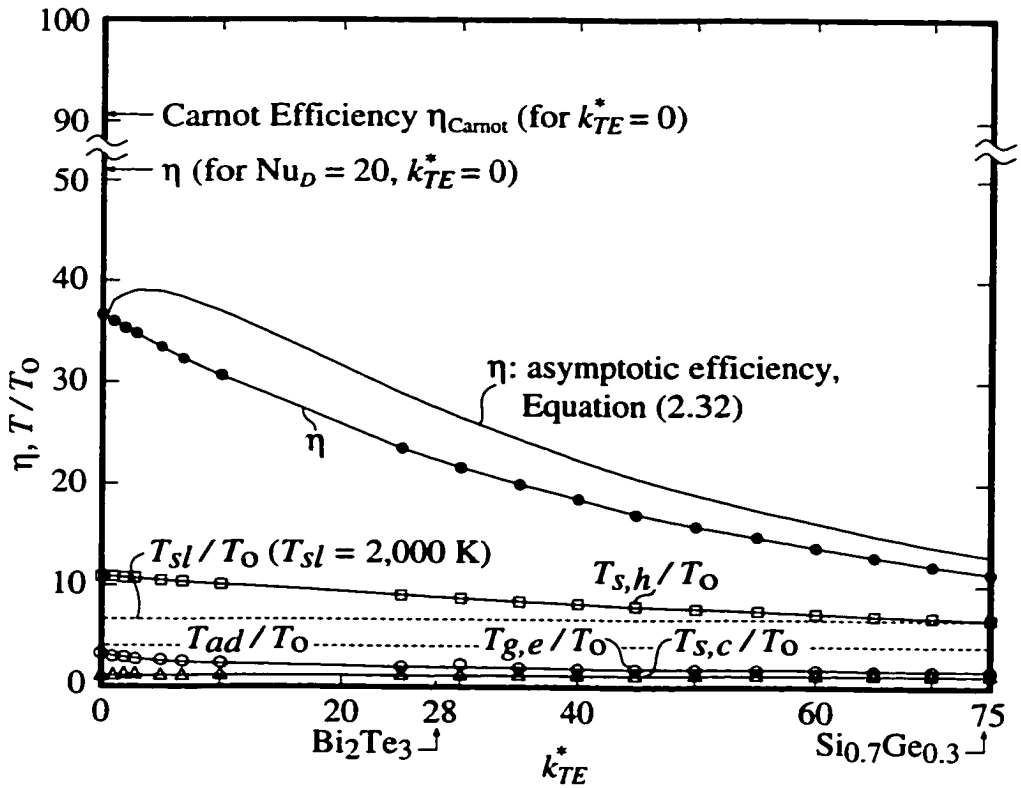

Figure 2.13: Effect of the thermal conductivity k_{TE} of the thermoelectric region on the conversion efficiency and the junction temperatures. $R^*_{e,o} = 1$, $\tau_c = 10$ s, $\langle u \rangle_{g,o} = 0.75$ m/s, $D_1 = 1.3$ mm, $l_s = 0.6$ mm, $C_{TE} = 1,908.8$, $C_C = 3,236.0$, $L_{TE} = 60$ mm, $L_C = 7.5$ mm, $k^*_C = 523.6$, $\Phi = 0.414$.

The neglected radiation losses to the ambient are less than 1 $\sim$ 3 percent of the combustion heating rate. This is because due to the high aspect ratio, the high temperature region of the tube is barely exposed to the ambient and the cold ends. Assuming a linear solid temperature distribution, the external heat removal rate at the cold junctions Q_e is approximated by the sum of the conduction loss and the cold-junction Peltier loss. Then from Eq. (2.26) we have

$$\begin{aligned} Q_e &= \mathrm{Nu}_e \frac{k_g}{D_2} A_s[(T_{s,1} - T_o) + (T_{s,n} - T_o)] \\ &= 2k_{TE} A_s \frac{\Delta T_s}{L_{TE}} + J_e \alpha_S (T_{s,1} + T_{s,n}). \end{aligned} \tag{2.29}$$

The exhaust gas heat loss $Q_{g,u}$ is

$$Q_{g,u} = (\rho c_p \langle u \rangle T)_{g,e} - (\rho c_p \langle u \rangle T)_{g,o}, \tag{2.30}$$

where $T_{g,e}$ is the exhaust gas temperature.

The power generated from a tube $J_e^2 R_{e,o}/N_t$ is, from Eq. (2.21)

$$J_e^2 R_{e,o}/N_t = \frac{\alpha_S^2 \Delta T_s^2 R_{e,o}^*}{2\rho_e L_{TE}(1 + R_{e,o}^*)^2} A_s. \tag{2.31}$$

Then, the efficiency given by Eq. (2.28), becomes

$$\begin{aligned} \eta^{-1} = 1 &+ \frac{1}{Z_e T_o} \frac{4(1 + R_{e,o}^*)}{R_{e,o}^*} \frac{T_o}{\Delta T_s} + \frac{1 + R_{e,o}^*}{R_{e,o}^*} \frac{T_{s,c}}{\Delta T_s} + \\ &\frac{2}{Z_e T_o} \frac{(1 + R_{e,o}^*)^2}{R_{e,o}^*} \frac{(\rho c_p \langle u \rangle T)_{g,e} - (\rho c_p \langle u \rangle T)_{g,o}}{k_{TE} \dfrac{\Delta T_s}{L_{TE}}} \frac{D_1^2}{D_2^2 - D_1^2} \frac{T_o}{\Delta T_s}. \end{aligned} \tag{2.32}$$

The prediction of Eq. (2.32) is also shown in Figure 2.13. The difference between Eq. (2.32) and the numerical results is mainly due to the underestimation of the conduction loss due to the convex, nonlinear solid temperature distribution. The convex solid temperature profile becomes more pronounced for the low thermal conductivity materials. In Eq. (2.32), the underestimation of the conduction loss leads

to an overestimation of the asymptotic efficiency. In Figure 2.13, as the thermal conductivity decreases, and therefore, the conduction loss decreases, the asymptotic efficiency becomes close to that obtained numerically. Figure 2.13 shows that due to the exhaust gas enthalpy loss, the maximum efficiency for zero thermal conductivity, $k^*_{TE} = 0$, is 37 percent, under the baseline conditions listed in Table 2.1. Note that the maximum efficiency is lower than the Carnot efficiency (due to the exhaust gas enthalpy, the Joule heating, and the cold-junction Peltier heating losses). Also note that for a larger Nusselt number, say $\mathrm{Nu}_D = 20$ (that is, for enhanced surface convection), resulting in a reduction in the exhaust gas enthalpy loss, the maximum efficiency increases substantially (but is still lower than the Carnot efficiency, due to the Joule and the cold-junction Peltier heating losses).

The solid conduction is always unfavorable for achieving a higher junction temperature difference and a higher conversion efficiency. This is in contrast to the unidirectional flow arrangement in which the solid conduction is the main mechanism for the heat recirculation for achieving a superadiabatic temperature (along with surface radiation).

Figure 2.14 shows that for a low thermal conductivity material, say $k^*_{TE} = 28$, a conversion efficiency over 25 percent is achievable, while $T_{s,h}$ is kept below $T_{sl} = 2,000$ K. Optimizations have shown that for this k^*_{TE} a smaller tube diameter, $D_1 = 0.63$ mm, is needed and the results shown in Figure 2.14, use this diameter. Note that using $k^*_{TE} = 28$, with $D_1 = 0.63$ mm and $\Phi = 0.53$, the electrical power generated is the same as that for $k^*_{TE} = 75, D_1 = 1.3$ mm and $\Phi = 0.414$. However, much less fuel is used. The smaller gas flow cross-sectional area results in a saving of 61 percent of the fuel. This is due to the smaller solid conduction loss.

The reduction in the effective thermal conductivity, potentially achievable us-

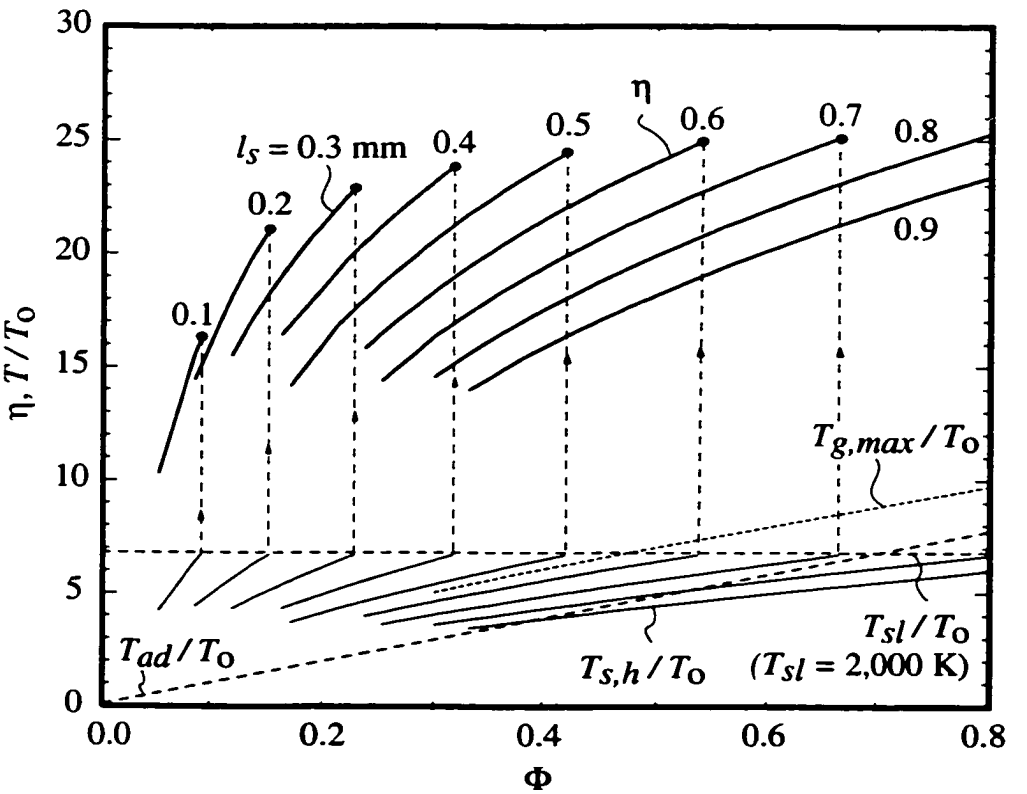

Figure 2.14: Effect of the stoichiometric ratio Φ on the conversion efficiency and the hot junction temperature, for various tube wall thicknesses for low thermal conductivity material (Bi_2Te_3). $Z_eT_o = 1.58$, $R^*_{e,o} = 1$, $\tau_c = 10$ s, $\langle u \rangle_{g,o} = 0.75$ m/s, $D_1 = 0.63$ mm, $L_{TE} = 60$ mm, $L_C = 7.5$ mm, $C_{TE} = 1,908.8$, $C_C = 3,236.0$, $k^*_{TE} = 28$, $k^*_C = 523.6$.

ing small powders (small grain size), should lead to a high efficiency thermoelectric converter. Experimental verification of the high efficiency thermoelectric power generator is needed.

2.4 Summary

The proposed combustion-thermoelectric tube allows for exploiting of the local superadiabatic temperature to improve the combustion-thermoelectric energy conversion efficiency. Direct fuel injection is effective of controlling the flame position and for increasing the flame and the hot junction temperatures. For the current high-temperature $Si_{0.7}Ge_{0.3}$ thermoelectric alloy, a conversion efficiency of 11.3 percent is predicted.

For a thermal conductivity equal to that of bismuth telluride Bi_2Te_3, and a melting temperature of 2,000 K, a conversion efficiency of about 25 percent is predicted.

CHAPTER III

REGENERATIVE DIESEL ENGINE

3.1 Motivation, Background, Scope, and Objectives

In power generation systems, thermal regeneration (which is one of the heat recovery methods using the exhaust heat content), is a well-known concept for increasing the thermal efficiency. Whereas thermal regeneration has been widely used in open cycle systems (such as gas turbine engines) in the past, because of easy applicability, thermal regeneration in closed cycle systems (such as the internal combustion engines) cannot be easily accommodated due to the nature of the engine cycle. Whereas in internal combustion engines, thermal regeneration using turbocompounding has been used, heating and compressing the intake air (before completing air intake) does not take full advantage of heat recovery. In contrast if the thermal regeneration is completed inside the cylinder after intake (in order not to affect the volume efficiency) the thermal efficiency will increase.

In order to realize such an efficient thermal regeneration process, a thermal storage medium is needed to save the heat of the exhaust gas and to heat the intake gas. The regenerative Diesel engine invented by the Ferrenberg [22], uses an in-cylinder, reciprocating, porous regenerator and is the first realization of effective thermal regeneration. The Stirling engine has the same configuration by using two

gas chambers connected by a porous regenerator, but the cycle sequence is different.

The regenerative engine is shown in Figure 3.1. The porous insert is attached to a rod and moves within the cylinder, synchronized, but out of phase with the piston. During the regenerative heating stroke, the regenerator moves toward the piston and during the regenerative cooling stroke, the regenerator moves away from the piston. Following combustion and expansion, the products of combustion (the exhaust gases) retain an appreciable sensible heat. During the regenerative cooling stroke, the hot exhaust gas flows through the regenerator and stores part of this sensible heat by surface-convection heat transfer within the regenerator (which has a large surface area). Since the cold air flows through the insert and is heated after the intake is closed (during the regenerative heating stroke), the volumetric efficiency is not affected.

To explore the feasibility and limitations of the regenerative Diesel engine, an existing in-cylinder thermal regeneration concept for Diesel engines is examined, considering various porous insert motions and fuel injection strategies on the fuel evaporation and combustion and engine efficiency. The results are compared with the results of a conventional Diesel engine. A parametric study considering various compression ratios and regenerative heating/cooling strokes of the regenerator is done to find optimum performance.

3.2 Analysis

The geometric parameters and variables of the regenerative Diesel engine with a side valve position are shown Figure 3.2. The two gas zones of the top and bottom chambers are connected by the permeable regenerator. The regenerator is divided into N_r small volumes and each volume consists of the gas and solid phases. The

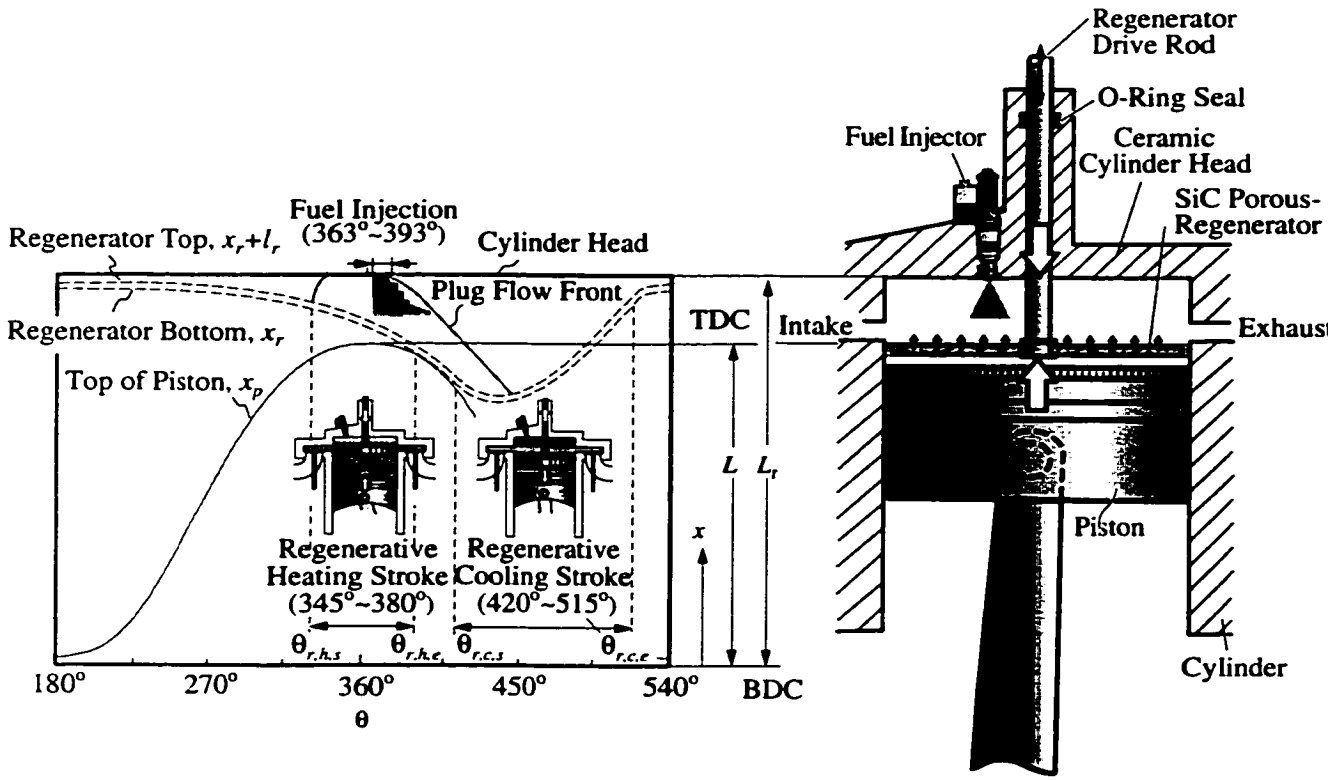

Figure 3.1: Sequence of motion of the regenerator and piston and physical rendering of fuel injection and air blowing during the regenerative heating stroke.

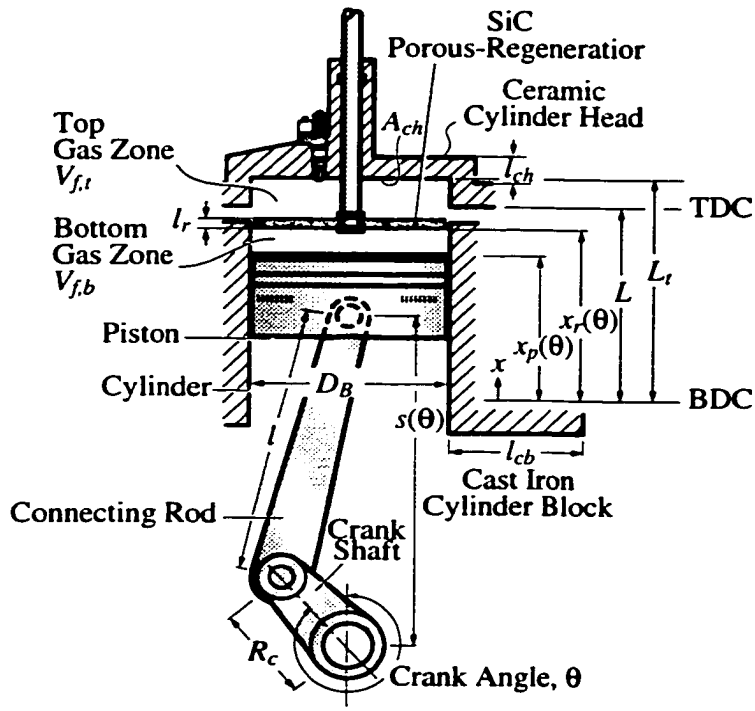

Figure 3.2: Geometric parameters and variables of the regenerative Diesel engine.

multi-zone-first-order analysis of the regenerative engine performance is given below, followed by the analysis of the injected fuel droplet.

3.2.1 Heat Transfer

A multi-zone gas model and a one-dimensional model for the solid phases are used for the analysis of the regenerative Diesel engine (Kaviany, [31]). The heat flux vector tracking for the regenerative engine is shown in Figure 3.3. The mechanisms of the heat transfer considered include the surface-convection, conduction and surface/volume radiation. The prescribed temperature of the cooling water is used for the analysis of the conduction heat transfer through the cylinder walls. One-dimensional energy conservation equations with both uniform and nonuniform grids are used for solid phases of the regenerator, the piston, the cylinder head, and cylinder block. Since the fuel is injected into the top gas zone and the fuel vapor does

not escape to the bottom gas zone under the conditions considered, it is assumed that the combustion occurs only in top gas zone. The heat release rate in the top gas zone is determined using a single-step, second-order combustion model and the empirical relation of the ignition delay. The species concentrations are calculated to determine the heat release rate and the NO_X production rate.

The gas is assumed as an ideal gas

$$\rho_f = \frac{M_f}{V_f} = \frac{p_f}{\frac{R_g}{M_a} T_f}. \tag{3.1}$$

For the top gas zone above the regenerator, the energy conservation equation is given as

$$Q_{u,inj} - (Q_{u,r})_{N_r} + \langle Q_{ku,t\text{-}ch} \rangle_{D_B} + \langle Q_{ku,t\text{-}cb} \rangle_{D_B} + \langle Q_{ku,t\text{-}r} \rangle_{D_B} = -\frac{d}{dt}(M_{f,t} c_{p,f} T_{f,t}) + \dot{S}_t, \tag{3.2}$$

where $Q_{u,inj}$ is the heat transfer due to the fuel injection and $(Q_{u,r})_{N_r}$ is the heat transfer due to the gas influx through the regenerator. $\langle Q_{ku,t\text{-}ch}$ or $_{cb}$ or $_{r} \rangle_{D_B}$ are the surface-convection heat transfer between the top fluid and surfaces (of the cylinder head, the cylinder block and the regenerator). The energy conversion in the top gas zone $\dot{S}_t$ is due to combustion (occurs only in the top gas zone) $\dot{S}_{r,c}$, gas expansion cooling/compression heating $\dot{S}_{m,p,t}$, fuel evaporation $\dot{S}_{F,lg}$, and radiation $(\dot{S}_{e,\epsilon} + \dot{S}_{e,\alpha})_t$, i.e.,

$$\dot{S}_t = \dot{S}_{r,c} + \dot{S}_{m,p,t} + \dot{S}_{F,lg} + (\dot{S}_{e,\epsilon} + \dot{S}_{e,\alpha})_t \tag{3.3}$$

More detailed description, for each term of the energy conservation Eg. (3.2), is given in the Appendix.

Similarly, for the bottom gas zone, the energy conservation equation is given as

$$-Q_{u,int} + Q_{u,exh} + (Q_{u,r})_0 + \langle Q_{ku,b\text{-}cb} \rangle_{D_B} + \langle Q_{ku,b\text{-}p} \rangle_{D_B} +$$

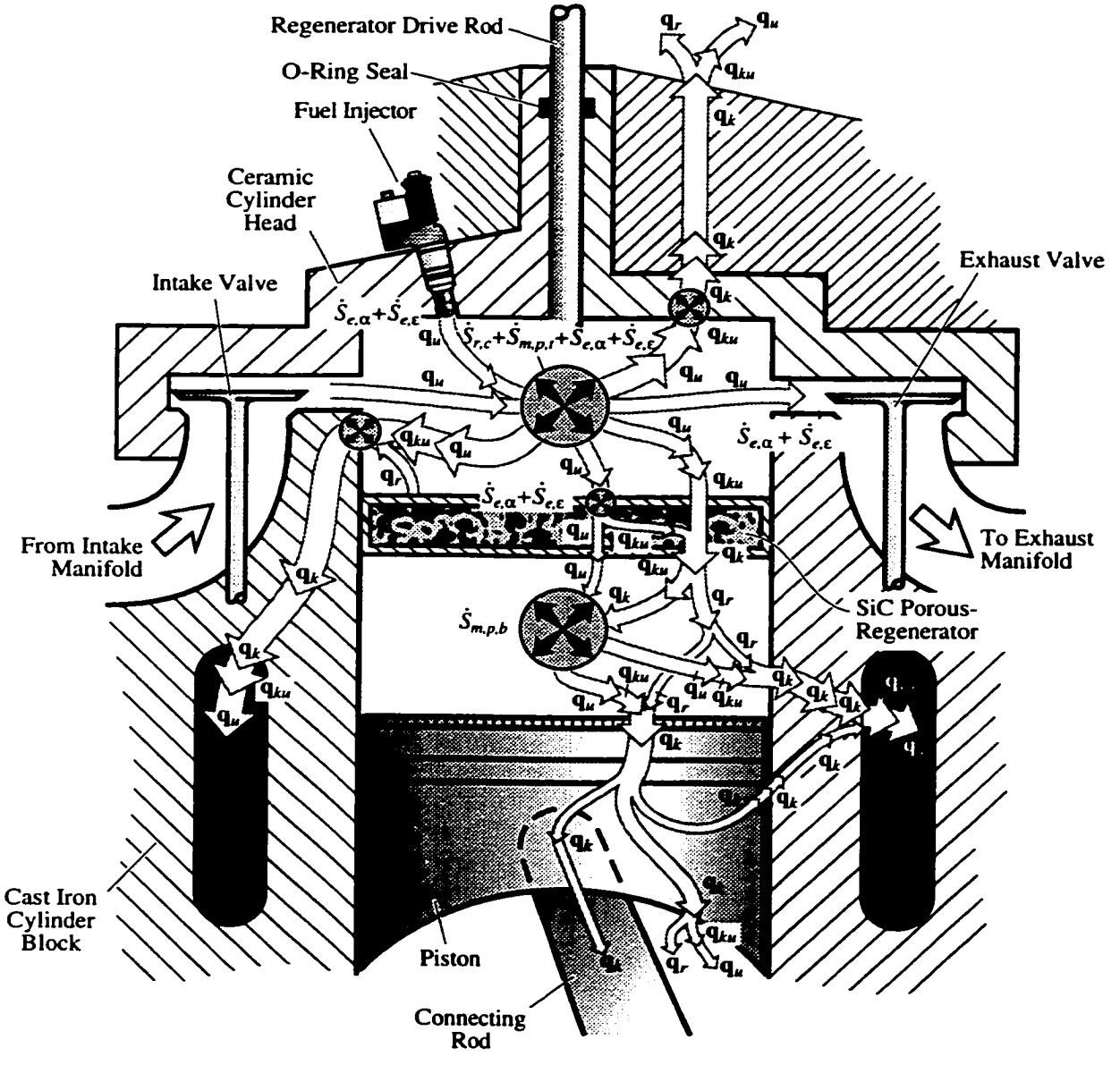

Figure 3.3: Heat flux vector tracking for the regenerative Diesel engine.

$$\langle Q_{ku,b\text{-}r}\rangle_{D_B} = -\frac{d}{dt}(M_{f,b}c_{p,f}T_{f,b}) + \dot{S}_b, \tag{3.4}$$

where $Q_{u,int}$, $Q_{u,exh}$ and $(Q_{u,r})_0$ are the convection heat transfer due to the intake, the exhaust, and the gas influx through the regenerator. The energy conversion in the bottom gas zone $\dot{S}_b$ is due to gas expansion cooling/compression heating only, i.e.,

$$\dot{S}_b = \dot{S}_{m,p,b} = V_{f,b}\frac{dp_{f,b}}{dt}. \tag{3.5}$$

More detailed description, for each term of the energy conservation Eq. (3.4), is given in the Appendix.

The porous regenerator is divided into N_r small volumes with uniform thickness $\Delta l_{r,i}$ and local thermal nonequilibrium is assumed between the gas and the solid phases. Energy equation for each volume of the solid phase is given by

$$\begin{aligned} &-(Q_{k,r})_{(i-1)\text{-}i} + (Q_{k,r})_{i\text{-}(i+1)} + \langle Q_{ku,f\text{-}r}\rangle_i - Q_{d,i} \\ &= -\rho_r \Delta l_{r,i}(1-\epsilon_r)A_r c_{p,r}\frac{dT_{r,i}}{dt}, \quad i = 1, 2, \ldots, N_r, \end{aligned} \tag{3.6}$$

where $(Q_{k,r})_{i\text{-}(i+1)}$, $\langle Q_{ku,f\text{-}r}\rangle_i$ and $Q_{d,i}$ are the heat transfer due to the conduction in the solid phase, the surface-convection and the evaporation of the fuel droplet respectively. Note that it is assumed that the heat transfer due to the evaporation of the fuel droplet occurs in the solid phase of the regenerator. More detailed description, for each term of the energy conservation Eq. (3.6), is given in the Appendix.

The energy equation for the gas phase in the porous regenerator is given as

$$\begin{aligned} &-(Q_{u,r})_{i-1} + (Q_{u,r})_i - \langle Q_{ku,f\text{-}r}\rangle_i \\ &= -\frac{d}{dt}(M_{f,r}c_{p,f}T_{f,r})_i + \dot{S}_{r,i}, \quad i = 1, 2, \ldots, N_r, \end{aligned} \tag{3.7}$$

where

$$\dot{S}_{r,i} = (\dot{S}_{m,p})_{r,i} = V_{f,r,i}\frac{dp_{f,r,i}}{dt}.$$

and the convection heat transfer $(Q_{u,r})_i$ and the surface-convection heat transfer $\langle Q_{ku,f-r}\rangle_i$ are given in Appendix in detail. The energy conservation equations at the top and bottom surfaces of the regenerator are also given in the Appendix.

The cylinder wall of the regenerative Diesel engine consists of the ceramic cylinder head and the cast iron cylinder block which are separated from each other. The cylinder head made of ceramic is used as a thermal barrier to reduce the heat loss. The cylinder head is divided into $N_{ch} - 1$ small volumes with a uniform thickness $\Delta l_{ch,i} = l_{ch,1}/(N_{ch}-1)$ and a large volume with thickness $\Delta l_{ch,N_{ch}} = l_{ch,2} = l_{ch} - l_{ch,1}$. Then the energy equation for the solid phase is written as

$$(Q|_{A,ch})_i = -\rho_{ch}\Delta l_{ch,i} A_{k,ch} c_{p,ch} \frac{dT_{ch,i}}{dt}, \quad i = 1, 2, \ldots, N_{ch}, \tag{3.8}$$

where $(Q|_{A,ch})_i$ is heat transfer due to the conduction and is given in Appendix in detail. The energy conservation equations at the surface inside the cylinder head are also given in the Appendix.

The energy conservation equations for the cylinder block and the piston are given similarly.

The intake mass flow rate using the valve curtain area $A_{v,i}$, is given as

$$\dot{M}_{f,int} = N_{v,i} C_{D,i} A_{v,i} \frac{p_o}{(\frac{R_g}{M_g} T_o)^{1/2}} f_{A,f}(p_T, p_o), \tag{3.9}$$

where

$$A_{v,i} = \pi D_{v,i} L_{v,i} f_{A,v}(\theta, \theta_{v,s,i}, \theta_{v,e,i}).$$

Similarly, the exhaust mass flow rate $\dot{M}_{f,exh}$ is determined. Here $f_{A,f}(p_T, p_o)$ is obtained from a one-dimensional isentropic flow analysis for the compressible flow through a flow restriction (Heywood, [27]).

The mass flow through the porous regenerator is determined by the Darcy law (Kaviany, [30]) and is given by

$$(\dot{M}_{f,r})_i = A_r \rho_{f,r} \frac{K_r}{\mu_f} \frac{p_{f,r,i} - p_{f,r,i+1}}{\Delta l_{r,i}}, \quad K_r = \frac{\epsilon_r^3 D_p^2}{180(1-\epsilon_r)^2},$$
$$i = 0, 1, \ldots, N_r, \tag{3.10}$$

where

$$\rho_{f,r} = \begin{cases} \rho_{f,r,i} & \text{for } (\dot{M}_{f,r})_i \geq 0 \text{ (the bottom to the top gas zone)} \\ \rho_{f,r,i+1} & \text{for } (\dot{M}_{f,r})_i < 0, \end{cases}$$

and $\rho_{f,r,0} = \rho_{f,b}$, and $\rho_{f,r,N_r+1} = \rho_{f,t}$.

The combustion reaction $\dot{M}_{r,F}$ in the top gas zone, using the single-step reaction model (Westbrook and Dryer, [36]), is given by

$$\dot{M}_{r,F} = \rho_{f,t} a_r \rho_F^{a_F} \rho_O^{a_O} \exp^{\frac{\Delta E_a}{R_g T_{f,t}}}, \tag{3.11}$$

where a_r is the pre-exponential factor and ΔE_a is the activation energy (kJ/kmole-K). The ignition delay is determined using the empirical correlation of the Diesel engine and ranges $2 \sim 3$ crank angles under the conditions considered (Heywood, [27]).

3.2.2 Droplet Evaporation

The transient fuel evaporation and the fuel droplet fate are determined using a Lagrangian, droplet tracking model along with a porous-surface filtration submodel for the droplet-regenerator interaction. These allow for the analysis of the fuel droplet evaporation, accumulation and combustion. After the fuel is injected, the fuel spray is assumed to be divided into N_d homogeneous droplet parcels. It is assumed that each parcel has n_d droplet particles with the same properties (e.g., droplet diameter,

speed and temperature) and does not interfere with other droplet parcels. The Sauter mean diameter D_{SM} is used as the initial droplet diameter (Hiroyasu and Kadota, [29]).

The instantaneous location of a droplet is given by

$$\frac{d}{dt}\mathbf{x}_d = \mathbf{u}_d. \tag{3.12}$$

The instantaneous velocity is determined by the momentum equation of a droplet as

$$\frac{d}{dt}(M\mathbf{u})_d = \sum \mathbf{F} = \mathbf{F}_d + \mathbf{F}_{\Delta T} + ..., \tag{3.13}$$

and neglecting the thermophoresis force $\mathbf{F}_{\Delta T}$ and other forces, the momentum equation is given by

$$M_d \frac{d\mathbf{u}_d}{dt} = -\frac{\pi}{8} D_d^2 \rho_{f,t} C_D |\mathbf{u}_d - \langle \mathbf{u}_f \rangle_{p,t}| (\mathbf{u}_d - \langle \mathbf{u}_f \rangle_{p,t}), \tag{3.14}$$

where

$$C_D = \begin{cases} 27\mathrm{Re}_D{}^{-0.84} & \text{for } \mathrm{Re}_D < 80 \\ 0.271\mathrm{Re}_D{}^{0.217} & \text{for } 80 < \mathrm{Re}_D < 10^4, \end{cases}$$

where $\mathrm{Re}_D = \rho_{f,t} D_d |\mathbf{u}_d - \langle \mathbf{u}_f \rangle_{p,t}| / \mu_f$.

In order to account for the deflection of the fuel droplets by the air flow emanating from the regenerator, the gas flow in the top gas zone is assumed to be the plug flow and the gas velocity is given as

$$\langle u_f \rangle_{p,t} = \frac{(\dot{M}_{f,r})_{N_r}}{A_r \rho_{f,r}} + \frac{dx_r}{dt}. \tag{3.15}$$

From the uniform temperature model for the fuel droplet heat and mass transfer (only the composition of the bulk liquid remains at the injected condition while the surface composition varies as required by the local conditions. The temperature of

the surface and the bulk liquid are the same and are known at each instant), the mass conservation for a droplet is given by (Faeth, [21])

$$\frac{dM_d}{dt} = -\dot{M}_d. \tag{3.16}$$

The corrected evaporation rate $\dot{M}_d$ for the convective ambient is expressed

$$\frac{\dot{M}_d}{\dot{M}_d(\mathrm{Re}_D = 0)} = 1 + f(\mathrm{Re}_D,\mathrm{Sc}), \tag{3.17}$$

where the evaporation rate $\dot{M}_d(\mathrm{Re}_D = 0)$ in the quiescent ambient is given in the Appendix and

$$f(\mathrm{Re}_D,\mathrm{Sc}) = \frac{0.278\mathrm{Re}_D{}^{1/2}\mathrm{Sc}^{1/3}}{[1 + 1.232/\mathrm{Re}_D\mathrm{Sc}^{4/3}]^{1/2}}. \tag{3.18}$$

The droplet energy conservation equation based on the uniform temperature model is

$$+\frac{\mathrm{Nu}_{D,1}k_f}{D_d}A_d(T_d - T_{f,t}) + \frac{\mathrm{Nu}_{D,2}k_f}{D_d}A_d(T_d - T_{r,i}) = -M_d c_{p,F}\frac{dT_d}{dt} - \dot{M}_d\Delta h_{lg}, \tag{3.19}$$

where $\mathrm{Nu}_{D,1}$ is due to single-phase (droplets in the gas) and $\mathrm{Nu}_{D,2}$ is due to phase change (film boiling) and surface convection (when the droplets are impinging on the regenerator) and the fuel droplet temperature T_d and $T_{r,i}$ is the temperature of the porous regenerator in contact with the droplets. The Nusselt number $\mathrm{Nu}_{D,2}$ is given in the Appendix (Bernardin and Mudawar, 1997) in detail.

The corrected Nusselt number $\mathrm{Nu}_{D,1}$ in the convective ambient is expressed

$$\frac{\mathrm{Nu}_{D,1}}{\mathrm{Nu}_{D,1}(\mathrm{Re}_D = 0)} = 1 + f(\mathrm{Re}_D,\mathrm{Pr}), \tag{3.20}$$

where $f(\mathrm{Re}_D,\mathrm{Pr})$ is the same as that given in Eq. (3.18), except Sc is replaced with Pr. The Nusselt number $\mathrm{Nu}_{D,1}(\mathrm{Re}_D = 0)$ in the quiescent ambient. For droplets

colliding with the regenerator, the filtration efficiency is expressed as (Martynenko et al., 1988)

$$\alpha = \alpha_d[\frac{6(1-\epsilon_r)}{\pi}]^{1/3}, \quad \alpha_d = 0.093 + 0.387\text{Sto} - 0.054\text{Sto}^2, \tag{3.21}$$

where

$$\text{Sto} = \frac{\rho_{b,l} D_d^2 |\mathbf{u}_d - \frac{d\mathbf{x}_r}{dt}|}{18\mu_f(d_s/2)},$$

where d_s is the particle diameter of porous regenerator and $\mathbf{u}_d$ is a droplet velocity.

Finally, the mass conservation equations for the gas phase, in the top and bottom gas zones, are given by

$$-(\dot{M}_{f,r})_{N_r} - \dot{M}_{F,evp} = -\frac{dM_{f,t}}{dt} \tag{3.22}$$

$$-\dot{M}_{f,int} + (\dot{M}_{f,r})_0 + \dot{M}_{f,exh} = -\frac{dM_{f,b}}{dt}, \tag{3.23}$$

where $\dot{M}_{F,evp} = \sum_i^{N_d}(n_d\dot{M}_d)_i$.

The mass conservation equation for the gas phase, inside the regenerator, is given by

$$-(\dot{M}_{f,r})_{i-1} + (\dot{M}_{f,r})_i = -\frac{dM_{f,i}}{dt}, \quad i = 1, 2, \ldots, N_r. \tag{3.24}$$

3.2.3 Regenerator Motion

The motion sequences of the piston and the bottom surface of the regenerator are given by

$$x_p = L_t - \frac{V_c}{A_{ch}}\{1 + 0.5(r_c - 1)[1 - \cos(\frac{\pi\theta}{180})]\}, \tag{3.25}$$

$$x_r = a + b\theta + c\theta^2 + d\theta^3 + e\theta^4 + f\theta^5, \tag{3.26}$$

where the constants a, b, c, d, e, and f are determined to satisfy the smooth transition of the velocity and the acceleration of the regenerator. Also, the minimum gaps,

between the top surface of the regenerator and the cylinder head and between the bottom surface of the regenerator and the piston are needed due to the required tolerance.

The net indicated work per cycle $W_{c,in}$ is given by

$$W_{c,in} = \int \dot{W}_{c,in} dt = \int \left[\oint (p_{f,t} \frac{dV_{f,t}}{dt} + p_{f,b} \frac{dV_{f,b}}{dt}) \right] dt. \tag{3.27}$$

The mechanical loss, due to the pressure drop $\Delta p = p_{f,t} - p_{f,b}$ across the porous regenerator, is expressed by

$$\dot{W}_{loss} = \dot{W}_{c,in} + \oint p_{f,t} A_{ch} \frac{dx_p}{dt} = - \oint \Delta p A_{ch} (\frac{dx_r}{dt} - \frac{dx_p}{dt}). \tag{3.28}$$

The relevant indicators of the engine performance are the thermal efficiency η_T, the volumetric efficiency η_V, the net indicated mean-effective pressure $p_{mep,in}$, the indicated specific fuel consumption sfc, and the fuel conversion efficiency η_F. The thermal efficiency η_T is defined as

$$\eta_T = \frac{W_{c,in}}{-M_{r,F} \Delta h_{r,F}}, \quad M_{r,F} = \int_{t_{F,s}}^{t_{F,e}} \dot{M}_{r,F} dt. \tag{3.29}$$

The volumetric efficiency η_V is

$$\eta_V = \frac{M_a(\theta_{v,e,i})}{M_{a,o}}, \tag{3.30}$$

where $M_a(\theta_{v,e,i})$ is the amount of mass of air in the cylinder when the intake valve closes and $M_{a,o}$ is the amount of air in the cylinder when charged under the inlet conditions of the intake valve.

The net indicated mean-effective pressure $p_{mep,in}$, the specific fuel consumption sfc and the fuel conversion efficiency η_F are given by

$$p_{mep,in} = \frac{W_{c,in}}{V_d}, \quad sfc = \frac{M_{F,o}}{W_{c,in}} \quad \eta_F = \frac{sfc}{\Delta h_{r,F}}. \tag{3.31}$$

The energy and species conservation equations are solved with an IMSL solver (DIVPAG) capable of solving the stiff ordinary differential equations. The quasi-steady state (time periodic) solution is found when the overall energy balance error is less than $2 \sim 3$ percent. The parameters used for the numerical simulation are listed in Table 3.1 and the operational characteristics are listed in Table 3.2.

Table 3.1: Characteristic dimensions of the engine and porous regenerator and properties for the fluids.

Parameter	Magnitude	Parameter	Magnitude
cylinder:		fuel:	
D_B	0.125 m	M_F	142.3 kg/kmole
L	0.14 m	Δh_{lg}	116×10^3 J/kg-fuel
cylinder head:		$\rho_{b,l}$	853 kg/m^3
ρ_{ch}	5,200 kg/m^3	$c_{p,F}$	3,010 J/kg-K
$c_{p,ch}$	730 J/kg-K	$k_{F,v}$	54×10^{-3} W/m-K
k_{ch}	1.2 W/m-K	$\epsilon_{r,F}$	0.75
l_{ch}	2 cm	$D_{m,F}$	6×10^{-6} m^2/s
cylinder block:		T_c	617.6 K
ρ_{cb}	7,200 kg/m^3	p_c	2.096 MPa
$c_{p,cb}$	480 J/kg-K	reaction:	
k_{cb}	54 W/m-K	$\Delta h_{r,F}$	-42.5×10^6 J/kg-fuel
l_{cb}	2 cm	a_r	5.4×10^8
piston:		a_F	0.25
ρ_p	2,750 kg/m^3	a_O	1.0
$c_{p,p}$	915 J/kg-K	ΔE_a	1.256×10^8 J/kmole-K
k_p	155 W/m-K	NO formation:	
l_p	2 cm	a_r	5.74×10^{14} (cm^3/mol)$^{\frac{1}{2}}$/s
$\alpha_{r,ch/cb/p}$	0.7/0.5/0.5	ΔE_a	5.562×10^8 J/kmole-K
$\epsilon_{r,ch/cb/p}$	0.7/0.5/0.5	air:	
regenerator:		M_a	28.96 kg/kmole
ρ_r	200 kg/m^3	γ	1.4
$c_{p,r}$	1,300 J/kg-K	$c_{p,a}$	1,300 J/kg-K
k_r	63 W/m-K	gas mixture:	
$\alpha_{r,r}$	0.9	M_g	28.6 kg/kmole
$\epsilon_{r,r}$	0.9	$c_{p,f}$	1,600 J/kg-K
l_r	8 mm	k_f	0.0824 W/m-K
ϵ_r	0.7	μ_f	52.1×10^{-6} Pa-s
A_{sf}/V	11,602 m^2/m^3	Pr	1.0
d_s	150 μm	Sc	1.0
D_p	50 μm	$\alpha_{r,f}$	0.1
T_{sl}	2,700 K	$\epsilon_{r,f}$	0.1
$T_{r,max}$	1,600 K		

Table 3.2: Operational characteristics of the engine.

Parameter	Magnitude	Parameter	Magnitude
operating conditions:		intake valve:	
		$N_{v,i}$	1
r_c	$8 \sim 16.5$	$C_{D,i}$	0.75
N	1,600 rpm	$D_{v,i}$	0.044 m
$(A/F)_a$	30	$L_{v,i}$	$0.25D_{v,i}$
$(A/F)_s$	15.5	$\theta_{v,s,i}$	0°
Φ	0.52	$\theta_{v,e,i}$	224°
$T_{f,w}$	380 K	$p_{n,i}$	357 kPa
fuel injection		$T_{n,i}$	329 K
$M_{F,o}$	0.216 g	exhaust valve:	
N_d	50	$N_{v,e}$	1
D_{SM}	100 μ m	$C_{D,e}$	0.7
$u_{d,o}$	100 m/s	$D_{v,e}$	0.042 m
$T_{d,o}$	500 K	$L_{v,e}$	$0.25D_{v,e}$
$\theta_{F,s}$	363°	$\theta_{v,s,e}$	474°
$\theta_{F,e}$	393°	$\theta_{v,e,e}$	720°
regenerator		$p_{n,e}$	251 kPa
schedule:		$T_{n,e}$	800 K
$\theta_{r,c,s}$	345°		
$\theta_{r,c,e}$	380°		
$\theta_{r,h,s}$	420°		
$\theta_{r,h,e}$	515°		

3.3 Results and Discussion

The results on engine performance, enhanced droplet evaporation, superadiabatic combustion, and optimization of thermal regeneration are given below.

3.3.1 Model Calibration

In order to verify the results of the engine simulation, the simulation results of the conventional Diesel engine were calibrated with those found using the simulation code of Caterpillar Inc. The Caterpillar code has a lumped gas model, a detailed chemical reaction model and the detailed mass flow rate model during the intake and exhaust and the surface-convection model based on the Woschni relation. The calibration was done by adjusting the coefficients in the surface-convection heat transfer model and the mass flow rate model. It was assumed that the result of calibrated heat transfer model can be used for the regenerative engine.

The mass flow rate during the intake and exhaust periods is compared with the results of the Caterpillar code in Figure 3.4. The overall results are in a good agreement except during the exhaust period. This is due to the fluctuating pressure in the exhaust maifold which is not considered in the current simulation code. The mass variation in the cylinder is shown in Figure 3.5. The heat loss rate is shown in Figure 3.6 and the variations of the gas temperature and pressure are shown in Figures 3.7 and 3.8 respectively.

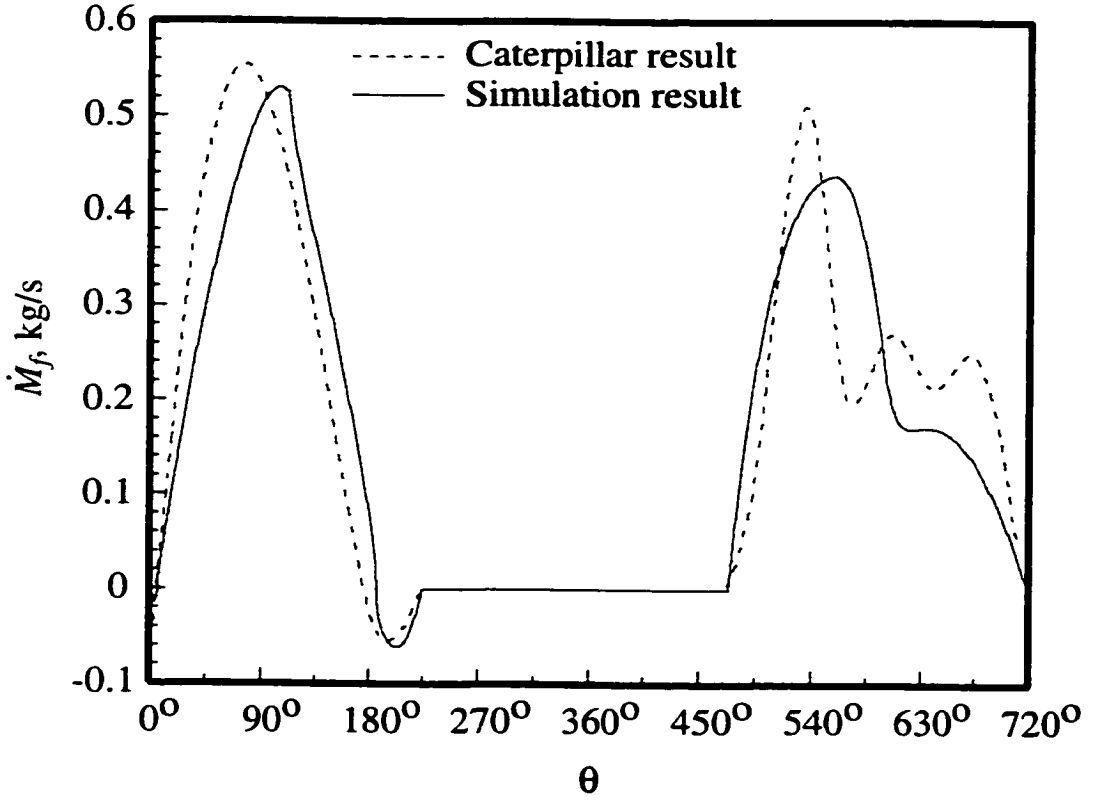

Figure 3.4: Comparison of the mass flow rates of the simulation code and Caterpillar's code.

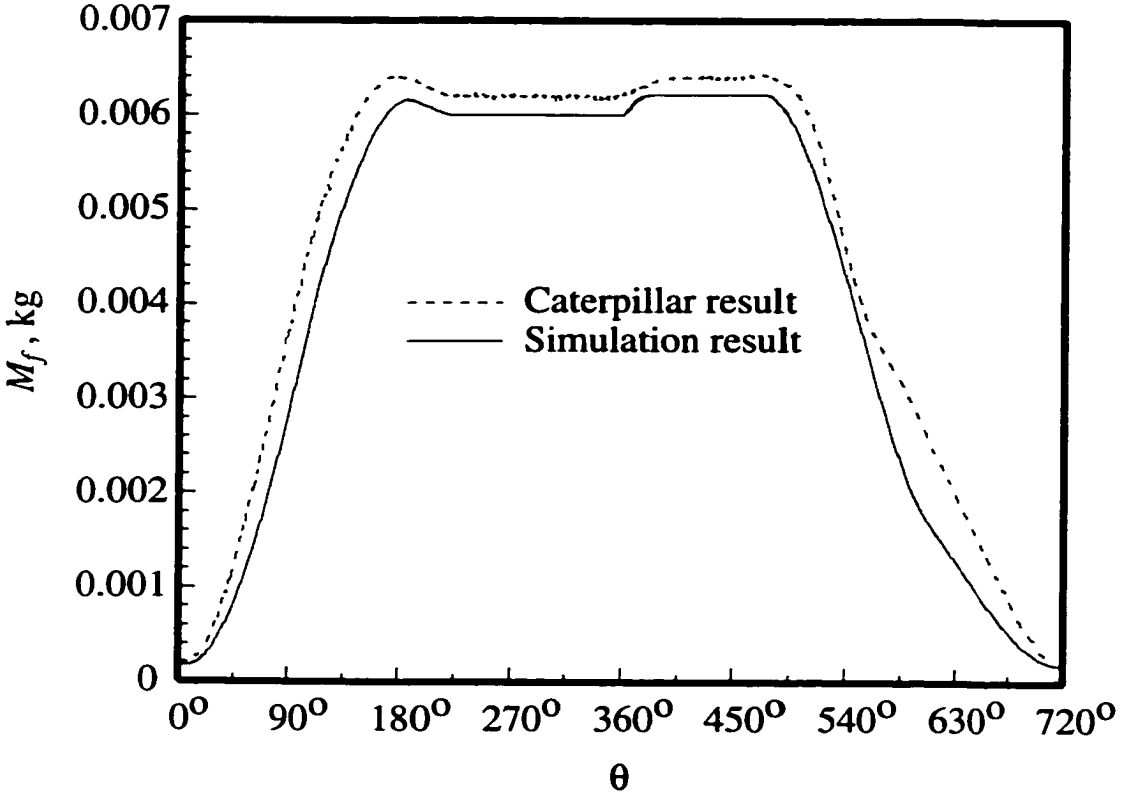

Figure 3.5: Comparison of the in-cylinder gas mass of the simulation code and Caterpillar's code.

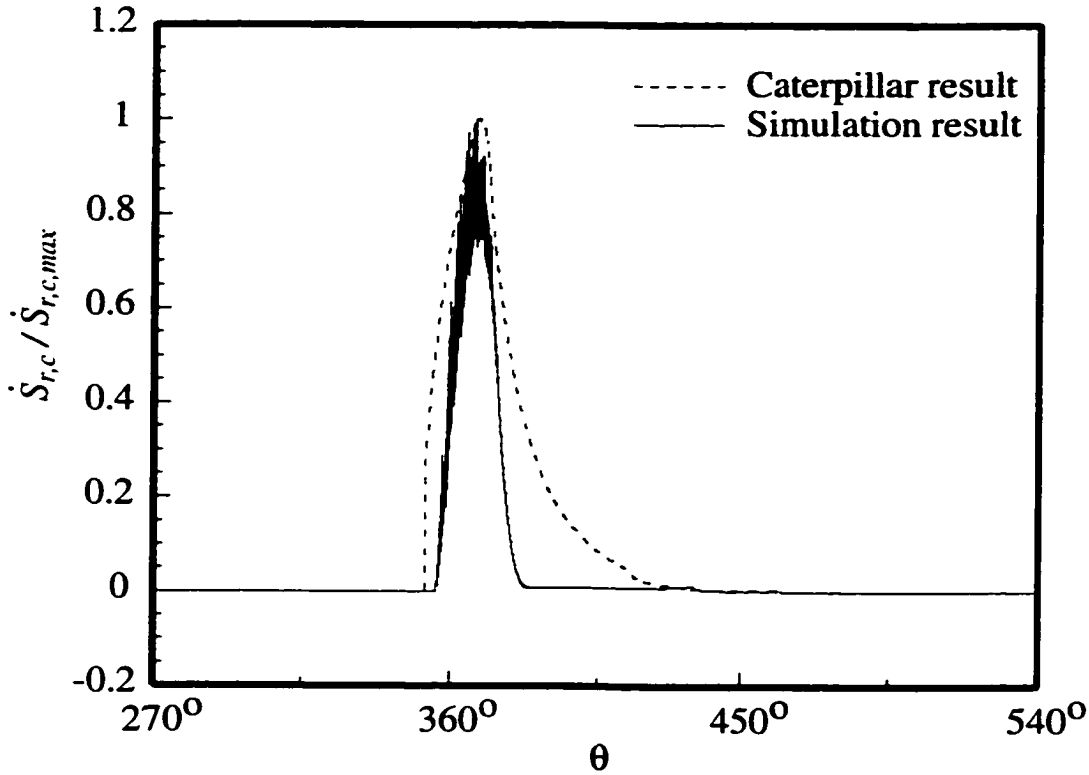

Figure 3.6: Comparison of the heat release rates of the simulation code and Caterpillar's code.

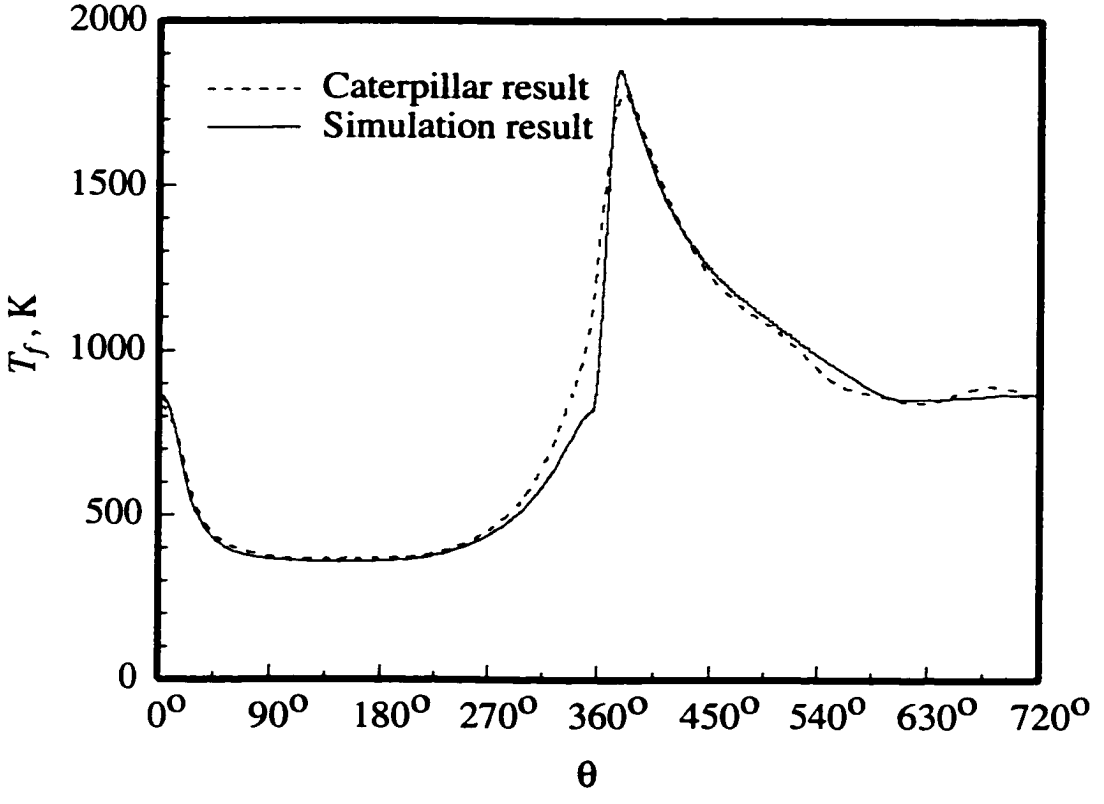

Figure 3.7: Comparison of the gas temperatures of the simulation code and Caterpillar's code.

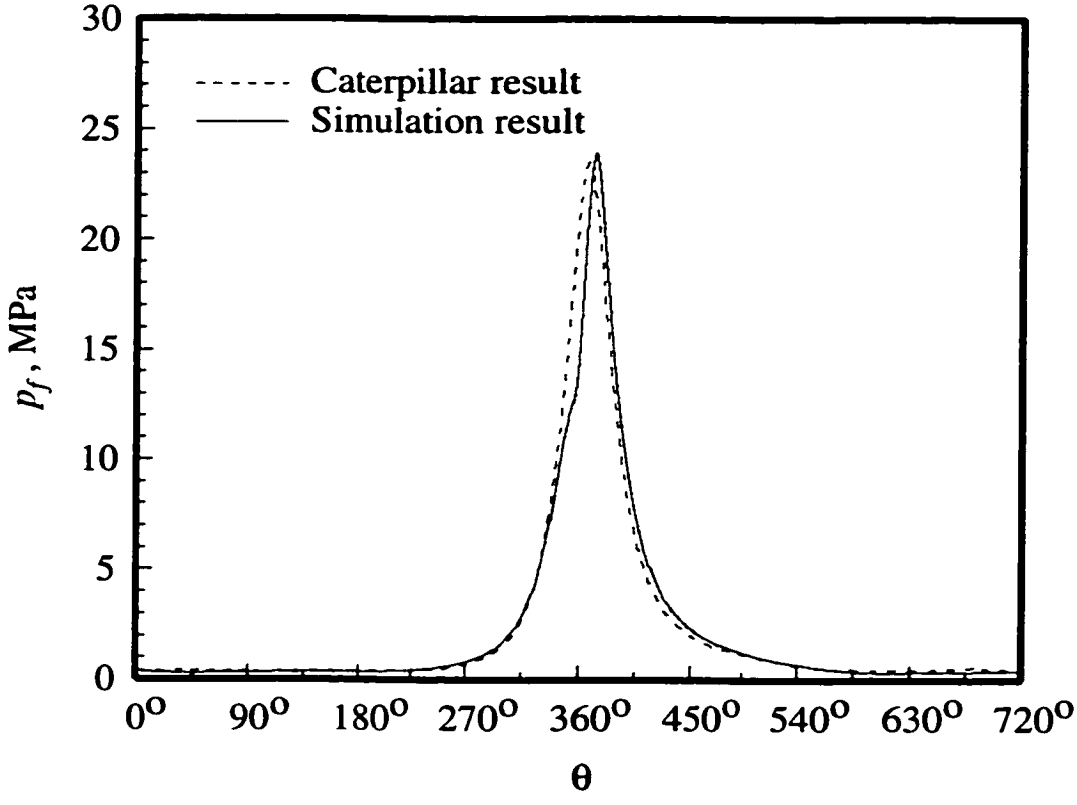

Figure 3.8: Comparison of the gas pressures of the simulation code and Caterpillar's code.

3.3.2 Thermal and Mechanical Performance

The $(p\text{-}V)_f$ diagram obtained from the analysis of the conventional and regenerative Diesel engines is shown in Figure 3.9. The thermodynamic limit results, shown in Figure 3.9, assume a constant volume process during thermal regeneration and a maximum regenerator temperature below $T_{r,max} = 1,600$ K. The work gained due to thermal regeneration is denoted as $A_1 - A_2$. Compared to the thermodynamic limit, the work loss due to insufficient thermal regeneration and the pressure drop through the regenerator (denoted as B), and the prolonged combustion of the Diesel engine (denoted as C), are detrimental to the thermal efficiency. The optimum performance should reduce the pressure drop and improve the combustion characteristics. Note that the compression ratio of the regenerative Diesel engine is lower than that of the conventional engine. This is due to the regenerator volume ($l_r = 8$ mm), the gap (0.5 mm) between the regenerator top surface and the cylinder head, and the gap (1 mm) between the regenerator bottom surface and the piston.

Figure 3.10 shows the mass flow rate during the intake, $\dot{M}_{f,int}$, the mass flow rate during the exhaust stroke, $\dot{M}_{f,exh}$, the mass flow rate into the top gas zone from the regenerator, $(\dot{M}_{f,r})_{N_i}$, and the fuel evaporation rate, $\dot{M}_{F,evp}$. Note that the intake flow of $\dot{M}_{f,int}$ has a back flow due to the reversal of the pressure difference between the valve inlet and the bottom gas zone, and that there is a reciprocating flow of $(\dot{M}_{f,r})_{N_i}$ through the porous regenerator. The reciprocating flow is attributed to the pressure differences caused by the regenerator/piston motion, the heat transfer, and the combustion. This allows for the thermal regeneration of the flue gas heat resulting in a superadiabatic combustion.

The temperature variations of the solid and gas phases during a cycle are shown in Figure 3.11. Fuel evaporation and combustion occur during thermal regeneration

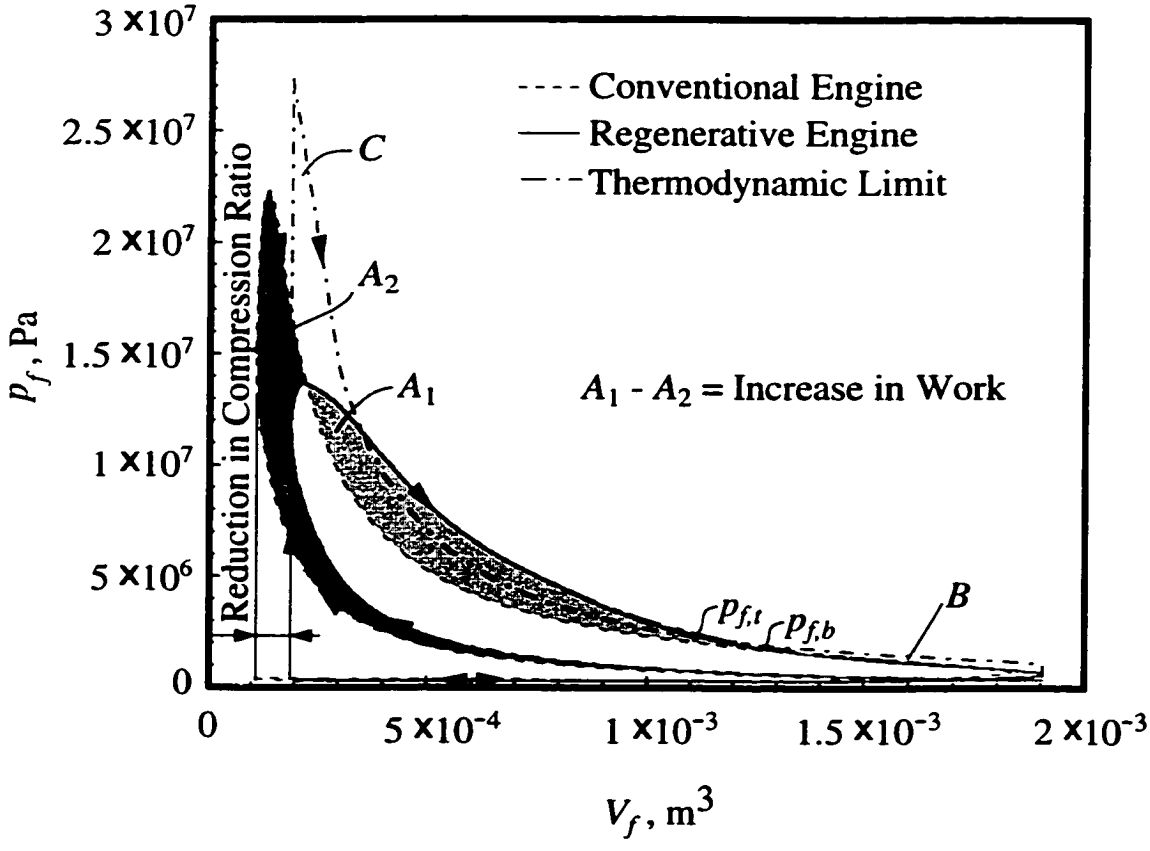

Figure 3.9: Thermodynamic limit and predicted $(p\text{-}V)_f$ diagram from the start of cycle $\theta = 0°$ to the end $\theta = 720°$, for the conventional and regenerative engines.

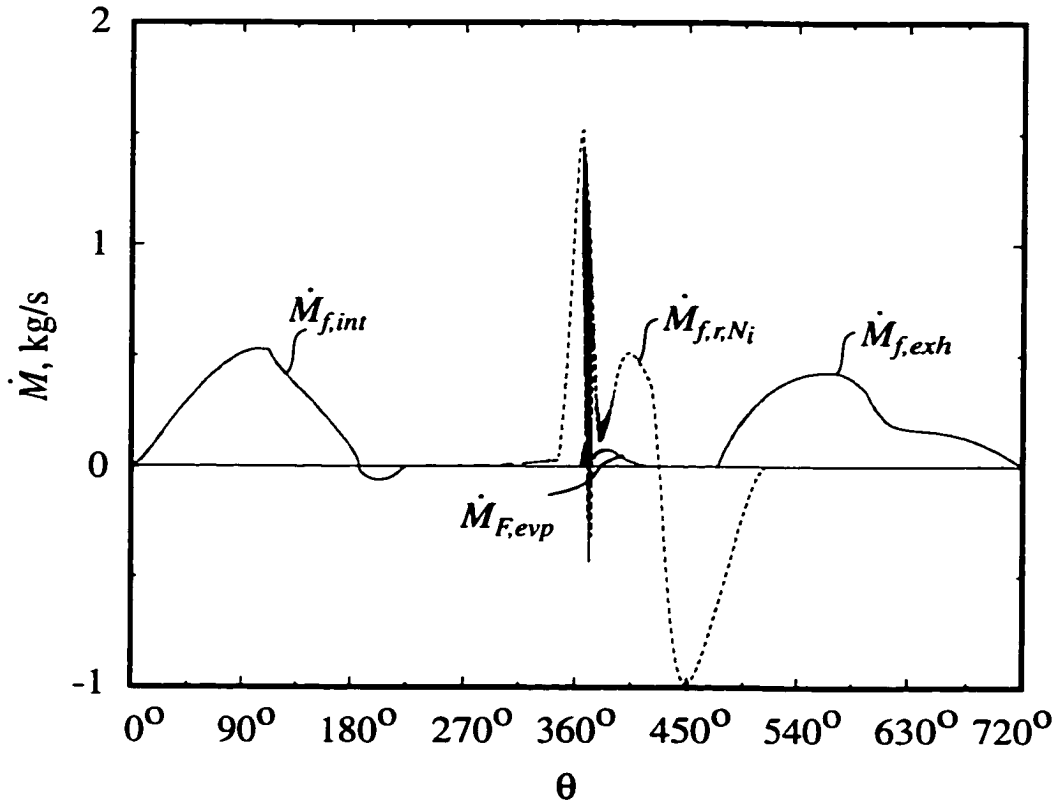

Figure 3.10: Variation of Mass flow rates during the intake and exhaust strokes, and the mass flow rate through the insert during the compression and expansion strokes, during a cycle.

resulting in a high peak gas temperature in the top gas zone and a relatively low peak gas temperature in the bottom gas zone. Note also that the ceramic cylinder head is insulated from the cylinder block (made of cast iron). The surface temperature of the cylinder head $T_{ch,o}$ is higher than that of the conventional Diesel engine, but the surface temperatures of the cylinder block $T_{cb,o}$ and the surface temperature of the aluminum piston $T_{p,o}$ are lower. The surface temperature $T_{r,L}$ of the regenerator made of SiC, also has a large temperature variation.

Figure 3.12 shows the variations of the mass, volume, and temperatures of the top and bottom gas zones, and the top gas zone pressure during the cycle. Since thermal regenerative heating occurs after the intake valve is closed, the volumetric efficiency of the regenerative engine is not deteriorated by regneration. The higher volumetric efficiency, about 92 percent, is due to the lower surface temperature in the bottom chamber.

The energy conversion, and surface heat transfer rates in the top and bottom gas zones are shown in Figures 3.13(a) to (c). The heat release rate $\dot{S}_{r,c}$ is controlled only by fuel evaporation (due to the assumed perfect mixing). The heat transfer rate, Q_u, due to the thermal regeneration, shown in Figures 3.13(b) and (c), enhances the fuel evaporation and leads to a superadiabatic combustion. Also the surface-radiation heat transfer $-(\dot{S}_{e,\epsilon}+\dot{S}_{e,\alpha})_t$ in the top chamber is comparable to the surface-convection heat transfer $\langle Q_{ku}\rangle_{D_B}$, due to the high surface temperature as shown in Figure 3.13(b).

Under the baseline conditions (including $r_c = 10$) given in Table 3.2, the predicted thermal efficiency of the regenerative engine is $\eta_T = 52$ percent, the volume efficiency is $\eta_V = 92$ percent, the indicated mean-effective pressure is $p_{mep,in} = 2.79$ MPa, and the indicated specific fuel consumption is $sfc = 163$ g/kW-hr.

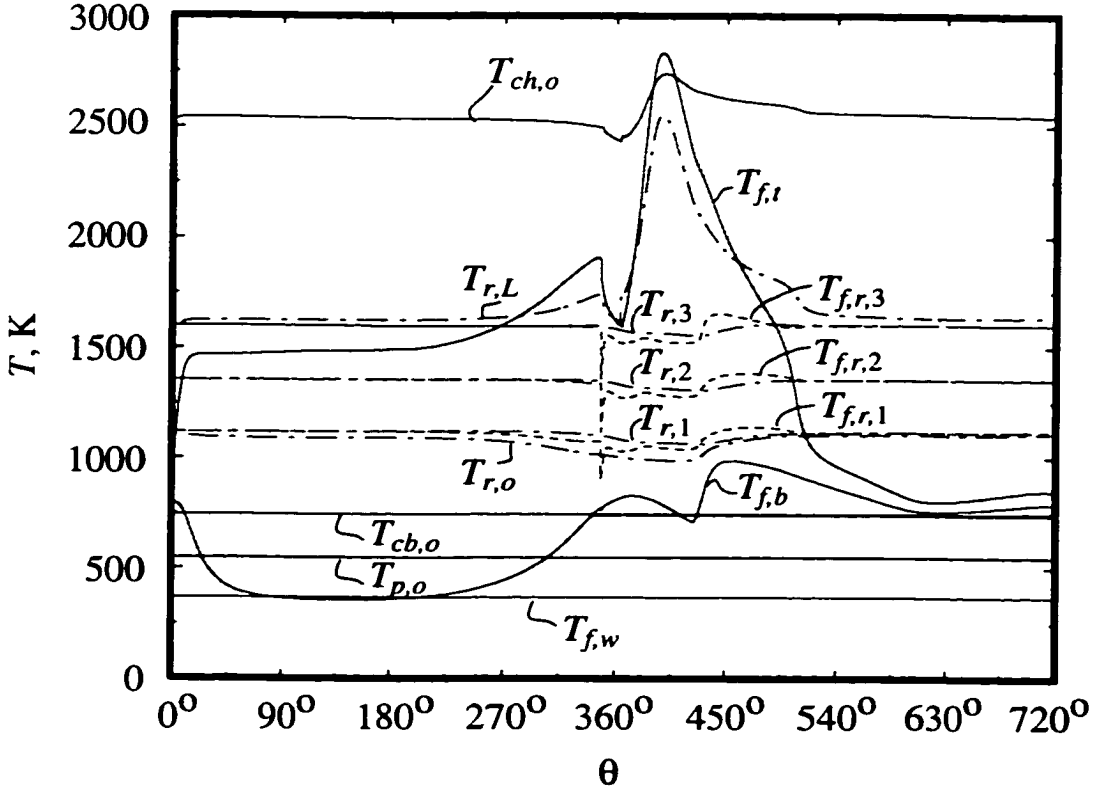

Figure 3.11: Variations of the gas and solid temperatures during a cycle.

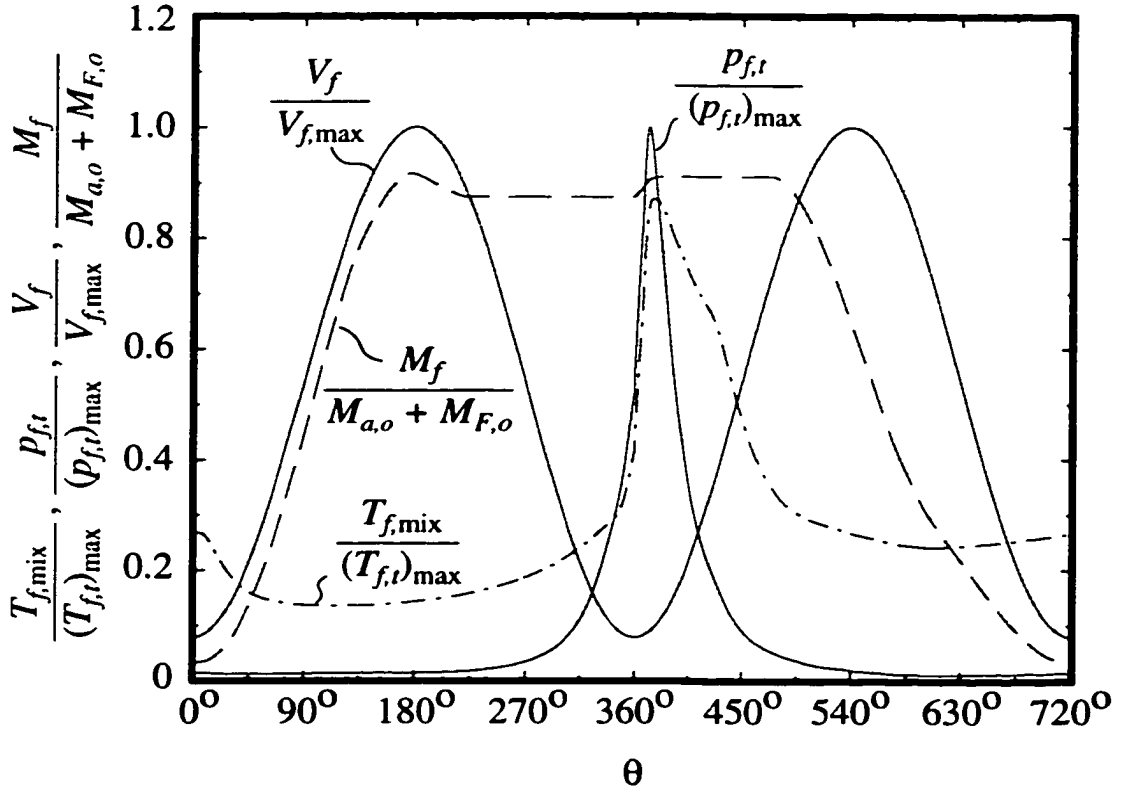

Figure 3.12: Variations of dimensionless mass, volume, temperature (top and bottom gas zones), and pressure in top gas zone, during a cycle.

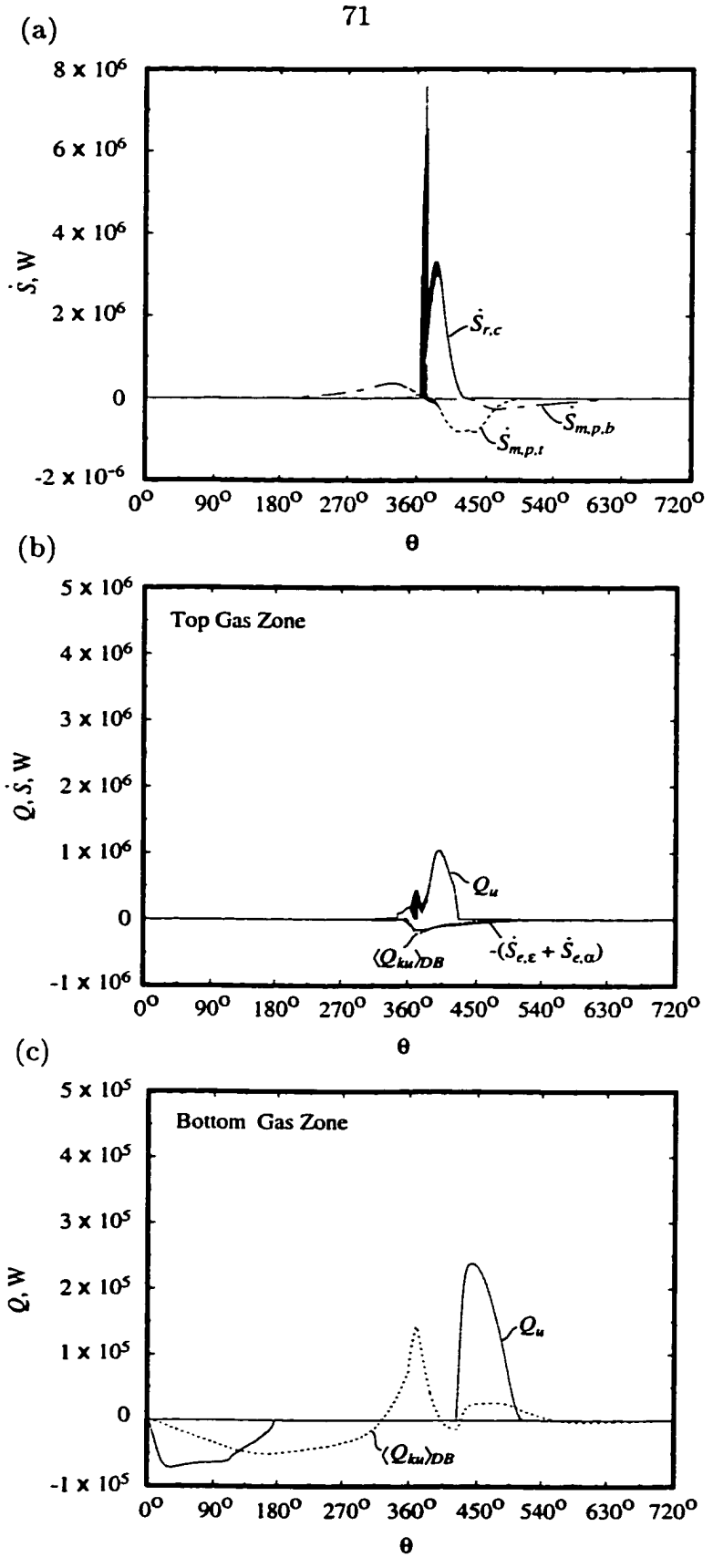

Figure 3.13: Variation of the energy conversions (a) and heat transfer rates (b) and (c), during a cycle.

3.3.3 Enhanced Evaporation

Since the fuel is injected toward the regenerator, which is located near the fuel injection nozzle, droplet impingement onto the regenerator is likely. The impinging droplets experience film boiling once in contact with the high temperature (above the Leidenfrost temperature) regenerator pore surface and are quickly vaporized. In addition to the high gas temperature (due to the thermal regeneration), the fuel impingement on the high temperature pore surface drastically reduces the evaporation time. Optimal fuel injection aims to achieve rapid fuel vaporization and uniform vapor distribution (in the top gas zone) with the least thermal impact on the porous regenerator, for the maximum performance.

The spray divergence angle θ_d is determined from the empirical correlation for a given nozzle geometry (Heywood, [27]) and is given as

$$\tan(\frac{\theta_d}{2}) = \frac{4\pi}{4.9}(\frac{\rho_{f,t}}{\rho_{F,l}})^{\frac{1}{2}}\frac{\sqrt{3}}{6}. \tag{3.32}$$

Figure 3.14(a) shows the penetration of the fuel spray into the top gas zone and the consequent impingement onto the moving regenerator. Figure 3.14(b) shows the fuel evaporation rate and the trajectories of the fuel droplet parcels (1st, 20th, 40th, and 50th of the 50 droplet parcels), the regenerator, and the piston. Once the fuel droplet makes contacts the porous regenerator, the fuel evaporation rate $\dot{M}_{F,evp}$ rapidly increases. The evaporation of the captured droplets helps to provide rapid fuel evaporation enabling intense premixed combustion, and increasing the peak pressure and the thermal efficiency. The air flow emanating from the regenerator deflects the droplets and helps to provide a uniform fuel-vapor distribution in the top gas zone. Using a plug flow model for this air flow, Figure 3.14(b) shows that the front of the plug flow reaches the cylinder head for most of the fuel injection period

and, therefore, ideal perfect mixing in the top gas zone can be justifiably used.

Since the regenerator moves with a high acceleration during the thermal regeneration, excess thermal stress due to the variation of the solid temperature should be avoided. To reduce the thermal stress, surface vaporization cooling due to the impinging fuel droplets should be distributed over a larger portion of the regenerator area, thus minimizing the temperature variation along the regenerator surface. Figure 3.15 shows that the filteration efficiency α of the first and last impinging fuel droplet parcels captured within about 4 pores (< 1 mm) for a 8 mm thickness regenerator. Also shown is that the temperature variation of the regenerator is rather small for the fuel impingement. Note that the temperature variation is affected surface-convection, conduction, radiation, and fuel droplet evaporation.

3.3.4 Superadiabatic Combustion

The superadiabatic flame temperature, due to thermal regeneration of the combustion heat, increases the thermal efficiency. Figure 3.16 shows that the peak gas temperature $T_{f,t}$ in the top gas zone of the regenerative engine is higher than that of the conventional engine. The mixture gas temperature $T_{f,mix}$ of the top and bottom gas zone is also higher than the gas temperature of the conventional engine, but only during the combustion period. The superadiabatic flame temperature during the fuel injection period, enhances the fuel evaporation. The enhanced fuel evaporation assists the intense combustion resulting in an increase of the peak pressure and engine power.

Note that the porous regenerator has the potential for soot trapping during the regenerative cooling stroke. During the regenerative heating stroke (air is preheated while flowing through the regenerator from the bottom gas zone to the top gas

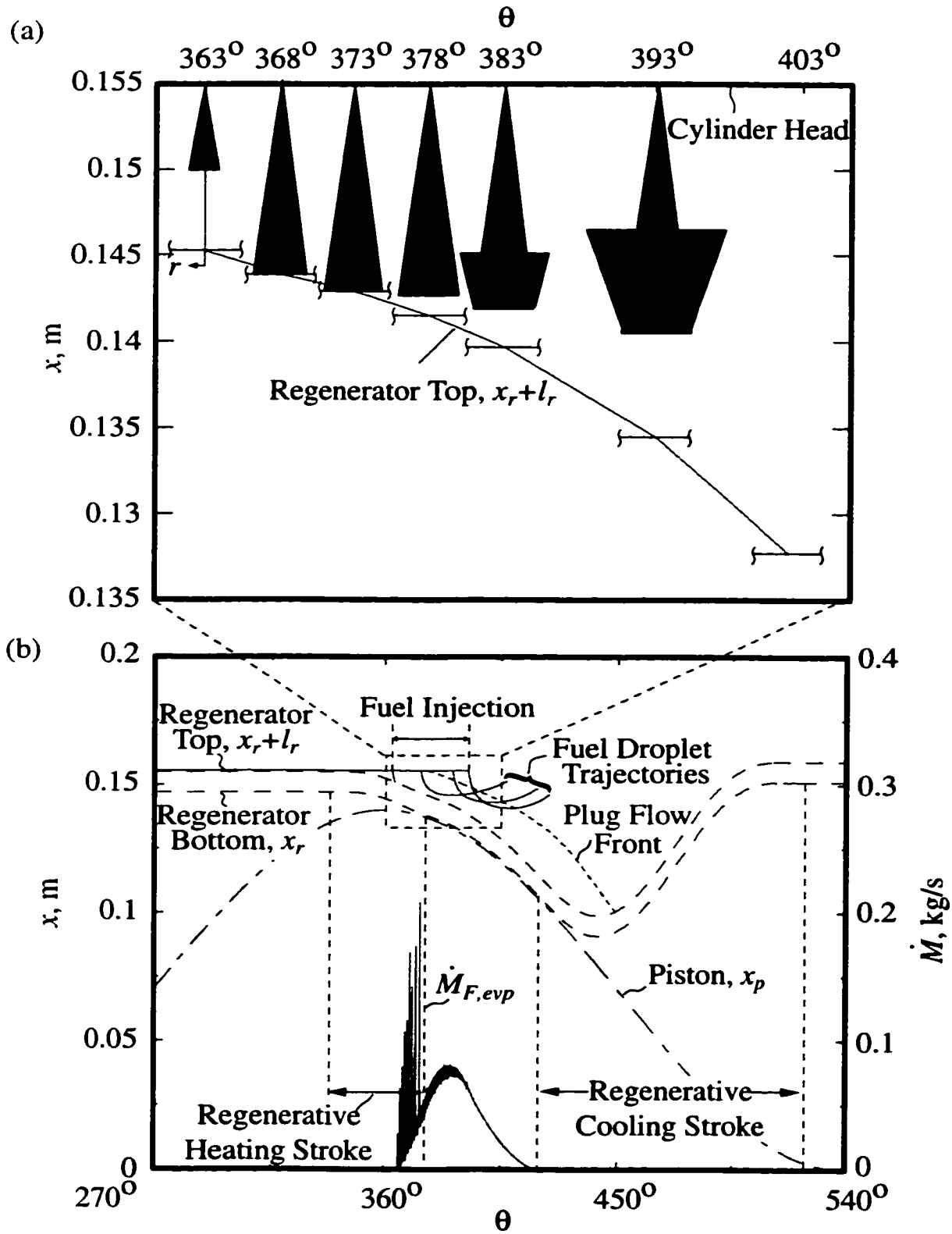

Figure 3.14: (a) Penetration and surface impingement of fuel spray, and (b) the trajectories of the fuel droplets and the front location for plug gas flow in top gas zone.

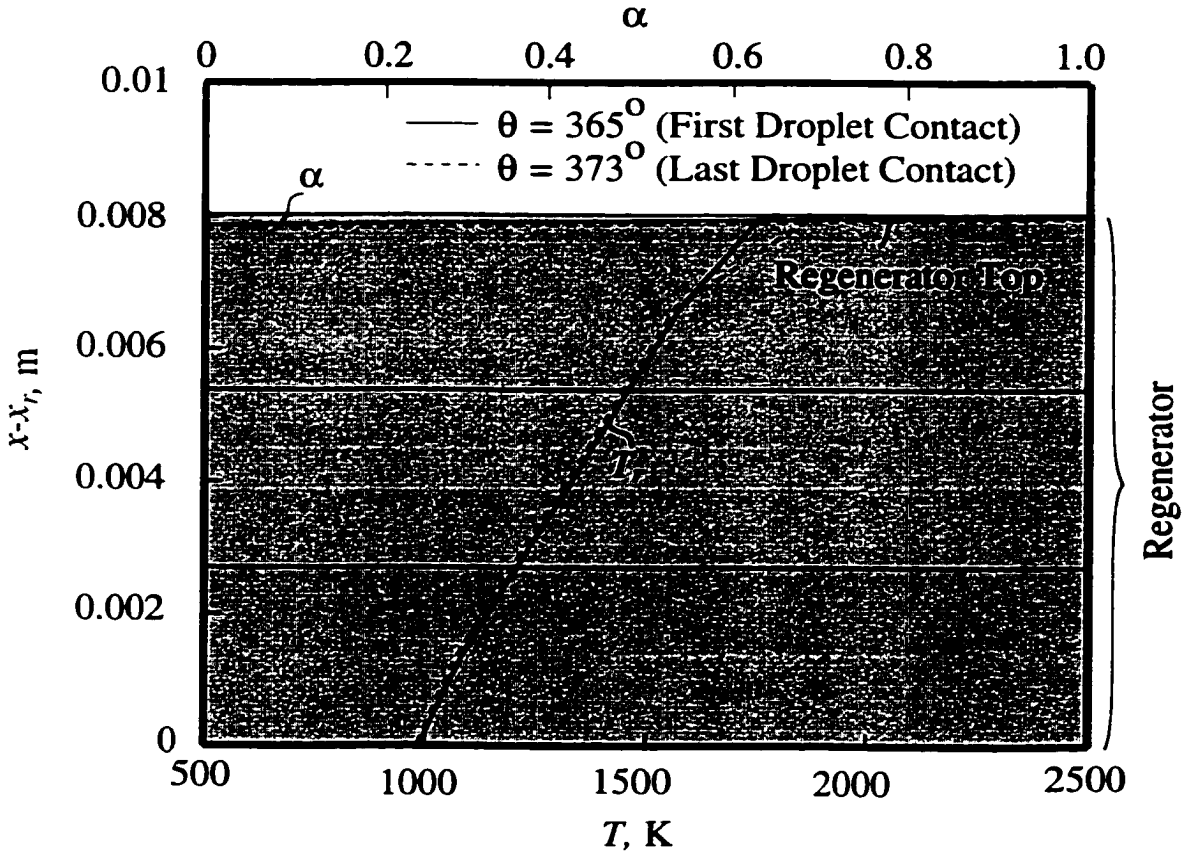

Figure 3.15: The filteration efficiency of the first and last impinging fuel droplet parcels and the temperature distribution within the regenerator insert.

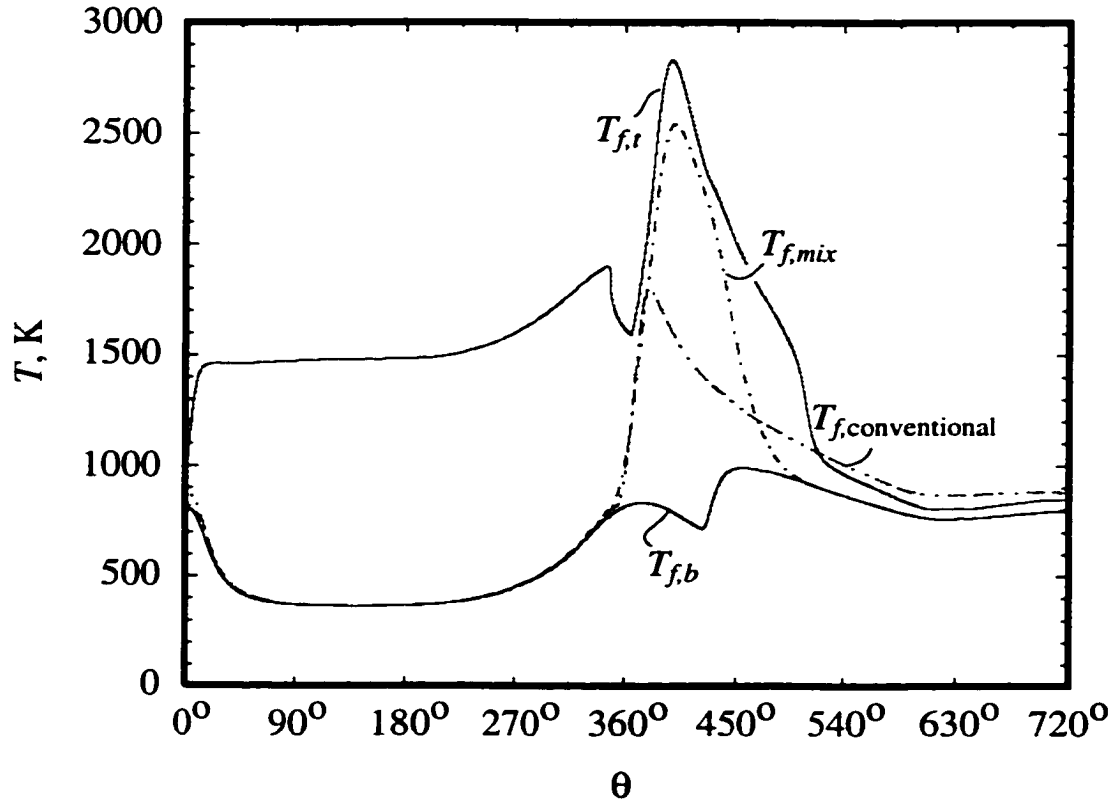

Figure 3.16: Variations of gas temperatures in the regenerative and the conventional engines, during a cycle.

zone), the preheated oxidant comes in contact with the trapped soot particles in the regenerator pores and can oxidize the soot. The higher gas temperature, due to the superadiabatic combustion, will also be beneficial in reducing the soot formation (because oxidation of the soot is enhanced). However, the higher gas temperature increases the thermal NO_X production (a 500 K increase in the flame temperature produces about 800 time more NO_X). Lowering the peak flame temperature, by controlling the fuel injection timing, the thermal regeneration, and by using a fuel-lean mixture, would then become necessary to control NO_X emissions.

3.3.5 Optimization of Thermal Regeneration

The optimum motion schedule of the regenerator for a high thermal efficiency, requires to the maximum thermal regeneration and to the minimum mechanical work loss due to the regenerator pressure drop.

Figure 3.17 shows that for the maximum thermal efficiency, the optimum regenerative heating and cooling strokes begin at 340° and 430° for prescribed stroke durations of 35° and 95°, respectively (for the regenerative heating stroke, $\theta_{r,h,s} \sim \theta_{r,h,e}$, and for the regenerative cooling stroke, $\theta_{r,c,s} \sim \theta_{r,c,e}$). The optimum regenerative heating stroke would create a high gas temperature and more fuel impingement on the the regenerator, and thus enhances evaporation. A retarded regenerative heating stroke decreases thermal regeneration period during the fuel injection and therefore does not achieve a higher super-adiabatic temperature.

The optimum regenerative cooling stroke using the high exhaust temperature, optimizes the work gain by the thermal regeneration and the work loss by the pressure drop. An advanced regenerative cooling stroke recovers the combustion heat at a higher temperature, thus increasing the regenerator temperature and the supera-

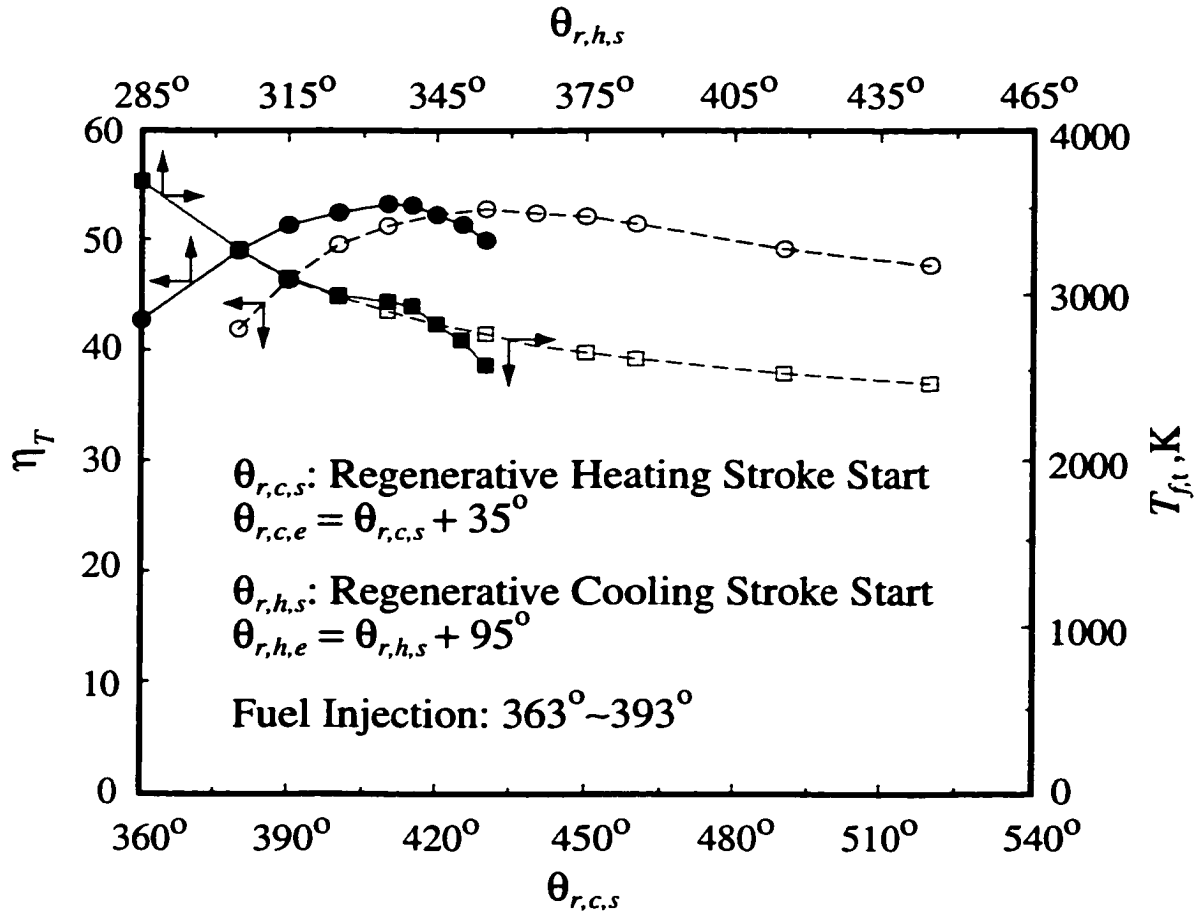

Figure 3.17: Effect of the regenerative heating and cooling stroke periods on the thermal efficiency.

diabatic flame temperatures. The retarded regenerative cooling stroke results in a higher expansion pressure due to higher exhaust gas temperature, thus increasing the work loss due to the regenerator pressure drop.

Figure 3.18 shows the effect of the compression ratio on the thermal efficiency. The maximum thermal efficiency of $\eta_T = 52$ percent is predicted at a compression ratio of $r_c = 10$. The maximum compression ratio r_c in the regenerative engine is limited to values below 14 due to the dead volume of the regenerator and the tolerance gaps. For maximum thermal efficiency, a optimum compression ratio of $r_c = 10$ is obtained.

3.4 Summary

The enhanced fuel evaporation, by droplet-regenerator interaction and air preheating, results in a more uniform fuel-vapor distribution and a dominant premixed combustion regime. The increase in the superadiabatic flame temperature enhances the fuel evaporation and increases the peak pressure, which correspondingly increases the thermal efficiency. Here the fuel-injection timing, and the motion of the regenerator are optimized for a higher thermal efficiency. For the optimum compression ratio of $r_c = 10$, a thermal efficiency of $\eta_T = 52$ percent is predicted, compared to 45 percent of the conventional Diesel engine with a higher compression ratio.

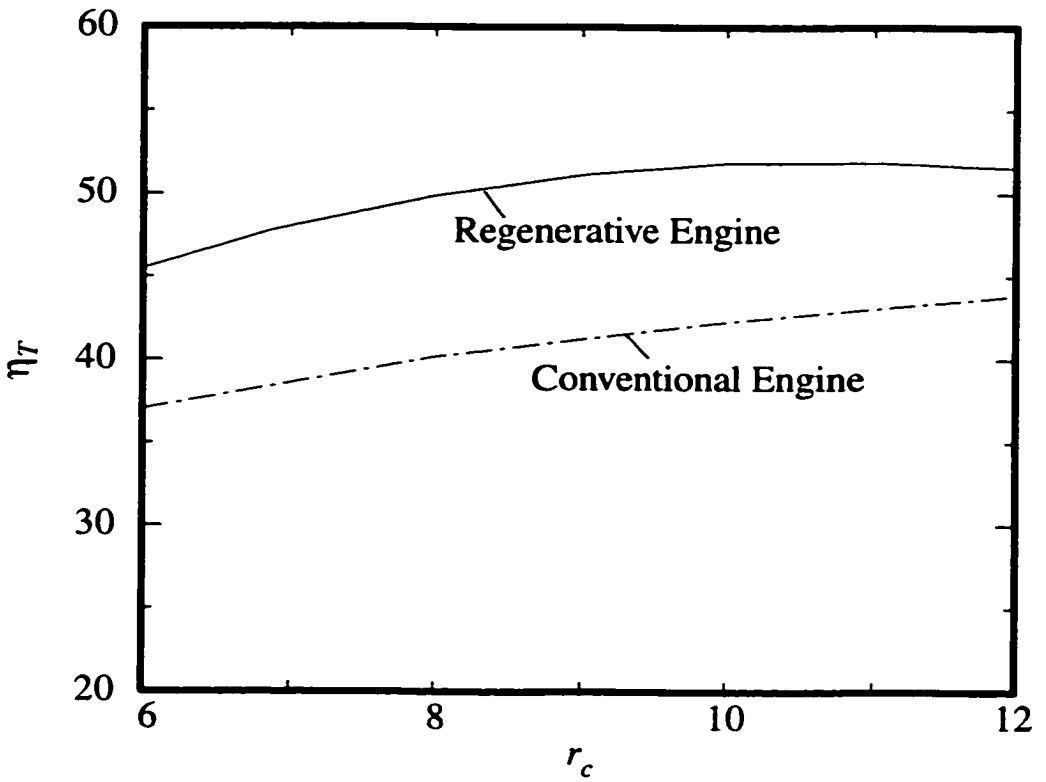

Figure 3.18: Effect of compression ratio on the thermal efficiency of the regenerative and conventional engines.

CHAPTER IV

CONCLUSION

Bounding solid surfaces containg reciprocating, reacting gas streams, allow for heat storage/release in the gas stream, i.e., thermal regeneration, and achievement of local superadiabatic temperatures. In addition to the reciprocating flow, fuel-injection allows for control of the flame location, and then ideally unlimited pre-heating of the oxidant (therefore, much higher superadiabatic temperatures). The local superadiabatic temperatures are exploited to achieve high thermal efficiency power generation systems, such as direct thermoelectric power generation systems and regenerative Diesel engines.

The optimization between thermal regeneration (to achieve higher superadiabatic temperatures) and pressure drop (of the reciprocating flow across the solid matrix) allows for the maximization of the thermal efficiency in such power generation systems. While the solid thermal conductivity in the unidirectional flow arrangements, is required for the heat feedback to the cold upstream gas stream, the solid thermal conductivity in the reciprocating flow arrangement is not needed any longer. In the regenerative Diesel engine, the pre-combustion process, including fuel evaporation

and fuel vapor-air mixing, are also assisted by the superadiabatic temperature, resulting in a rapid evaporation of fuel droplets on the hot solid surface and an increase of turbulence intensity. The optimization of the entire combustion processes (including the pre-combustion and reaction process) and the motion of the reciprocating piston, allow for maximum conversion of the combustion heat to mechanical work.

The effect of thermal regeneration in reciprocating, reacting streams, and the optimum thermal efficiency, were analyzed for two power generation systems, namely direct thermoelectric power generation and the regenerative Diesel engine.

4.1 Combustion-Thermoelectric Tube

The combustion-thermoelectric tube has a reciprocating, reacting stream with localized fuel injection within the tube and achieves a local superadiabatic temperature. This results in the large solid temperature difference between the hot and cold junctions of the thermoelectric module. This temperature difference is used for an electrical power generation using the Seebeck effect and high-temperature thermoelectric materials, such as $Si_{0.7}Ge_{0.3}$.

4.1.1 Objective

The objective of the analysis is to optimize the thermoelectric power generation system using numerical simulations.

4.1.2 Analysis

In direct combustion-thermoelectric energy conversion, direct fuel injection and reciprocation of the air flowing into a solid matrix are combined with the solid-gas interfacial heat transfer to allow superadiabatic temperatures to be reached at the hot junction. During the present study, a combustion-thermoelectric tube was introduced and analyzed. Radially averaged temperatures were used for the fluid and solid phases in conjunction with a first-order Arrhenius reaction model.

4.1.3 Results

A combination of direct injection of the fuel and external cooling of the cold junctions has been used to increase the energy conversion efficiency for high-melting temperature thermoelectric materials. The relatively large thermal conductivity of the available high-temperature thermoelectric materials (e.g., Si-Ge alloys) results in a large conduction loss from the hot junctions and deteriorates the performance.

The present parametric study (geometry, flow, stoichiometry, materials) shows that with the current high figure of merit and high temperature $Si_{0.7}Ge_{0.3}$ properties, a conversion efficiency of about 11 percent is achievable. With lower thermal conductivities for these high-temperature materials, efficiencies about 25 percent appear possible. This makes this energy conversion system comparable to other high efficiency, direct, electric power generation methods.

4.1.4 Recommendations for Future Work

The analysis should be extended to consider more realistic geometries, such as the presence of the dielectric layer between the p and n thermoelectric materials. The thermal and electric contact resistances at the hot and cold junctions, and at the interface of the combustion region and thermoelectric regions, also should be addressed. Fabrication of the prototype is also recommended for the experimental verification of the thermoelectric system. New high-temperature materials should be studied as well. Finally, in order to predict the thermodynamic limit of the thermal efficiency, a study of the maximum achieveable flame temperature should be made.

4.2 Regenerative Diesel Engines

A regenerative Diesel engine which uses an in-cylinder reciprocating, porous regenerator is analyzed for its potential to achieve superadiabatic temperatures and high-thermal efficiencies. The higher efficiency is due to the improved pre-combustion processes (i.e., rapid fuel evaporation and enhanced fuel-air mixing) and combustion processes assisted by the superadiabatic temperature.

4.2.1 Objective

The objective is to examine the role of the porous insert motion and fuel injection strategies on fuel evaporation-combustion and engine efficiency, using an existing in-cylinder thermal regeneration concept for Diesel engines.

4.2.2 Analysis

A two-gas zone and a single-step Arrhenius reaction model are used with a Lagrangian droplet tracking model that allows for filtration by the insert. The filtration model and the film-evaporation model of impinging fuel droplets onto the porous regenerator are used to determine the effects of the regenerator on enhancement of fuel evaporation. The fuel vapor and the oxidant concentration in the top region of the cylinder controls the heat release rate.

4.2.3 Results

While the heated air emanating from the porous regenerator enhances fuel evaporation, thus resulting in a superadiabatic combustion and increasing thermal effi-

ciency, the corresponding increase in the thermal NO_X is undesirable. A thermal efficiency of 52 percent is predicted, compared to 45 percent for conventional Diesel engines. Optimum regenerative strokes are found. The optimal regenerative cooling stroke occurs close to the peak flame temperature, thus increasing the superadiabatic flame temperature and the peak pressure, while decreasing the expansion stroke pressure and the pressure drop through the insert. During the regenerative heating stroke, the heated air enhances droplet evaporation, resulting in a more uniform, premixed combustion, higher peak pressure, and thus larger mechanical work.

4.2.4 Recommendations for Future Work

Further optimization of the regenerative Diesel engine can be made using parameters such as fuel injection timing and the properties of the porous regenerator. Consideration of multi-dimensional flow, heat transfer and combustion with more detailed chemical reactions and kinetics, are recommended for accurate prediction of the pollutant formation. Finally, use of a stationary regenerator, similar to those used in Stirling cycle engines, may overcome the potential difficulties of insert design and durability.

4.3 Summary

It was shown that the superadiabatic temperature obtained using thermal regeneration in reciprocating reacting streams with fuel injection, improves the entire combustion processes (including fuel evaporation and fuel-vapor mixing). This results in high thermal efficiencies for power generation systems, such as direct thermoelectric power generation and the regenerative Diesel engine. It was also shown that fuel injection provides a way to control the flame location and achieve a higher superadiabatic temperature (due to the unlimited preheating of the oxidant).

The concept of the thermal regeneration in reciprocating reacting streams with fuel injection could be successfully applied to other applications demanding high superadiabatic temperatures such as high-efficiency radiant burners, fixed-bed catalytic reactors for pollutant after-treatment and regenerative soot filtration.

APPENDICES

APPENDIX A

DETAILED FORMULATIONS OF REGENERATIVE DIESEL ENGINE

A.1 Heat Transfer

Terms appearing in the energy conservation Eq. (3.2) of the top gas zone are given below. The heat transfer due to the fuel injection is

$$Q_{u,inj} = -\dot{M}_{F,inj} c_{p,F} T_{F,o}. \tag{A.1}$$

The surface-convection heat transfers between the top gas zone and surfaces of the cylinder head, the cylinder block, and the top regenerator surface $\langle Q_{ku} \rangle_{D_B}$, are

$$\begin{aligned} \langle Q_{ku,t\text{-}ch} \rangle_{D_B} &= \frac{(T_{f,t} - T_{ch,o})}{\langle R_{ku,t\text{-}ch} \rangle_{D_B}}, \quad \langle Q_{ku,t\text{-}cb} \rangle_{D_B} = \frac{(T_{f,t} - T_{cb,o})}{\langle R_{ku,t\text{-}cb} \rangle_{D_B}}, \\ \langle Q_{ku,t\text{-}r} \rangle_{D_B} &= \frac{(T_{f,t} - T_{r,L})}{\langle R_{ku,t\text{-}r} \rangle_{D_B}}, \end{aligned} \tag{A.2}$$

where the surface-convection resistance is given as

$$\langle R_{ku,t} \rangle_{D_B} = \frac{D_B}{\langle \mathrm{Nu} \rangle_{D_B,t} k_f A_{ku,t}}, \tag{A.3}$$

where $\langle \mathrm{Nu} \rangle_{D_B,t}$ is determined from the Woschni correlation using the average cylinder gas velocity and the cylinder pressure (Woschni, [37]), as given below

$$\langle \mathrm{Nu} \rangle_{D_B,t} = 0.035 \mathrm{Re}_{D_B,t}^{0.8}, \quad \mathrm{Re}_{D_B,t} = \frac{\rho_{f,t} D_B \langle u \rangle_t^f}{\mu_f}. \tag{A.4}$$

Here $\langle u \rangle_t^f$ is given by

$$\langle u \rangle_t^f = c_1 (\overline{u_{p,t}^2})^{1/2} + c_2 \frac{V_f (p_{f,t} - p_m)}{(M_{a,o} + M_{F,o}) \frac{R_g}{M_g}}, \tag{A.5}$$

where

$$(\overline{u_{p,t}^2})^{1/2} = 2 L_d N \frac{2\pi(\mathrm{rad/rot})}{60(\mathrm{s/min})}, \quad p_m V_f = M_f \frac{R_g}{M_g} T_n$$

and for intake and exhaust, $c_1 = 6.18$ and for compression and expansion, $c_1 = 0.28$ and for intake, compression and exhaust, $c_2 = 0$ and for expansion, $c_2 = 0.00324$ m/s-K. Similarly, in the bottom gas zone, $\langle \mathrm{Nu} \rangle_{D_B,b}$ is determined and for intake and exhaust, $c_1 = 6.18$ and for compression and expansion, $c_1 = 0.28$ and for intake, compression and exhaust, $c_2 = 0$ and for expansion, $c_2 = 0.00324$ m/s-K.

The energy conversion terms in the top gas zone are

$$\dot{S}_{r,c} = \dot{M}_{r,F} \ \Delta h_{r,F}, \ \dot{S}_{m,p,t} = V_{f,t} \frac{dp_{f,t}}{dt}, \ \dot{S}_{F,lg} = -\dot{M}_{F,evp} \Delta h_{lg},$$

$$\begin{aligned}
(\dot{S}_{e,\epsilon} + \dot{S}_{e,\alpha})_t &= (-\epsilon_{r,f} \alpha_{r,ch} \sigma_{\mathrm{SB}} T_{r,f,t}^4 + \epsilon_{r,ch} \alpha_{r,f} \sigma_{\mathrm{SB}} T_{ch,o}^4) A_{r,ch} + \\
&\quad (-\epsilon_{r,f} \alpha_{r,cb} \sigma_{\mathrm{SB}} T_{r,f,t}^4 + \epsilon_{r,cb} \alpha_{r,f} \sigma_{\mathrm{SB}} T_{cb,o}^4) A_{r,cb,t} + \\
&\quad (-\epsilon_{r,f} \alpha_{r,r} \sigma_{\mathrm{SB}} T_{r,f,t}^4 + \epsilon_{r,r} \alpha_{r,f} \sigma_{\mathrm{SB}} T_{r,L}^4) A_{r,r}.
\end{aligned} \tag{A.6}$$

Note that the $T_{r,f,t}$ is the apparent flame temperature for the gas volumetric radiation (Assanis and Heywood, [18]) and the $T_{r,L}$ is the top surface temperature of the regenerator.

For the bottom gas zone, the convection heat transfer due to gas flow through the regenerator, the intake and the exhaust are

$$Q_{u,int} = \begin{cases} -\dot{M}_{a,int}c_{p,f}T_n & \text{for} \quad \dot{M}_{a,int} \geq 0 \\ \dot{M}_{a,int}c_{p,f}T_{f,b} & \text{for} \quad \dot{M}_{a,int} < 0 \end{cases}$$

$$Q_{u,exh} = \begin{cases} -\dot{M}_{a,exh}c_{p,f}T_{f,b} & \text{for} \quad \dot{M}_{a,exh} \geq 0 \\ \dot{M}_{a,exh}c_{p,f}T_e & \text{for} \quad \dot{M}_{a,exh} < 0 \end{cases} \tag{A.7}$$

Note that the intake and exhaust occurs in the bottom chamber. The surface-convection heat transfers $\langle Q_{ku,b\text{-}cb}\rangle_{D_B}, \langle Q_{ku,b\text{-}p}\rangle_{D_B}, \langle Q_{ku,b\text{-}r}\rangle_{D_B}$ are determined similarly as in the top chamber.

In the regenerator, the conduction heat transfer rate in the solid phase is given by

$$(Q_{k,r})_{i\text{-}(i+1)} = \frac{T_{r,i} - T_{r,i+1}}{(R_{k,r})_{i\text{-}(i+1)}}, \quad (R_{k,r})_{i\text{-}(i+1)} = \frac{\Delta l_{r,i}}{(1-\epsilon_r)A_r k_r}. \tag{A.8}$$

The surface-convection heat transfer between the porous regenerator and the gas is given by

$$\langle Q_{ku,f\text{-}r}\rangle_i = \frac{\langle \mathrm{Nu}\rangle_{D,p,i} k_f}{D_p}\frac{A_{sf}}{V}(\Delta l_{r,i}A_r)(T_{r,i} - T_{f,r,i}) \tag{A.9}$$

where,

$$\begin{aligned} \langle \mathrm{Nu}\rangle_{D,p,i} &= 2 + (0.4\mathrm{Re}_{D,p,i}^{1/2} + 0.2\mathrm{Re}_{D,p,i}^{2/3})\mathrm{Pr}^{0.4} \\ \mathrm{Re}_{D,p,i} &= \frac{\dot{M}_{f,r,i}D_p}{(1-\epsilon_r)A_r\mu_f}, \; D_p = 6(1-\epsilon_r)\frac{V}{A_{sf}}. \end{aligned}$$

The heat transfer due to the fuel droplet in contact with the regenerator is given by

$$Q_{d,i} = n_d\alpha_d\frac{\mathrm{Nu}_{D,2}k_f}{D_d}A_d(T_d - T_{r,i}). \tag{A.10}$$

where it is assumed that the heat transfer due to the fuel droplet-regenerator interaction occurs between the fuel droplet and the solid phase of the regenerator. $\mathrm{Nu}_{D,2}$ is due to the film boiling heat transfer for the droplets colliding the porous regenerator over Leidenfrost temperature and is expressed as (Bernardin and Mudawar, [19])

$$\mathrm{Nu}_{D,2} = \frac{D_d}{k_f}\rho_{l,\infty}\Delta h_{lg,\infty}\frac{\langle \dot{m}_d \rangle}{\rho_{l,\infty}}\eta_d[1 - \frac{\langle \dot{m}_d \rangle/\rho_{l,\infty}}{(\langle \dot{m}_d \rangle/\rho_l)_o}]\frac{1}{T_s - T_{l,\infty}} + 1,720(T_s - T_{l,\infty})^{-0.088}\langle D_d \rangle^{-1.004}\langle u_d \rangle^{-0.764}\frac{(\langle \dot{m}_d \rangle/\rho_{l,\infty})^2}{(\langle \dot{m}_d \rangle/\rho_l)_o}, \tag{A.11}$$

where

$$\begin{aligned} \eta_d &\equiv \frac{3.68 \times 10^4}{\rho_l \Delta h_{lg,\infty}}(T_s - T_{l,\infty})^{1.691}\langle D_d \rangle^{-0.062} \\ \Delta h_{lg,\infty} &\equiv c_{p,l}(T_{lg} - T_{l,\infty}) + \Delta h_{lg} \\ (\frac{\langle \dot{m}_d \rangle}{\rho_l})_o &\equiv 5 \times 10^{-3}\ \mathrm{m/s}. \end{aligned}$$

Note that the above correlation is based on experimental results for water droplet spray on a nickel-plated copper surface, in an otherwise stagnant air is used for $180℃ < T_s - T_{l,\infty} < 380℃$. Although the regenerator surface condition is out of the range considered, the relation is used for the analysis of the vapor-film regime in impinging-droplet.

In the regenerator, the convection heat transfer rate for the fluid phase is given by

$$(Q_{u,r})_i = \begin{cases} (\dot{M}_{f,r})_i c_{p,f} T_{f,r,i} & \text{for} \quad (\dot{M}_{f,r})_i \geq 0 \\ -(\dot{M}_{f,r})_i c_{p,f} T_{f,r,i+1} & \text{for} \quad (\dot{M}_{f,r})_i < 0. \end{cases}$$
$$i = 0, 1, \ldots, N_r, \tag{A.12}$$

where $T_{f,r,0} = T_{f,b}$ and $T_{f,r,N_r+1} = T_{f,t}$.

At the bottom surface of the porous regenerator $i = 1$, the energy equation is

$$-\frac{(T_{f,b} - T_{r,o})}{\langle R_{ku,b\text{-}r}\rangle_{D_B}} + \frac{T_{r,o} - T_{r,1}}{(R_{k,r})_{o\text{-}1}} = 0. \tag{A.13}$$

At the top surface of the porous regenerator $i = N_r$, the energy equation is

$$-\frac{(T_{f,t} - T_{r,L})}{\langle R_{ku,t\text{-}r}\rangle_{D_B}} - \frac{\sigma_{\text{SB}}(T_{cb,o}^4 - T_{r,L}^4)}{(R_{r,\Sigma})_{cb\text{-}r,t}} - \frac{T_{r,N_r} - T_{r,L}}{(R_{k,r})_{N_r\text{-}L}}$$
$$= -\dot{S}_{e,\epsilon,r} - \dot{S}_{e,\alpha,r}, \tag{A.14}$$

where $(R_{r,\Sigma})_{cb\text{-}r,t}$ is the surface radiation resistance (Siegel and Howell, [35])

$$(R_{r,\Sigma})_{cb\text{-}r,t} = \frac{1-\epsilon_{r,cb}}{\epsilon_{r,cb}A_{r,cb}} + \frac{1}{F_{cb\text{-}r}(A_{r,cb})_t} + \frac{1-\epsilon_{r,r}}{\epsilon_{r,r}A_{r,r}}.$$

Note that the surface and volumetric radiation are neglected at the bottom chamber due to the low temperature.

In the energy conservation equation for the cylinder head, the heat transfer rates are given by $(Q|_{A,ch})_i$ is given for the volumes $i = 1, 2, ...N_{ch} - 1$ as

$$(Q|_{A,ch})_i = -\frac{(T_{ch,i-1} - T_{ch,i})}{(R_{k,ch})_{(i-1)\text{-}i}} + \frac{(T_{ch,i} - T_{ch,i+1})}{(R_{k,ch})_{i\text{-}(i+1)}}, \tag{A.15}$$

and for the inside surface of cylinder head, the energy equation is given by

$$-\frac{(T_{f,t} - T_{ch,o})}{\langle R_{ku,t\text{-}ch}\rangle_{D_B}} + \frac{\sigma_{\text{SB}}(T_{ch,o}^4 - T_{r,L}^4)}{(R_{r,\Sigma})_{ch\text{-}r,t}} + \frac{\sigma_{\text{SB}}(T_{ch,o}^4 - T_{cb,o}^4)}{(R_{r,\Sigma})_{ch\text{-}cb,t}} +$$
$$\frac{(T_{ch,o} - T_{ch,1})}{(R_{k,ch})_{o\text{-}1}} = -\dot{S}_{e,\epsilon,ch} - \dot{S}_{e,\alpha,ch}. \tag{A.16}$$

and for the last volume $i = N_{ch}$, we have

$$(Q|_{A,ch})_{N_{ch}} = -\frac{(T_{ch,N_{ch}-1} - T_{ch,N_{ch}})}{(R_{k,ch})_{(N_{ch}-1)\text{-}N_{ch}}} + \frac{(T_{ch,N_{ch}} - T_{f,w})}{R_{k,ch\text{-}w} + (R_{ku,f})_w}, \tag{A.17}$$

where $(R_{ku,f})_w$ is the thermal resistance for surface convection in the coolant jacket.

A.2 Droplet Evaporation

For the mass conservation equation, the fuel evaporation rate $\dot{M}_d(\mathrm{Re}_D = 0)$ in the quiescent ambient is (Faeth, [21])

$$\dot{M}_d(\mathrm{Re}_D = 0) = 2\pi\rho_{f,t}D_d D_{m,F}\ln(1+\mathrm{B}_M), \tag{A.18}$$

where

$$\mathrm{B}_M = \frac{Y_{F,sg} - Y_{F,\infty}}{1 - Y_{F,sg}}.$$

The saturation fuel-vapor concentration $Y_{F,sg}$ is determined as

$$Y_{F,sg} = \frac{x_{sg}M_F}{(1-x_{sg})M_a + x_{sg}M_F}, \tag{A.19}$$

where

$$x_{sg} = \frac{p_v}{p_{f,t}}, \quad p_v = p_{v,o}e^{-\frac{M_v\Delta h_{lg}}{R_g}(\frac{1}{T_d} - \frac{1}{T_{lg,o}})}.$$

From the mass conservation equation, the droplet diameter is given by

$$\frac{dD_d}{dt} = -\frac{4\rho_{f,t}D_{m,F}}{\rho_{b,l}D_d}\ln(1+\mathrm{B}_M)[1+f(\mathrm{Re}_D,\mathrm{Sc})], \tag{A.20}$$

where $D_{m,F}$ is the diffusion coefficient, D_d is the droplet diameter and B_M are the mass transfer number.

For the energy conservation equation of the fuel droplet, Nusselt number $\mathrm{Nu}_{D,l}$ $(\mathrm{Re}_D = 0)$ in the quiescent ambient is expressed

$$\mathrm{Nu}_{D,l}(\mathrm{Re}_D = 0) = \frac{\dfrac{\dot{M}_d(\mathrm{Re}_D = 0)c_{p,F}}{\pi D_d k_f}}{\exp(\dfrac{\dot{M}_d(\mathrm{Re}_D = 0)c_{p,F}}{2\pi D_d k_f}) - 1}. \tag{A.21}$$

Species conservation equations in the top chamber are given by

$$-\dot{M}_{F,evp} + \dot{M}_{r,F} = -\frac{dM_{F,t}}{dt} \tag{A.22}$$

$$\left[-(\dot{M}_{f,r})_{N_r} + \dot{M}_{r,F}(A/F)_s\right](\frac{O}{A}) - \frac{1}{2}\dot{M}_{NO,t} = -\frac{dM_{O,t}}{dt} \tag{A.23}$$

$$-(\dot{M}_{f,r})_{N_r}\left[1 - (\frac{O}{A})\right] - \frac{1}{2}\dot{M}_{NO,t} = -\frac{dM_{N_2,t}}{dt}, \tag{A.24}$$

where $M_{f,t} = M_{F,t} + M_{O,t} + M_{P,t} + M_{N_2,t}$ and $(A/F)_s = 15.5, (O/A)_s = 0.23$.

The thermal NO formation $M_{NO,t}(= [\mathrm{NO}]_t V_{f,t} M_a \times 10^{-6})$ is estimated by the Zeldovich mechanism. With a steady-state approximation for the nitrogen atom, the neglected reverse reaction, and the oxygen atom concentration presumed to be a equilibrium, the instantaneous formation rate of NO is

$$\frac{d\,[\mathrm{NO}]_t}{dt} = a_r\,[\mathrm{N_2}]_t\,[\mathrm{O_2}]_t^{1/2}\exp(-\frac{\Delta E_a}{R_g T_{f,t}}), \tag{A.25}$$

where [ ] is the species concentration in [mol/cm^3] and $a_r = 5.74\times10^{14}[(\mathrm{cm}^3/\mathrm{mol})^{1/2}/\mathrm{s}]$ and $\Delta E_a/R_g = 66,900$ K (Furuhata et al., [25]).

The mass of fuel injected $M_{F,o}$ is calculated as a function of the air to fuel ratio $(A/F)_a$ and the intake conditions by

$$M_{F,o} = \frac{M_{a,o}}{(A/F)_a}, \quad M_{a,o} = \frac{p_n V_d}{T_n \frac{R_g}{M_a}}. \tag{A.26}$$

BIBLIOGRAPHY

BIBLIOGRAPHY

Combustion-thermoelectric tube

[1] Athanasios, G. K. and Margaritis K., Reciprocating flow regeneration of soot filters, *Combustion and Flame*, 2000, Vol. 121, pp. 488 – 500.

[2] Chen, G., Thermal conductivity and ballistic-phonon transport in the cross-plane direction of superlattices, *Physical Review B*, 1998, Vol. 57, No. 23, pp. 14958–14973.

[3] Echigo, R., Hanamura, K., Yoshida, H., Koda, M., and Tawata, K., Sophisticated Thermoelectric Conversion Devices of Porous Materials by Super-Adiabatic Combustion of Reciprocating Flow and Advanced Power Generation System, *11th International Conference on Thermoelectrics*, 1992, pp. 45–50.

[4] Hanamura, K., Echigo, R., and Zhdanok, S. A., Superadiabatic Combustion in a Porous Medium, *International Journal of Heat and Mass Transfer*, 1993, Vol. 36, No. 13, pp. 3201–3209.

[5] Hoffmann, J. G., Echigo, R., Tada, S., and Yoshida, H., Analytical Study of Flame Stabilization in Reciprocating Combustion in Porous Media with High Thermal Conductivity, *26th Symposium (International) on Combustion*, 1996, pp. 2709–2716.

[6] Hoffmann, J. G., Echigo, R., Yoshida, H., and Tada, S., Experimental Study on Combustion in Porous Media with a Reciprocating Flow System, *Combustion and Flame*, 1997, Vol.111, pp. 32–46.

[7] Kaviany, M., *Principles of Heat Transfer in Porous Media*, Corrected Second Edition, Springer–Verlag, New York, 1999.

[8] Kaviany, M., *Principles of Heat Transfer*, Heat Transfer Course Pack, University of Michigan, Ann Arbor, MI, 2000.

[9] Kesting, A., Pickenacker, O., Trimis, D., Drust, F., Development of a Radiation Burner for Methane and Pure Oxygen Using the Porous Burner Technology, *5th International Conference on Technologies and Combustion for a Clean Environment (Clean Air V)*, 1999, Lisbon, Portugal.

[10] Matros, Yu. Sh. and Bunimovich, G.A., Reverse flow operation in fixed bed catalytic reactors, *Catalytic Review and Science Engineering*, 1996, Vol.38, pp. 1–68

[11] Min, D. K., and Shin, H. D., Laminar premixed flame stabilized inside a honeycomb ceramic, *International Journal of Heat and Mass Transfer*, 1991, Vol. 34, No. 2, pp. 341–356.

[12] Patankar, S. V., *Numerical Heat Transfer and Fluid Flow*, Hemisphere, Washington, DC, 1980.

[13] Rowe, D. M., Editor, *CRC Handbook of Thermoelectrics*, CRC Press, Boca Raton, 1995.

[14] Sahraoui, M., and Kaviany, M., Direct simulation vs volume-averaged treatment of adiabatic, premixed flame in a porous medium, *International Journal of Heat and Mass Transfer*, 1994, Vol. 37, No. 18, pp. 2817–2834.

[15] Siegel, R., and Howell, J. R., *Thermal Radiation Heat Transfer*, Third Edition, Hemisphere, Washington, DC, 1992.

[16] Weinberg, F. J., Editor, *Advanced Combustion Methods*, First Edition, Academic Press Inc., London, 1986.

[17] Yoshizawa, Y., Sasaki, K., and Echigo, R., Analytical study of the structure of radiation controlled flame, *Int. J. Heat Mass Transfer*, 1988, Vol. 31, No. 2, pp. 311–319.

Regenerative Diesel engine

[18] Assanis, D. N., Heywood, J. B., Development and Use of a Computer Simulation of the Turbocompounded Diesel System for Engine Performance and Component Heat Transfer Studies, 1986, SAE paper 860329.

[19] Bernardin, J.D. and Mudawar, I., Film Boiling Heat Transfer of Droplet Streams and Sprays, *International Journal of Heat and Mass Transfer*, 1997, Volume 40, pp. 2579–2593.

[20] Clarke, J. M., Ideal Cycles Incorporating Heat Exchange, 1990, SAE Paper No. 900913.

[21] Faeth, G. M., Evaporation and combustion of sprays, *Progress Energy Combustion Science*, 1983, Vol. 9, pp. 1–76.

[22] Ferrenberg, A. J., Regenerative Internal Combustion Engine, 1988, US Patent 4,790,284.

[23] Ferrenberg, A. J., The Single Cylinder Regenerated Internal Combustion Engine, 1990, SAE Paper No. 900911.

[24] Ferrenberg, A. J., Williams B. E. and McNeal S. R., Low Heat Rejection Regenerated Diesel Engines for Shipboard Mechanical and Electrical Power (Part2), 1995, Contract N00167-92-C-0020.

[25] Furuhata, T., Tanno, S., Miura, T., Ikada, Y., and Nakajima, T., Performance of Numerical Spray Combustion Simulation, *Energy Conversions and Management*, 1997, Vol. 38, No. 10-13, pp. 1111–1122.

[26] Hanamura, K., Echigo, R., and Zhdanok, S. A., Superadiabatic Combustion in a Porous Medium, *International Journal of Heat and Mass Transfer*, 1993, Vol. 36, No. 13, pp. 3201–3209.

[27] Heywood, J. B., *Internal Combustion Engine Fundamentals*, McGraw-Hill, 1988.

[28] Hoffmann, J. G., Echigo, R., Yoshida, H., and Tada, S., Experimental Study on Combustion in Porous Media with a Reciprocating Flow System, *Combustion and Flame*, 1997, Vol. 111, pp. 32–46.

[29] Hiroyasu, H. and Kadota, T., Fuel Droplet Size Distribution in Diesel Combustion Chamber, 1974, SAE Paper No. 740715.

[30] Kaviany, M., *Principles of Heat Transfer in Porous Media*, Corrected Second Edition, Springer–Verlag, New York, 1999.

[31] Kaviany, M., *Principles of Heat Transfer*, Heat Transfer Course Pack, University of Michigan, Ann Arbor, MI, 2000.

[32] Martynenko, V. V., Echigo, R. and Yoshida, H., Mathematical Model of Self-sustaining Combustion in Inert Porous Medium with Phase Change under Complex Heat Transfer, *International Journal of Heat and Mass Transfer*, 1998, Vol. 41, No. 1, pp. 117–126.

[33] Park, C.-W., and Kavinay, M., 1999, "Combustion-Thermoelectric Tube", *Proceeding of the 1999 National Heat Transfer Conference*, Albuquerque, New Mexico, NHTC99-211.

[34] Sahraoui, M., and Kaviany, M., Direct simulation vs volume-averaged treatment of adiabatic, premixed flame in a porous medium, *International Journal of Heat and Mass Transfer*, 1994, Vol. 37, No. 18, pp. 2817–2834.

[35] Siegel, R., and Howell, J. R., 1992, *Thermal Radiation Heat Transfer*, Third Edition, Hemisphere, Washington, D.C., 1992

[36] Westbrook, C. K., Dryer, F. L., Chemical kinetic modeling of hydrocarbon combustion, *Progress Energy Combustion Science*, 1984, Vol. 10, pp. 1–57.

[37] Woschni, G., Universally Applicable Equation for the Instantaneous Heat Transfer Coefficient in the Internal Combustion Engine, 1967, SAE Paper No. 670931.

[38] Yoshizawa, Y., Sasaki, K., and Echigo, R., Analytical study of the structure of radiation controlled flame, *International Journal of Heat and Mass Transfer*, 1988, Vol. 31, No. 2, pp. 311–319.